The Thesis Committee for Kerstan Josef Wallace
Certifies that this is the approved version of the following thesis:

Use of 3-Dimensional Dynamic Modeling of CO_2 Injection for Comparison to Regional Static Capacity Assessments of Miocene Sandstone Reservoirs in the Texas State Waters, Gulf of Mexico

APPROVED BY
SUPERVISING COMMITTEE:

Supervisor:

Michael H. Young

Co-Supervisor:

Timothy A. Meckel

Marc A. Hesse

Use of 3-Dimensional Dynamic Modeling of CO_2 Injection for Comparison to Regional Static Capacity Assessments of Miocene Sandstone Reservoirs in the Texas State Waters, Gulf of Mexico

by

Kerstan Josef Wallace, B.S.Geo.Sci.

Thesis

Presented to the Faculty of the Graduate School of

The University of Texas at Austin

in Partial Fulfillment

of the Requirements

for the Degree of

Master of Science in Geological Sciences

The University of Texas at Austin

May, 2013

Dedication

I would like to dedicate this to my wife, Emily. Your constant support has motivated me without end.

Acknowledgements

The completion of this study would not have been possible without Tip Meckel, David Carr, Mehdi Zeidouni and Ramón Treviño. Tip's endless patience, problem solving, and guidance have helped me to generate new ideas, perform research, and develop as a scientist. To David Carr I owe most of my understanding of technical geologic skills. Thanks to David's tireless efforts in my undergraduate career, I am able to perform most of the tasks that I use every day in the development of my research. Mehdi Zeidouni's enthusiasm and immense technical help in computer modeling made the completion of this research possible. Without Mehdi's expertise, this project would not have succeeded, and I greatly appreciate his willingness to sacrifice his time only for my benefit. Ramón Treviño's invaluable advice, project management skills, and overall geniality have helped to keep me inspired and motivated throughout the length of my research project. I owe any success to these four selfless individuals.

I would also like to thank my committee, Michael Young and Marc Hesse. Their input and direction has been invaluable, and I appreciate their genuine interest in my research and success. I count myself very lucky to have gotten to work with both of them.

I would like to acknowledge the students in the GCCC who have helped in my research along the way. Erin Miller and Andrew Nicholson both helped to broaden my understanding of major components used in this study. I would like to thank Julie Ditkof for using her technical expertise to quickly generate the seismic inversion volume used in this study. Julie's collaboration was instrumental for 3D model generation.

I am very lucky to have worked in such a friendly environment, and to this I owe thanks to my many co-workers at the Gulf Coast Carbon Center and the Bureau of

Economic Geology. The positive, friendly attitude of each of my coworkers has always made it a joy to come to work.

The technical support from the information technology group at the Bureau of Economic Geology surpassed all expectations of assumed duties and on countless occasions has aided me in the swift resolution of technical issues. I would like to thank Chuck Garza, Joseph Yeh, Ron Russel, and Ruben Reyes specifically for aiding me with my frequent technological issues. I greatly appreciate their help in and behind the scenes.

Thank you to Landmark, IHS Petra, and CMG for the use of well log interpretation, seismic interpretation, and modeling software, to Seismic Exchange Inc. for the use and publication of 3D seismic data and to the Jackson School of Geosciences, Bureau of Economic Geology, Gulf Coast Carbon Center, and Department of Energy for funding my research.

Most importantly, I would like to thank my family and my wife for their constant support.

Abstract

Use of 3-Dimensional Dynamic Modeling of CO_2 Injection for Comparison to Regional Static Capacity Assessments of Miocene Sandstone Reservoirs in the Texas State Waters, Gulf of Mexico

Kerstan Josef Wallace, M.S.Geo.Sci.

The University of Texas at Austin, 2012

Supervisors: Michael H. Young, Timothy A. Meckel

Geologic sequestration has been suggested as a viable method for greenhouse gas emission reduction. Regional studies of CO_2 storage capacity are used to estimate available storage, yet little work has been done to tie site specific results to regional estimates. In this study, a 9,258,880 acre (37469.4 km^2) area of the coastal and offshore Texas Miocene interval is evaluated for CO_2 storage capacity using a static volumetric approach, which is essentially a discounted pore volume calculation. Capacity is calculated for the Miocene interval above overpressure depth and below depths where CO_2 is not supercritical. The goal of this study is to determine the effectiveness of such a regional capacity assessment, by performing refinement techniques that include simple analytical and complex reservoir injection simulations. Initial refinement of regional estimates is performed through net sand picking which is used instead of the gross thickness assumed in the standard regional calculation. The efficiency factor is

recalculated to exclude net-to-gross considerations, and a net storage capacity estimate is calculated.

Initial reservoir-scale refinement is performed by simulating injection into a seismically mapped saline reservoir, near San Luis Pass. The refinement uses a simplified analytical solution that solves for pressure and fluid front evolution through time (Jain and Bryant, 2011). Porosity, permeability, and irreducible water saturation are varied to generate model runs for 6,206 samples populated using data from the Atlas of Northern Gulf of Mexico Gas and Oil Reservoirs (Seni, 2006).

As a final refinement step, a 3D dynamic model mesh is generated. Nine model cases are generated for homogeneous, statistically heterogeneous, and seismic-based heterogeneous meshes to observe the effect of various geologic parameters on injection capacity.

We observe downward revisions (decreases) in total capacity estimation with increasingly refined geologic data and scale. Results show that estimates of storage capacity can decrease significantly (by as much as 88%) for the single geologic setting investigated. Though this decrease depends on the criteria used for capacity comparison and varies within a given region, it serves to illustrate the potential overestimation of regional capacity assessments compared to estimates that include additional geologic complexity at the reservoir scale.

Table of Contents

List of Tables

List of Figures

Chapter 1: Introduction

Carbon Sequestration Background

Geologic sequestration of carbon dioxide (CO_2) has been proposed as a potentially viable method for reducing atmospheric greenhouse gas emissions (Lackner, 2003; Tsang et al., 2002; Bachu, 2003). Disposal of CO_2 by injection into geologic reservoirs has been shown to be possible with existing technology (Holloway 2001; Gale et al., 2001; Bachu and Gunter, 2003; Eiken et al., 2011). Storing significant quantities of injected CO_2 in subsurface reservoirs requires favorable geologic properties such as high porosity and permeability, thick stratigraphic sequences, and high sealing capacity. CO_2 is typically injected at depths greater than ~2,600 feet (~792.5 meters) where high reservoir pressure (> 1,071.3 psi, 7.4 Mpa) and temperature (> 88° F, 31° C) change the phase from gaseous to supercritical (Bachu, 2000). Supercritical CO_2 behaves as a fluid with low density, low water solubility, and low viscosity (Friedmann, 2007).

Injection of supercritical CO_2 for storage has been proposed primarily for three types of reservoirs: unminable coal seams, depleted oil and gas fields, and saline aquifers (Benson and Cole, 2008). This study focuses on the latter, as deep saline aquifers have been predicted to play the most important role in any potential long-term, widely practiced Carbon Capture and Storage (CCS) operations due to their large capacity and abundance in the subsurface (White et al., 2003). CO_2 has been successfully injected into saline aquifers at a commercial scale at the Sleipner (Norway) and In Salah (Algeria) fields (Torp and Gale, 2003; Ringrose et al., 2009) and CO_2 capturing technology at point sources is well-developed and has been proven successful, yet costly (Pennline et al., 2008).

Risks associated with CO_2 injection include contamination of drinking water resources through leakage into potable aquifers and mobilization of metals, fault activation through pressure increase, and surface disturbance of plant and animal life through significant CO_2 leakage (Wilson et al., 2003). Studies of natural and industrial analogs of CO_2 leakage show that non-sealing faults or fractures along with improperly plugged and abandoned wells can cause migration of CO_2 to the surface (Lewicki et al, 2006; Keating et al., 2010). In most cases these CO_2 leakages pose little risk to human health and often do not affect water potability.

Estimates of CO_2 storage potential have been generated for many sedimentary basins worldwide. These regional estimates are typically produced by a relatively standard method that consists of a discounted pore volume calculation. The current estimate of total CO_2 storage capacity for North America is between 1160 to 3500 Gigatonnes (Gt) (DOE, 2007).

Offshore Texas Miocene Suitability for Sequestration

The Gulf of Mexico has been an active target for oil and gas production for over 70 years and, as a result, is densely populated with subsurface data. From this dense dataset, the offshore Miocene stratigraphy is known to typically exhibit thick sand intervals with high porosity and permeability, effective trapping mechanisms, and regional seals. The following properties all indicate potentially high CO_2 storage volumes and overall positive CCS feasibility for offshore Texas Miocene sandstones, highlighting the necessity for detailed study of the region and accurate estimates of CO_2 storage capacity:

- High porosity values (>30%) in log and core observations paired with thick clastic intervals (>800 feet, 244 meters) create very large pore volumes for CO_2 storage.
- The high permeability (>1 darcy, 9.9×10^{-13} m^2) observed in offshore Texas Miocene sandstones suggests favorable injectivity with slow pressure build-up.
- Thick regional shale intervals, like the *Amphestegina chipolensis* shale formation, provide low permeability seals which have proved to be adequate for gas trapping on geologic time scales.
- Structural deformation from salt tectonism and growth faulting has created numerous effective trap types that are observed throughout the region.
- Depth of the Miocene interval ranges from 0 to >20,000 feet (6,096 meters), and interval thickness can exceed 15,000 feet (4,572 meters).
- Proximity of offshore Miocene reservoirs to multiple point sources of high CO_2 emission along the Texas coast reduces transportation costs and the existing offshore pipeline infrastructure facilitates the use of offshore reservoirs as CO_2 sinks.
- Environmental risks of sequestration are low in an offshore environment given lack of potable groundwater and a decrease in the impact from potential surface leakage.
- Numerous depleted oil and gas fields in the offshore Miocene may serve as initial storage or enhanced recovery targets.

Geologic Setting

The basin structure of the Gulf of Mexico was developed during the Late Triassic and Early Jurassic, while the North American tectonic plate began separating from the

South American and African tectonic plates. The southward drift of the Yucatan Continental block, away from the North American plate during the Late Triassic to the Late Jurassic, created the connection between the Gulf of Mexico and the Atlantic Ocean (Salvador, 1987). Starting in the Late Jurassic, low sediment supply resulted in mostly carbonate deposition with some siliciclastic influx in the northern Gulf (Winker and Buffler, 1988). In the late Paleocene, interior continental seaways began reaching accommodation limits and newly established rivers allowed for massive, fluvial-dominated, deltaic deposition of siliciclastics in the Gulf of Mexico, which caused the progradation of the continental margin by tens of kilometers (Galloway et al., 2000). During the early Eocene, growth of these newly formed deltas continued along with the generation of two additional fluvial sourced delta systems (Galloway et al., 2011). Clastic deposition continued throughout the Oligocene followed by a large transgression resulting in the deposition of the Anahuac Shale, marking the beginning of the Miocene interval.

The early Miocene is characterized by two, thick, prograding, clastic wedges separated by a significant shale tongue containing *Marginulina ascensionensis* (Marg. A) fauna. These basin-margin sequences have been called Lower Miocene 1 (LM1) and Lower Miocene 2 (LM2), the latter of which is capped by a transgressive shale containing *Amphestegina chipolensis* (Amph. B) fauna. Following deposition of the Amph. B shale, a relatively brief (ca. 3 m.y.) period of deposition resulted in the Middle Miocene (MM) progradational, clastic sequence, which is capped by a transgressive shale containing either *Textularia stapperi* fauna or *Textularia* W fauna (Witrock et al., 2003). Upper Miocene (UM) deposits from the late middle to early late Miocene record extensive margin offlap over a period of 7 million years. The Miocene interval is capped

by a regional flooding event associated with the *Robulus "E"* biostratigraphic marker (Galloway et al., 2000).

The strike-parallel Clemente-Tomas fault system actively displaced strata by up to over 4,000 feet (1219 meters) during the deposition of the LM1 and LM2 through sediment loading and salt evacuation (Winker and Edwards, 1983; McDonnell et al., 2009). The LM1 and LM2 stratigraphic intervals typically are expanded by roughly 2 times on the downthrown side of the fault (Bradshaw and Watkins, 1994). Throughout the middle to late Miocene, growth faulting associated with salt evacuation and progradation of the South Brazos Delta resulted in the Corsair fault system (Vogler and Robinson, 1987). Roughly 12 miles (19.3 kilometers) basinward and contemporaneously to the Corsair fault system, the Wanda fault system formed through salt evacuation (Morton et al., 1985). Two-fold expansion of the upper Miocene section occurs across the Wanda fault system. Salt diapirs associated with secondary salt withdrawal along the Wanda fault zone penetrate Miocene strata (Bradshaw and Watkins, 1994). The locations of regional faults (Olabisi, 2011) are shown in figure 1.1. Many of the hydrocarbon and potential CO_2 traps are formed as a result of the extensive structural deformation associated with regional and local growth faulting and salt tectonism that occurred during and after Miocene deposition.

Previous Work

Regional CO_2 capacity studies have been performed throughout North America and worldwide. North American CO_2 capacity was examined by seven regional groups as part of the regional carbon dioxide sequestration partnerships supported by the U.S. Department of Energy (DOE) (Litynski et al., 2008). European capacity for CO_2 storage was examined similarly, as part of the GeoCapacity program (Vangkilde-Pedersen et al.,

2009). These studies are typically performed by multiplying gross pore volume by CO_2 density and an efficiency factor. The National Energy Technology Laboratory (NETL) has proposed the following equation for determining CO_2 storage resource mass estimates (G_{CO_2}) in saline formations (NETL, 2008):

$$G_{CO_2} = A_t \, h_g \, \varphi_{tot} \, \rho E_{saline} \qquad (1)$$

where,

A_t=Total area

h_g=Gross thickness

φ_{tot}=Total porosity

ρ=CO_2 density

E_{saline}=Storage efficiency factor

The storage efficiency factor (E) is determined at different probability values and for various lithologies through Monte Carlo simulation using field data from multiple oil and gas reservoirs. According to NETL, the efficiency factor corrects for net-to-total area, net-to-gross thickness, effective-to-total porosity, volumetric displacement efficiency, and microscopic displacement efficiency. Net-to-total area is the fraction of the area being studied that is suitable for CO_2 storage. Net-to-gross thickness refers to the fraction of the interval with sufficient porosity and permeability to serve as an adequate CO_2 reservoir. Effective-to-total porosity refers to the fraction of the pore space that is connected. Volumetric displacement efficiency is defined as the fraction of the reservoir volume accessible to CO_2 as a result of the density contrast between CO_2 and connate water. Microscopic displacement efficiency is the fraction of pore space that is occupied by immobile, residual fluids.

Using ranges of observed and hypothesized values for each of these parameters, a set of efficiency factors has been proposed by NETL for use in saline aquifers in sandstone, limestone, or dolomite and for probability values of P_{10}, P_{50}, or P_{90}, which range from 0.4 to 5.5%. Though efficiency values have a large effect on calculated capacity, little work has been done to validate the use and effectiveness of these terms. The regional capacity assessments provided by the DOE regional partnerships are obtained using equation 1 with assumed E values. These studies serve as the current primary basis for the estimate of total North American CO_2 storage capacity and, in turn, imply the feasibility for wide-spread CCS development in the United States.

Previous work has been done to refine capacity estimates through detailed models and injection pilot projects, but these have not been tied back specifically to the regional assessments to examine the validity of the regional calculations. Rock reaction models have been performed in a laboratory setting to better understand fluid dissolution and mineral precipitation of CO_2 and brine at reservoir conditions (Kaszuba et al., 2003; Wellman et al., 2003; Wolf et al., 2004; Giammar et al., 2005). Computer models of rock reactions and flow properties at various reservoir conditions have been used to better understand the importance of the physical and chemical processes associated with CO_2 injection and migration (Flett et al., 2004; Kumar et al., 2004; Allen et al., 2005; Spiteri et al., 2005; Duan et al., 2006; Juanes et al., 2010). Dynamic 2-D and 3-D flow models with reactive transport have been performed for various discrete reservoirs (Johnson et al., 2004; Lagneau et al, 2005; Doughty et al., 2008; Yang, 2008; Audigane et al., 2010). Pilot projects have been performed to test feasibility and validate expected CO_2 migration and reaction behavior (Hovorka et al. 2006; Pawar et al., 2006; Frailey and Finley, 2008). While these studies have been useful in developing a better understanding of CCS, they

are relatively disconnected from the regional work that is being used to estimate large-scale potential of CCS. One potential reason for this relates to the challenge of normalizing results from estimates at disparate scales, which is addressed in the current research.

Project Description

The goals of this project are to (1) provide a static, regional CO_2 capacity assessment for the coastal and offshore regions of the Miocene interval; (2) perform a dynamic 3-D flow simulation on a discrete, seismically defined reservoir within the regional assessment area; (3) test the accuracy of the regional assessment by comparing it to the 3-D reservoir model and intermediate refinement steps; and (4) assess the cost-capacity relationship at reservoir and regional scales, to better understand the effect of additional refinement.

The regional assessment presented here and those performed as part of the DOE partnerships are necessary for determining feasibility of widespread CCS projects. Though the NETL calculation method is commonly used for this kind of assessment, the accuracy of the resulting estimations is rarely tested and the overall utility of the results is unknown. In this study, coarse regional well data paired with overlapping fine scaled 3D seismic data allows us to compare regional-scale static capacity calculations to detailed, data-constrained 3D reservoir models. To assess the value of any additional capacity refinement, the costs and benefits of required data and interpretation time are important to consider. Increasing the scale and reducing the uncertainty on capacity estimates will raise project costs, but at some point the change in estimated capacity will become negligible. Further refinement can only occur with additional subsurface data (core, well tests, etc.)

By performing the additional data collection and interpretation procedures typically required before injection begins at a given site, the reliability/utility of the regional CO_2 capacity assessment is examined. Comparing the findings from these late-stage (geologically mature) models to earlier assessments may have broader implications to CCS by showing the relative similarity or differences between the results. The amount of capacity change observed with increasing refinement will be useful to understand the accuracy of this and other existing or future static regional capacity assessments. Requisite refinement measures needed to confidently estimate capacity can be determined for the specific geologic setting presented here and may, to some degree, be applied to other capacity assessments, particularly those in a similar geologic setting. The results of this study may be important in long-term CCS planning by providing some measure of the accuracy of existing storage capacity estimates. By observing the degree to which the regional capacity estimate changes with refinement, the feasibility of widespread CCS can be better understood.

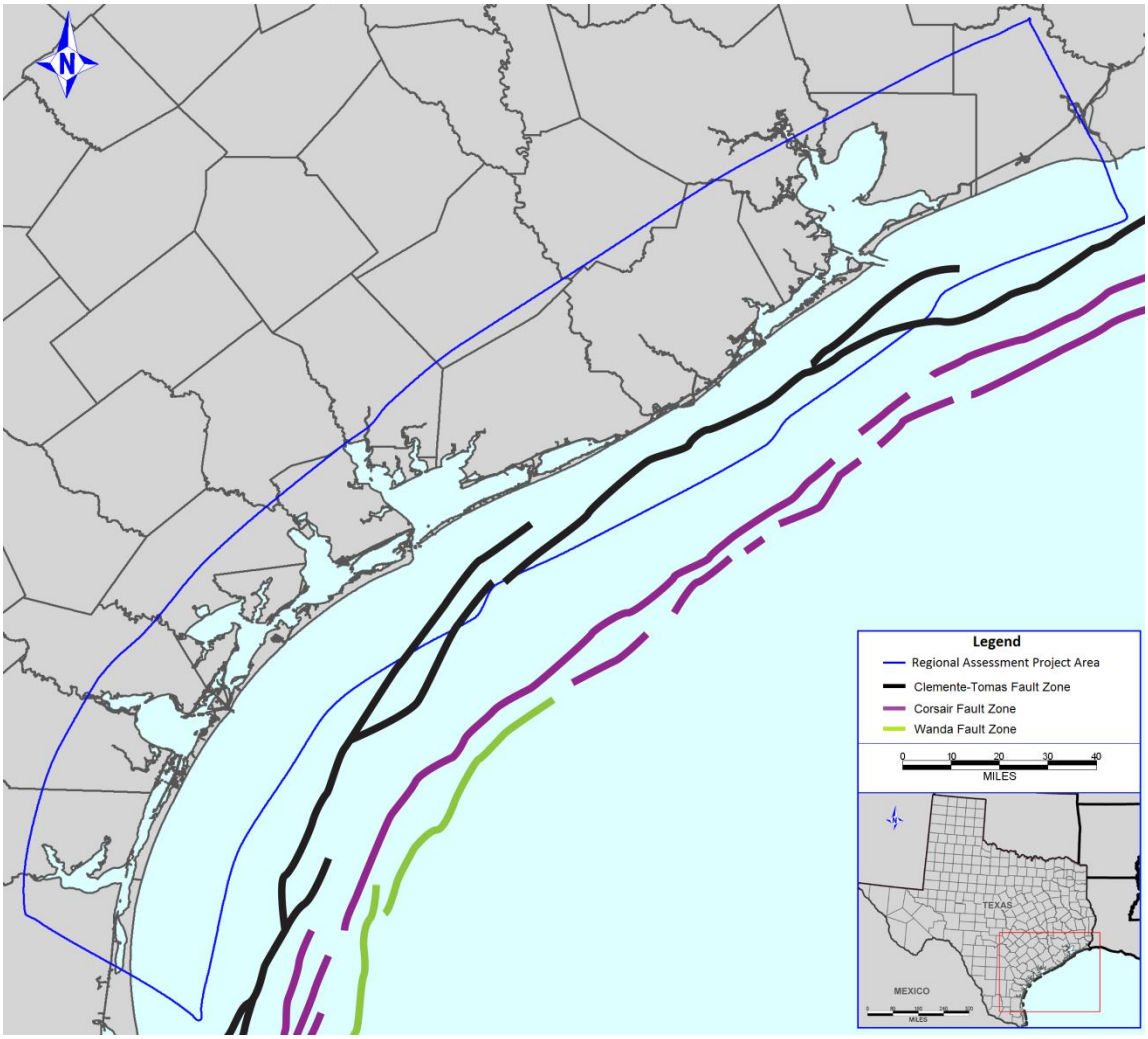

Figure 1.1: Location of regional faults and study area outline modified from Olabisi (2011).

Chapter 2: Methodology

CHAPTER 2.1: SITE AND DATASET DESCRIPTION

The regional CO_2 capacity assessment performed in this study covers 9,258,880 acres (37469.4 km^2) of the Texas coastal and offshore area (figure 2.1). The extent of the study area is largely determined by location of available data (well logs). The basinward extent of the study area is defined by a 6.5 mile (10.5 km^2) buffer in the seaward direction from the state water-federal water boundary.

A Petra software (IHS; 3.83; Houston TX) database containing 89,566 wells with locations and directional surveys for deviated wells (Carr, 2010) is used as the basis for much of the regional assessment. Well logs and/or paleontological data from 3,300 wells are used to pick formation tops, select sand intervals, and/or determine porosity. Well logs used in this study contain various combinations of curves and include spontaneous potential (SP), resistivity, gamma ray, caliper, neutron density, bulk density, and sonic (DT). Digital well logs (Log ASCII Standard; LAS) of key wells are either purchased or digitized from available raster logs. In this study, LAS log curves are used primarily for porosity determination, synthetic seismogram generation, seismic posting, and seismic inversion volume generation.

3D seismic data, provided by Seismic Exchange Incorporated (Houston, TX), allows high resolution structure mapping of seismic horizons and generation of a discrete 3D reservoir model. The selection of San Luis Pass as the site location for the dynamic model is based primarily on favorable structure typical of the Miocene observed in regional seismic horizon mapping. The location also overlaps with an ongoing high resolution seismic survey that may be important in future studies. The trap type and closure area in the San Luis Pass site are typical to the region and best represent an

average potential saline aquifer CO_2 sink in the offshore Texas Miocene. Velocity data (check shots) have been acquired for 14 wells near the San Luis Pass to aid in the time-depth conversion of a portion of the 3D seismic volume. Figure 2.1.1 shows the location of the regional assessment project area, wells used, available 3D seismic survey, depth converted seismic volume, and the dynamic reservoir model site.

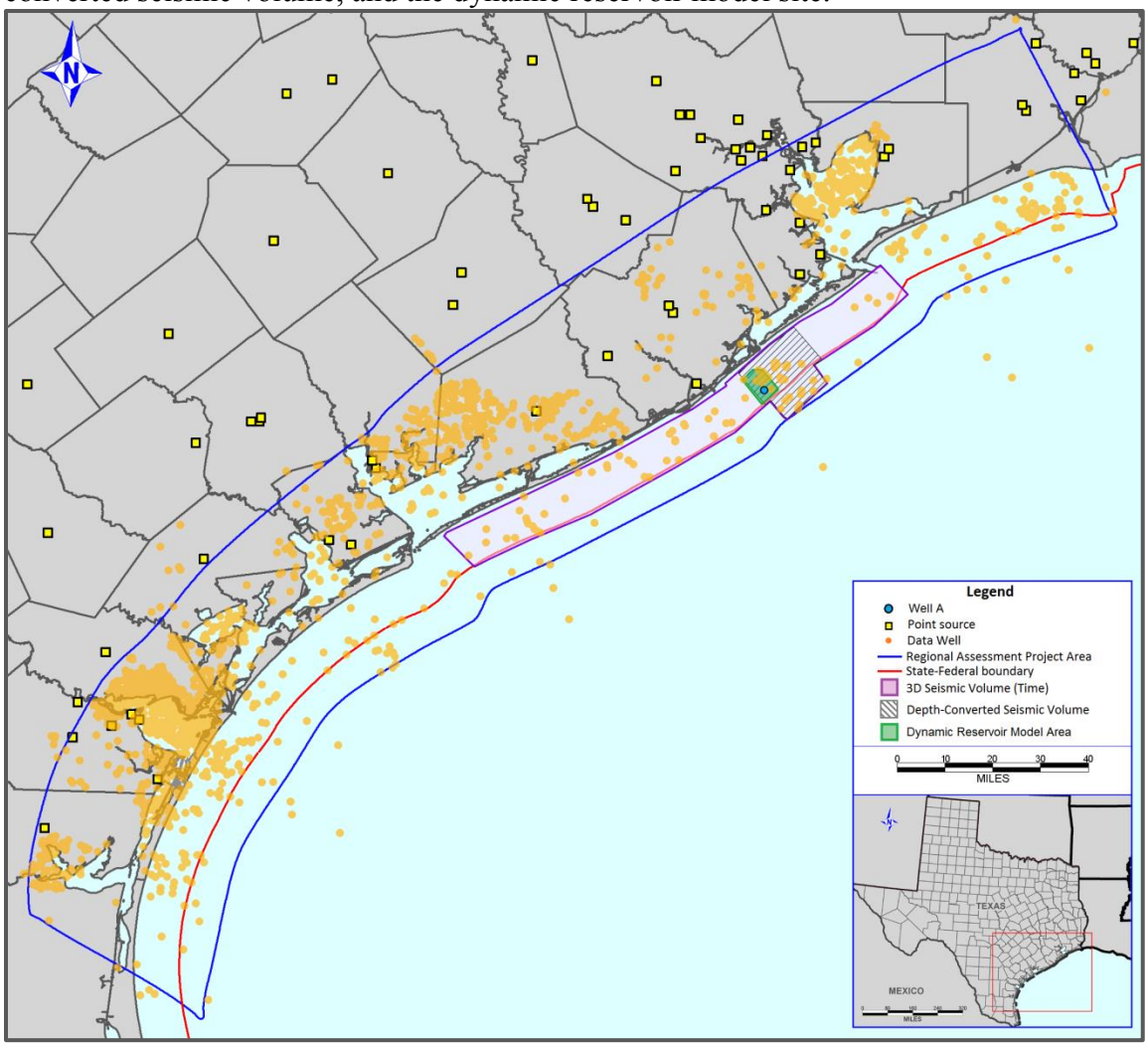

Figure 2.1.1: Site location for regional study and reservoir model along with well and point source locations.

CHAPTER 2.2: REGIONAL STATIC MODEL METHODOLOGY

We apply the regional static CO_2 storage capacity equation (equation 1) to a portion of the subsurface volume that we call the "capacity interval," which is defined here as the portion of Miocene strata that is present at depths suitable for CO_2 storage (figure 2.2.1). Miocene strata is identified using paleontological markers and stratigraphic definitions from Galloway (2000). The top of the Miocene interval is marked by the presence of the *Robulus* E paleontological marker and the base of the Miocene is picked as the maximum flooding surface (MFS) associated with the Anahuac Shale Formation. The upper depth limit for CO_2 injection is determined by the minimum temperature and pressure conditions at which CO_2 will be supercritical. Nicholson (2012) compiled temperature and pressure data from wells and produced fields in Miocene strata in the Texas State Waters and applied the Peng-Robinson equation of state to determine regional CO_2 fluid density with depth (figure 2.2.2). From this relationship, we determine the upper limit of 3,300 feet (1,006 meters) to be the minimum depth at which CO_2 is likely to be supercritical. The lower depth limit for CO_2 injection is determined by the depth at which the hydrostatic pressure in the subsurface is exceeded. This overpressure data is acquired through the United States Geological Survey (USGS).

Using raster and LAS wireline logs, paleontological data, and the top and base of Miocene are picked in a Petra software database. Figure 2.2.3 shows a type log with the key stratigraphic and paleontological horizons used to make interpretations. The top of the Miocene interval is picked in 1,227 well logs and the base of the Miocene interval is picked in 3,042 logs. Well log horizon picks are interpolated over the study area using a least squares algorithm and a square grid cell size of 640 acres (2.6 km^2). Though faulting is present in the region, the relatively large well spacing within the study area did not

allow for confident fault interpretation. Only the Clemente-Tomas fault zone is considered in the interpolation algorithm for the base of Miocene, the position of which is given in a study by McDonnell et al. (2009). Figure 2.2.4 shows the gridded interpolations of the base of the Miocene interval. Over the study area, the top of the Miocene interval ranges in depth from 130 to 3,972 feet (40 to 1,211 meters) (subsea true vertical depth). Over the majority of the study area, the top of the Miocene is shallower than 3,300 feet (1,006 meters) deep, thus, in most areas, the supercritical depth cutoff is used to define the top of the capacity interval.

The gross thickness term of equation 1 (h_g) is determined for the capacity interval by subtracting the upper surface of the capacity interval from the lower surface. The upper surface is obtained by merging the grid of the top of the Miocene interval with a grid populated with constant values of 3,300 feet (1,006 meters) with the criteria that, in overlapping areas, the deeper of the two grids will be retained. Similarly, the base of the capacity interval is generated by merging the grid of the Anahuac MFS with the interpolated USGS overpressure depth grid (figure 2.2.5) with the criteria that in overlapping areas, the shallower of the two grid values will be retained. The gross thickness of the capacity interval is then obtained by subtracting the upper merged grid from the lower merged grid (figure 2.2.6). Note that for all grids generated in the regional capacity estimate, grid node locations are identical.

The porosity term of equation 1 (φ_{tot}) is determined for the capacity interval using 86 wireline logs with LAS porosity curves. Either sonic porosity or density porosity curves are used to determine porosity. Sonic logs are more common in our database, but the sparse distribution of LAS porosity data requires that bulk density logs are considered

for wells with no sonic curve. Sonic porosity is calculated with the empirical transform[1] proposed by Schlumberger (1989) modified from Raymer et al. (1980):

$$\text{PHIS} = .67\left(1 - \frac{\text{DT}_m}{\text{DT}}\right), \qquad (2)$$

where,

PHIS = Sonic porosity

DT = Interval transit time reading from log[1]

DT_m = Interval transit time for rock matrix (quartz = 55.5 μsec/ft)

Density porosity is calculated using the transform from Schlumberger (1998):

$$\text{PHID} = \frac{\text{RHOB} - \text{RHO}_m}{\text{RHO}_{fl} - \text{RHO}_m}, \qquad (3)$$

where,

PHID = Density porosity

RHOB = Bulk density measurement from log

RHO_m = Density of matrix (quartz = 2.65 gram/cm^3 [g/cc])

RHO_{fl} = Density of pore fluid (water = 1 g/cc)

The resulting porosity values are averaged within net sandstone reservoir portions of the capacity interval.

Net sandstone intervals for porosity determination are identified through the use of the SP and gamma ray curves that correspond to the porosity curves for a given well. SP curves are the preferred indicator of net sandstone as they highlight intervals of qualitatively high permeability, whereas gamma ray curves primarily show sandstone volume. Since high injectivity is necessary for CO_2 sequestration, intervals with relatively high permeability are of primary interest. Gamma ray curves are used for wells

[1] Note that some empirical equations are expressed only in oilfield units.

in which an SP curve is absent. SP curves are straightened along a shale baseline to eliminate the effect of SP drift caused by salinity changes of the connate water with depth. SP curves are then normalized by transforming the log values into a shale volume percentage ranging from 0% (clean sand) to 100% (pure shale) using the equation:

$$\mathrm{VSH_{SP}} = \frac{\mathrm{SP}-\mathrm{SP_{CL}}}{\mathrm{SP_{SH}}-\mathrm{SP_{CL}}}, \qquad (4)$$

where,

VSH_{SP} = Shale volume from the SP curve

SP = Log value from SP curve

SP_{CL} = Average log value in a clean sand (constant in each well)

SP_{SH} = Average log value in pure shale (constant in each well)

Likewise, gamma ray values are normalized for wells with no SP curve by using the equation (Schlumberger, 2000):

$$\mathrm{ISH_{GR}} = \frac{\mathrm{GR}-\mathrm{GR_{CL}}}{\mathrm{GR_{SH}}-\mathrm{GR_{CL}}}, \qquad (5)$$

where,

ISH_{GR} = Gamma ray shale index

GR = Log value from gamma ray curve

GR_{CL} = Average log value in a clean sand (constant in each well)

GR_{SH} = Average log value in pure shale (constant in each well)

In addition to shale volume normalization, a Tertiary non-linear correction is applied to the resulting ISH_{GR} values to correct for overly optimistic sand volumes due to non-linearity (Larionov, 1969):

$$\mathrm{VSH_{GR}} = .083(2^{3.7\mathrm{ISH_{GR}}} - 1), \qquad (6)$$

where,

VSH_{GR}=Volume of shale from gamma ray log

The resulting average porosity values within the net reservoir portions of the capacity interval are interpolated between the 86 well locations using a least squares algorithm and a grid cell size of 640 acres (2.6 km^2) (figure 2.2.7).

The CO_2 density term of equation 1, ρ, is determined as a function of depth over the study area by applying a depth-CO_2 density transform (Nicholson, 2012) to the midpoint of the capacity interval. The midpoint of the capacity interval is obtained by dividing the gross thickness grid by 2 and subtracting it from the base of the capacity interval grid. The depth-CO_2 density transform is derived from the empirical pressure-temperature-depth relationships (figure 2.2.2) and is comprised of two equations that describe the CO_2 fluid density vs. depth curve by depth range:

$$\rho_s = 21.1(\frac{Z_s}{1000})^4 - 311.5(\frac{Z_s}{1000})^3 + 1637.3(\frac{Z_s}{1000})^2 - 3449.5(\frac{Z_s}{1000}) + 2665.6, \quad (7)$$

where,

ρ_s=CO_2 density from 2,000 feet to 5,000 feet of depth

Z_s=Depth (between 2,000 and 5,000 feet)

$$\rho_d = .475(\frac{Z_d}{1000})^3 - 14.27(\frac{Z_d}{1000})^2 + 147.71(\frac{Z_d}{1000}) + 154.92, \quad (7)$$

where,

ρ_d=CO_2 density from 5,000 feet to 10,000 feet of depth

Z_d=Depth (between 5,000 and 10,000 feet)

These transforms are applied to the appropriate depth ranges of the midpoint depth grid and the resulting CO_2 density distribution across the project area can be seen in figure 2.2.8.

CO_2 capacity is calculated using equation 1 with the gridded inputs of h_g, φ_{tot}, and ρ. An efficiency factor (E) of 0.02 is selected; in this case, E=0.02 is the P_{50} value for saline aquifer sandstone reservoirs recommended by NETL (2008). The grid size of 640

acres (2.6 km^2) is used for all input grids and is used as the input area in equation 1 for the resulting capacity map (figure 2.2.9).

Net Sand Refinement of Static Regional Capacity

Refinement of the regional static capacity estimate is possible through quantification and measurement of any corrections contained within the efficiency factor assumptions. Given the limited scope of available data, the only feasible regional capacity refinement step is the correction of net to gross sand volume. The NETL method used to determine E, consists of a Monte Carlo simulation populated with a distribution of net to gross ratio values from various basin studies along with measured distributions for other corrections, to produce a range of possible efficiencies for a given lithology (NETL, 2008). By measuring the actual net to gross ratio from logs and removing the net to gross consideration from the NETL Monte Carlo simulation, it is possible to estimate a "net regional capacity".

Net permeable sand is picked in 1,009 wireline logs using a raster SP curve. SP curves are used for net sand determination primarily because they are the most abundant curve in the dataset, but also because they highlight permeable zones. Logs are used for net sand picking if they meet the following criteria:

(1) The logged interval spans the entire Miocene interval

(2) The log is legible

(3) The log does not show dramatic SP drift over the Miocene interval

(4) Each run of the log contains a pure shale and a clean sand

Because SP logs are measured on a relative scale, applying a uniform cutoff for sand picking is not possible. Also, the use of raster logs requires a manual normalization of each log. To systematically normalize the sand picking procedure, a method is devised

in which a cutoff is calculated for each log based on clean sand and pure shale end members. Before interpretation begins, log raster images are straightened and depth calibrated. Next, clean sand and pure shale intervals with thicknesses greater than 50 feet (15.2 meters) are identified within the Miocene strata. The average SP value within the clean sand interval (SP_{min}) is estimated. Likewise, SP_{max} is calculated by estimating the average SP value in the pure shale interval. By obtaining SP_{min} and SP_{max}, it is possible to determine an SP value that can be used as a cutoff for net sand reservoir through the implementation of the simple equation:

$$SP_{net} = C(SP_{min} + SP_{max}), \qquad (8)$$

where,

SP_{net}=Net sand cutoff SP value (mV)

C=cutoff value (0-1)

Determining an appropriate value for C is performed through a core to log comparison, where 310 feet (95 meters) of a Lower Miocene core spanning the interval from 14,840 to 15,150 feet (4,523 to 4,618 meters) measured depth from the Amoco Production (State Tract 487-L SW/4 #2 well) is used for comparison with the corresponding raster SP log. Sandy intervals observed in the core can be best identified in the SP curve by using equation 8 with a C value of 0.53.

Calculation of SP_{net} allows the placement of a vertical trend line of the sand cutoff on the raster log. Net sand is then picked by highlighting the intervals that cross the cutoff trend line in the negative direction. The location of the top and base of the sand pick is placed at the inflection point between local SP maximum and minimum values of the SP curve rather than at the intersection of the SP curve and the trend line. The net sand values are summed for each well over the entire Miocene (figure 2.2.10) as well as

the capacity interval (figure 2.2.11) and interpolated between wells using a least squares algorithm and a grid cell size of 640 acres (2.6 km^2).

The efficiency factor presented by the NETL (2008) is calculated using the equation:

$$E_{saline} = E_{An/At} E_{hn/hg} E_{\varphi e/\varphi tot} E_v E_D, \quad (9)$$

where,

E_{saline}=Efficiency factor for saline formations

$E_{An/At}$=Net to total area

$E_{hn/hg}$=Net to gross thickness

$E_{\varphi e/\varphi tot}$=Effective to total porosity

E_v=Volumetric displacement term (plume shape)

E_D=Microscopic displacement term (accessible pore volume)

By obtaining ranges for each input variable from data collected in multiple basins and using the distribution of the values for each variable as an input in a Monte Carlo simulation, a distribution of E_{saline} values is generated (NETL, 2008). For a detailed explanation of the Monte Carlo simulation methodology, refer to Appendix B of the Carbon Sequestration Atlas of the United States and Canada.

To account for the use of net sand thickness in the regional capacity estimate, the $E_{hn/hg}$ variable in equation 9 is removed. The NETL methodology is recreated and E_{net} is calculated using the modified equation:

$$E_{net} = E_{An/At} E_{\varphi e/\varphi tot} E_v E_D, \quad (10)$$

where,

E_{net}= Net storage efficiency in a saline aquifer

E_{net} is calculated using the commercial program Goldsim (Version 10.5 SP3, GoldSim Technology Group), with all variables in equation 10 equal to those given by the NETL (2008). The resulting E_{net} P_{50} value is 4.5%.

Net sand capacity or "Net capacity" is calculated by using a modified version of equation 1:

$$G_{CO_2net} = A_t\, h_{net}\, \varphi_{tot}\, \rho E_{net,} \qquad (11)$$

where,

G_{CO_2net}=Estimated storage capacity in net reservoir portion of the subsurface

h_{net}=Net sand thickness

Net capacity per square mile (figure 2.2.12) is calculated using the grid for net sand in the capacity interval (figure 2.2.11) as the input for the h_{net} variable and an E_{net} of 0.045 while keeping the remaining variables of equation 11 the same as those used in the gross regional calculation.

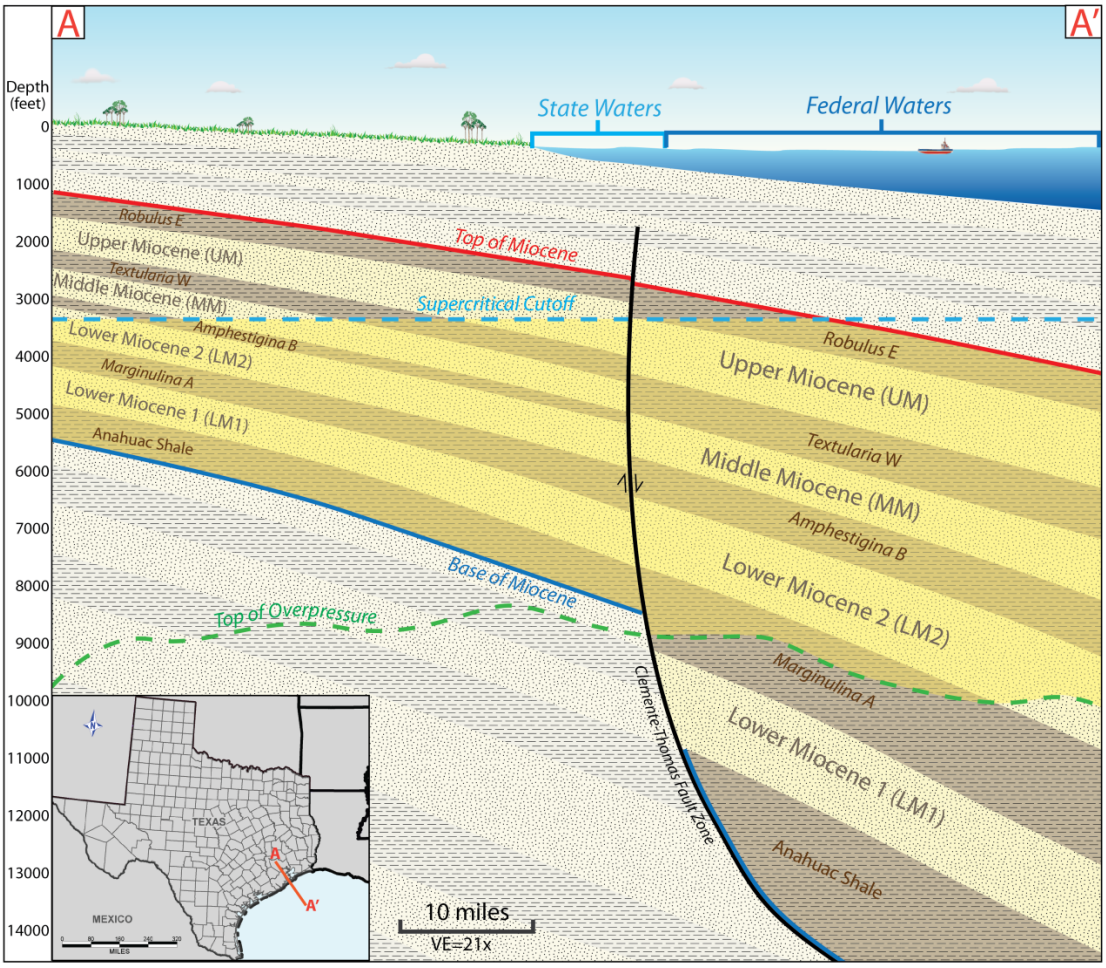

Figure 2.2.1: Schematic cross section showing the capacity interval (yellow) and Miocene stratigraphy with definitions from Galloway (2000).

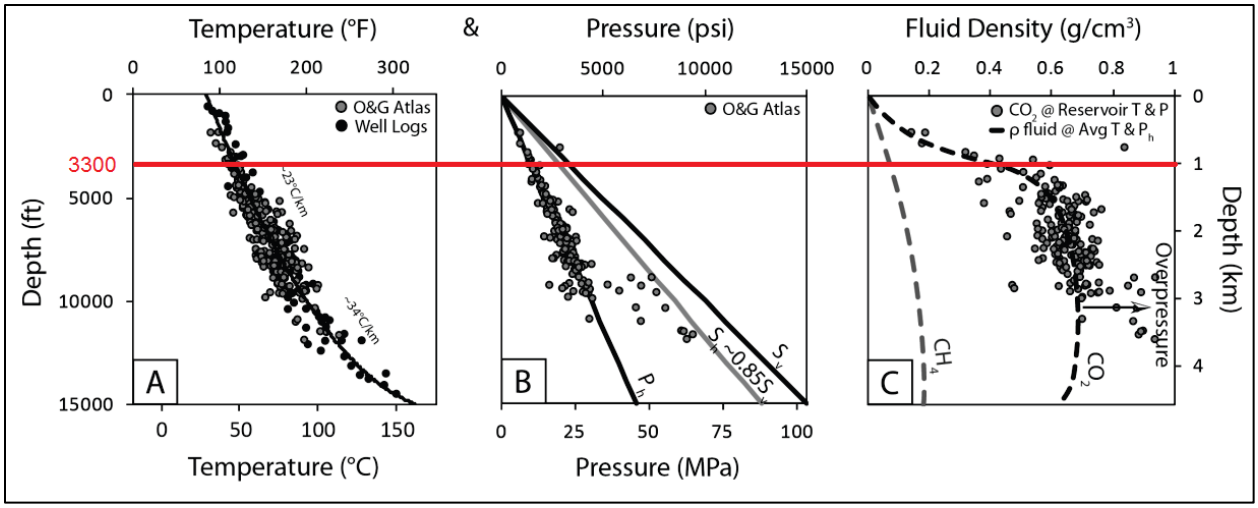

Figure 2.2.2: Temperature (A), pressure (B), and CO_2 fluid density (C) vs. depth showing upper depth limit for supercritical behavior in red (Modified from Nicholson, 2012).

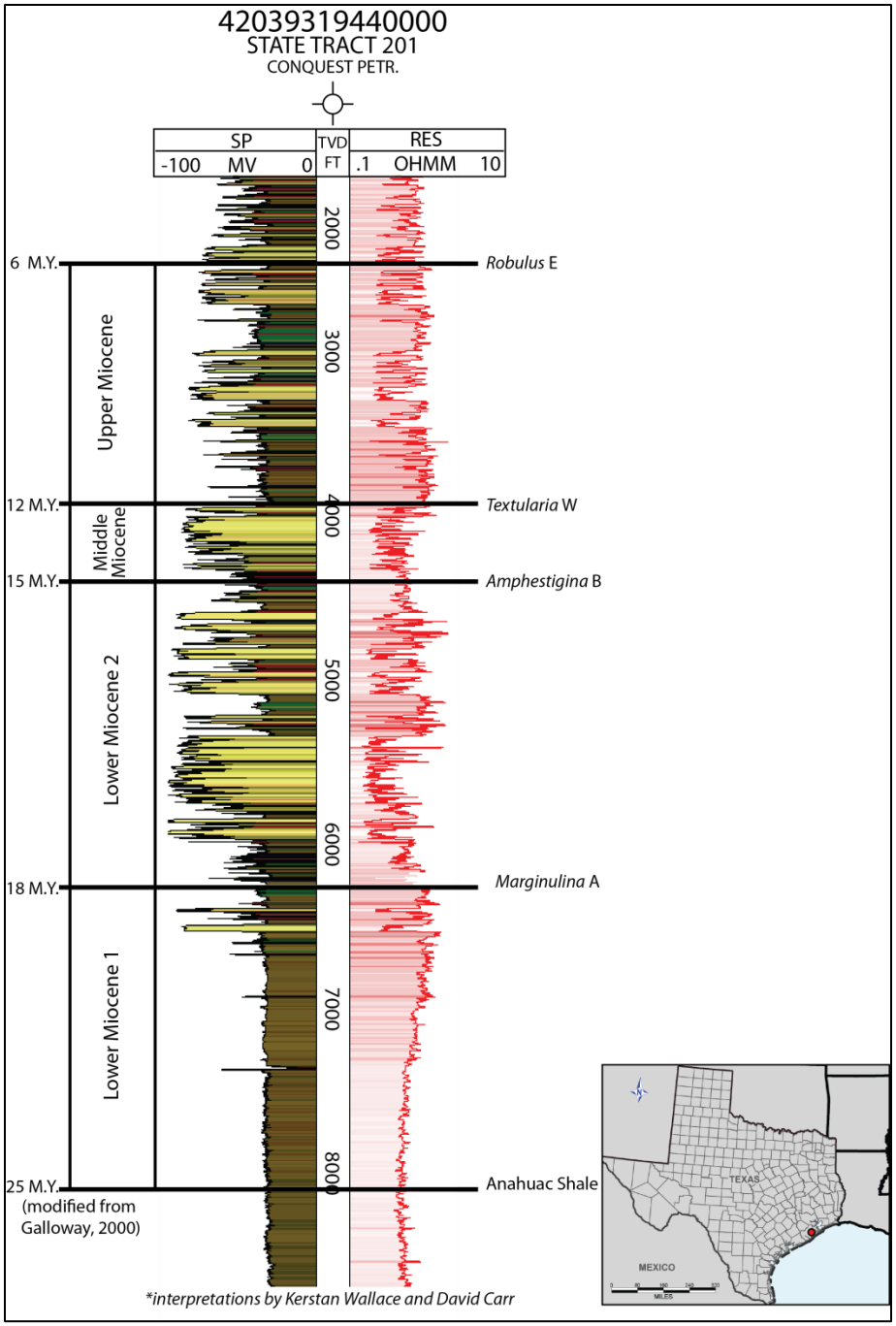

Figure 2.2.3: Type log of offshore Miocene interval showing major formation tops used for regional interpretations along with corresponding formation names, paleontological markers and geologic age modified from Galloway (2000).

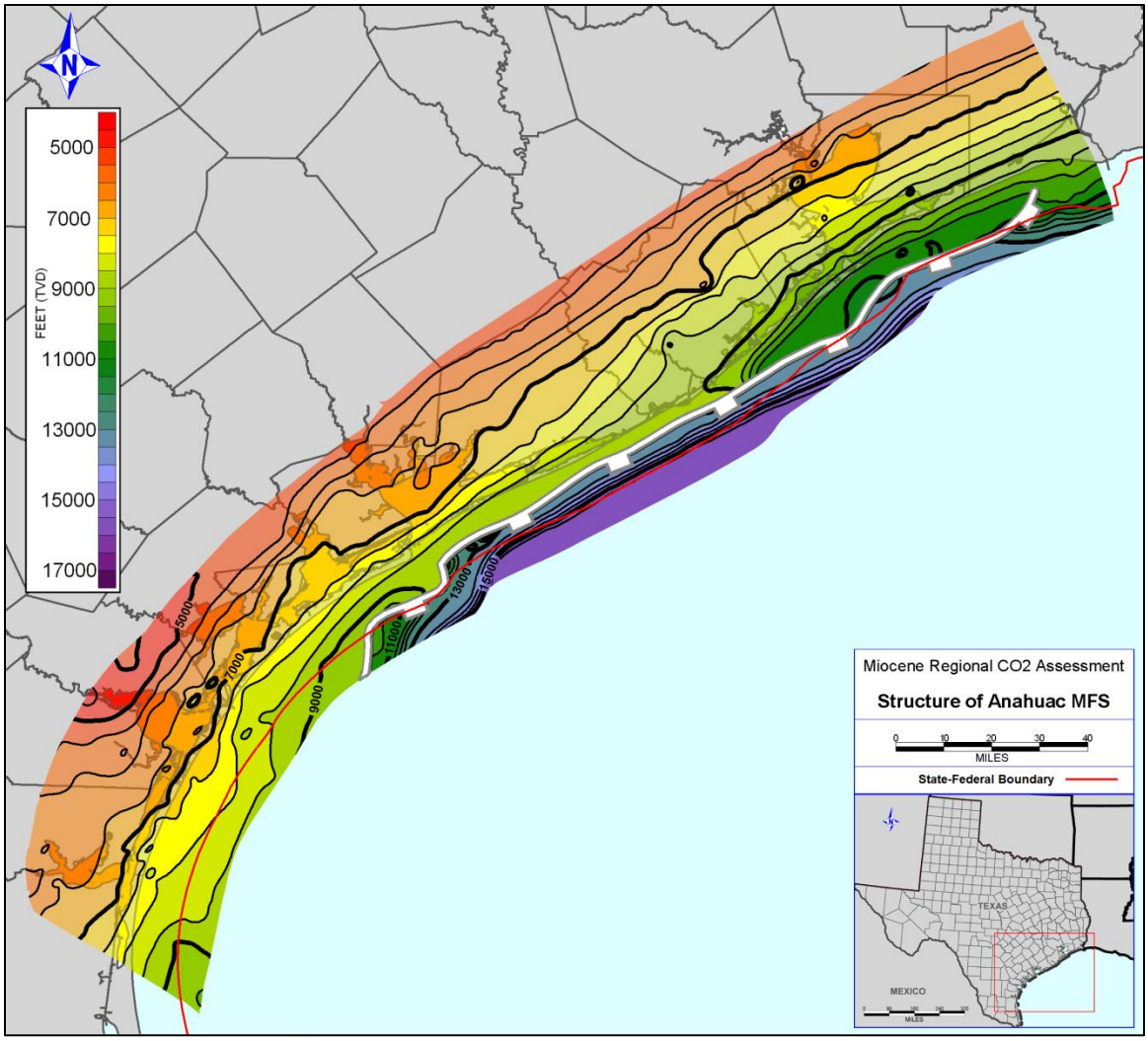

Figure 2.2.4: Structure of the base of Miocene interval based on interpretations in 3,042 well logs. Clemente-Tomas fault zone shown in white from McDonnell et al. (2009).

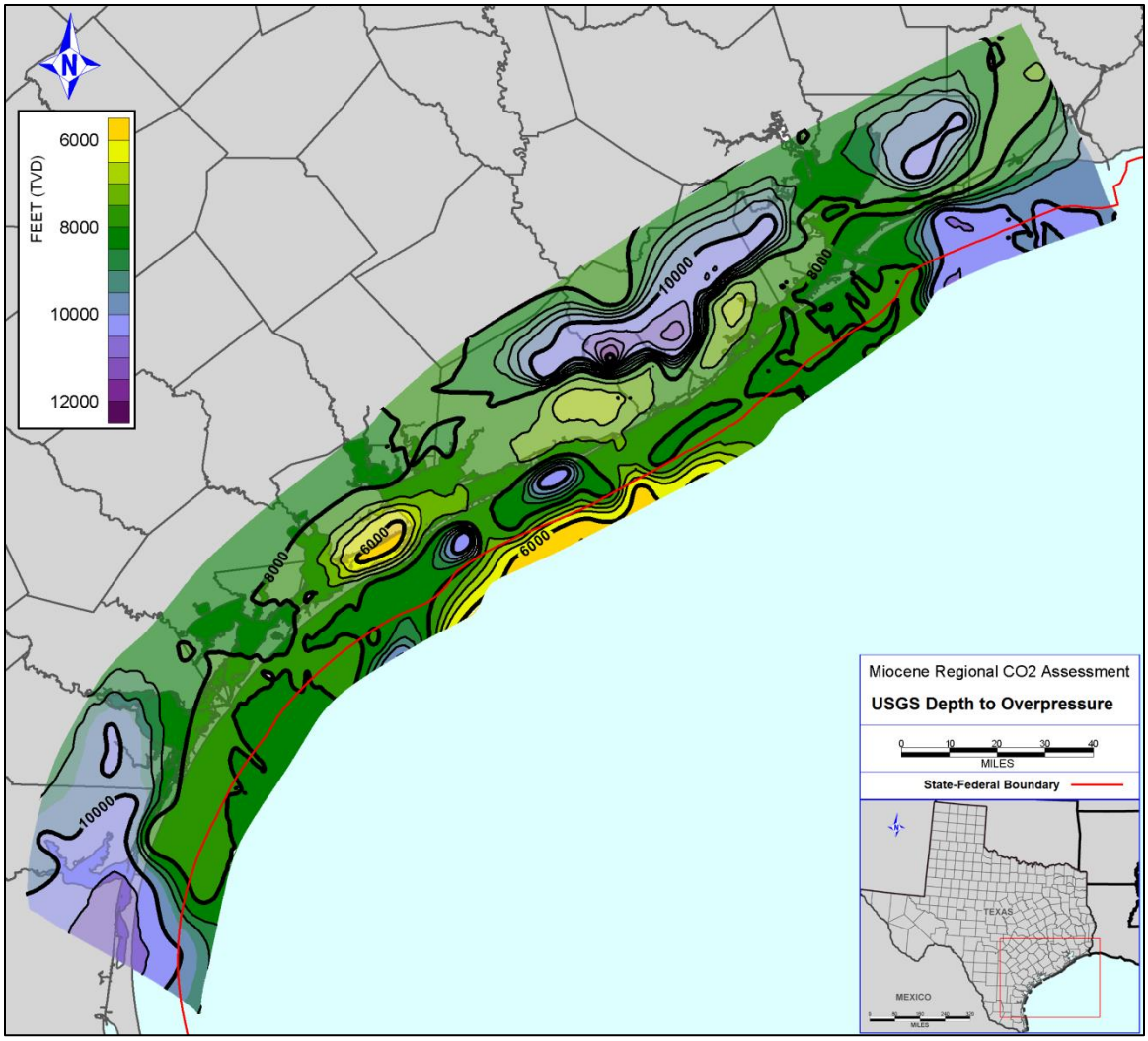

Figure 2.2.5: Depth to reservoir overpressure gridded over study area from USGS data.

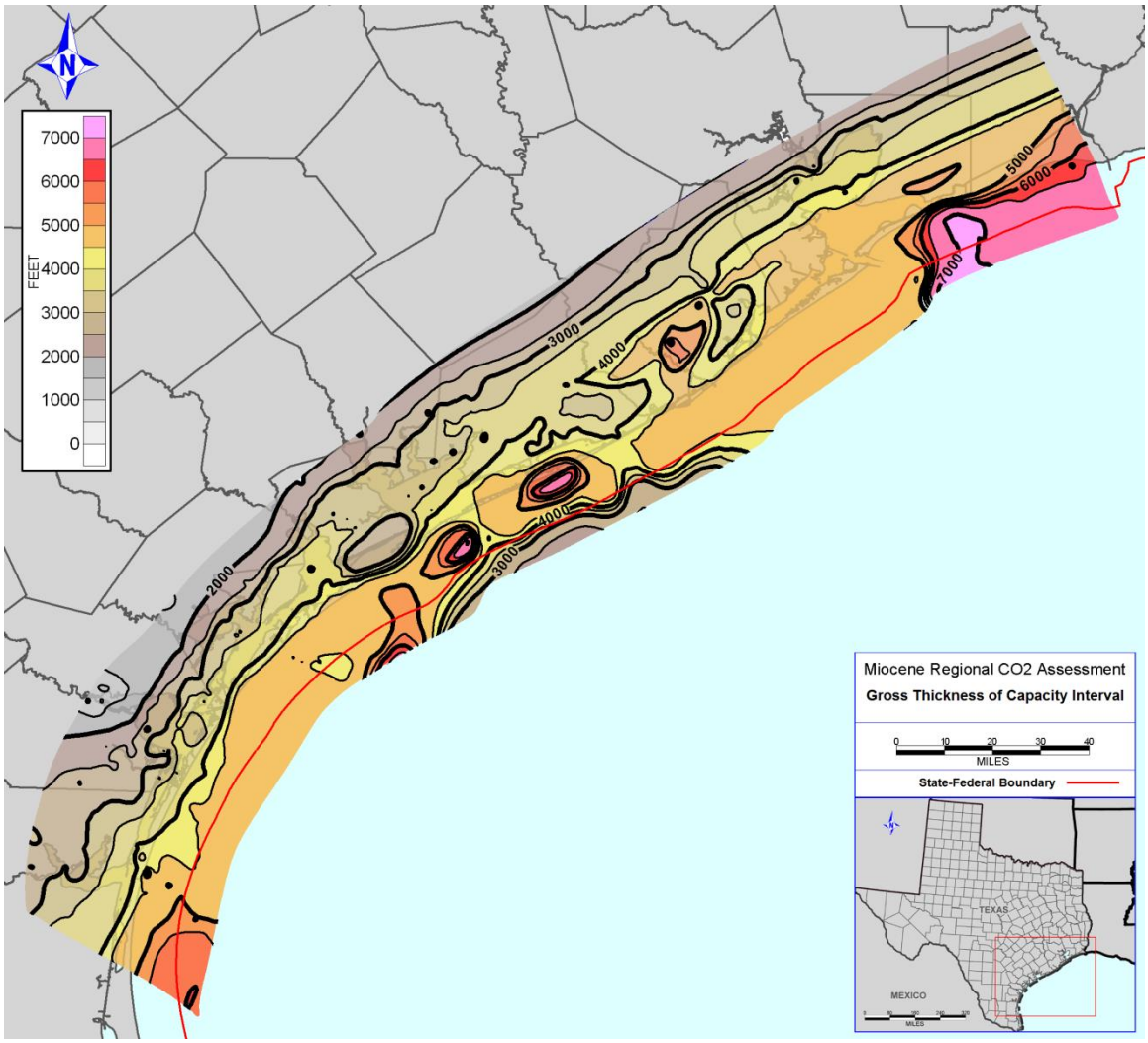

Figure 2.2.6: Gross thickness of capacity interval.

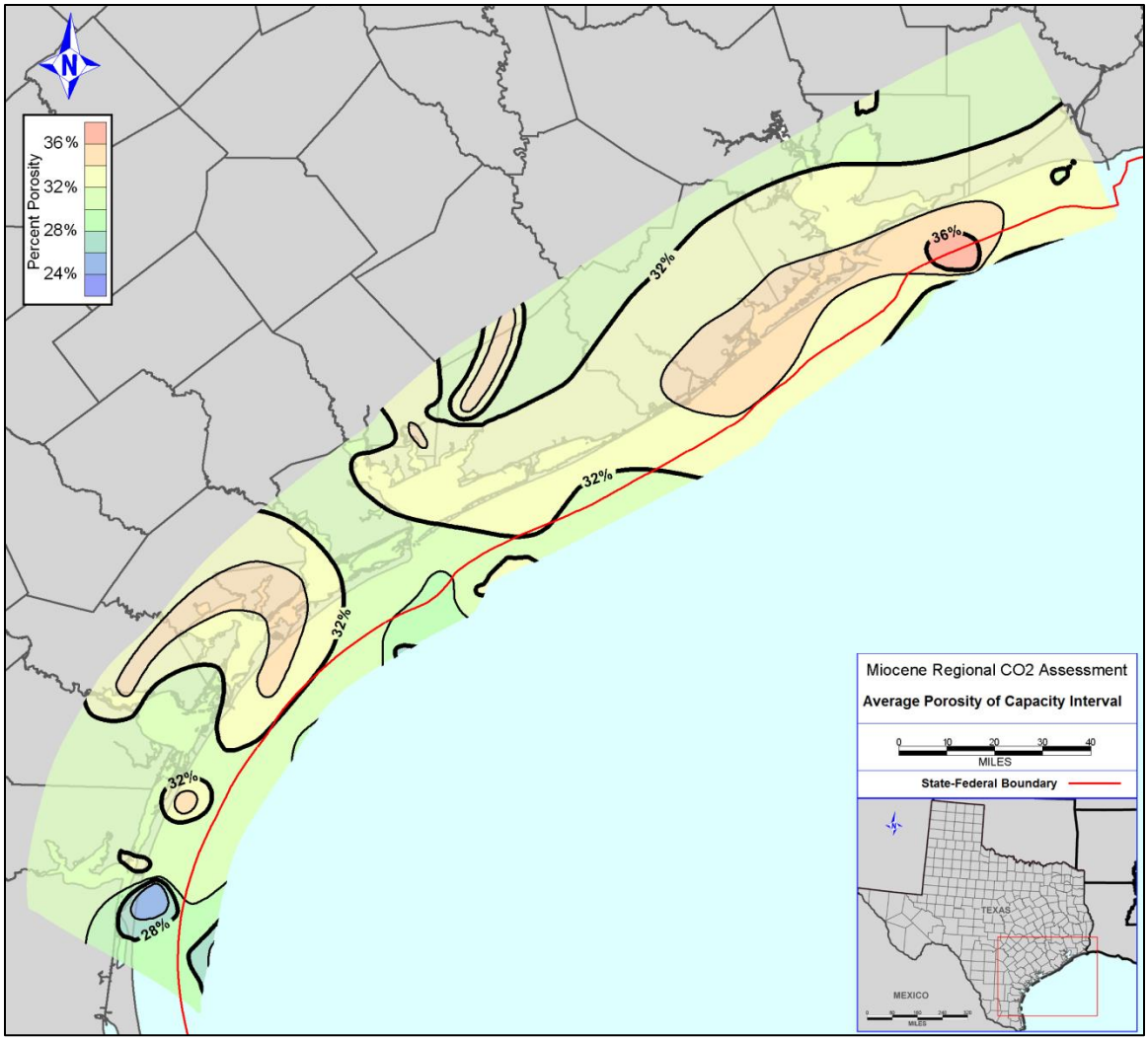

Figure 2.2.7: Average porosity of the capacity interval based on 86 log measurements.

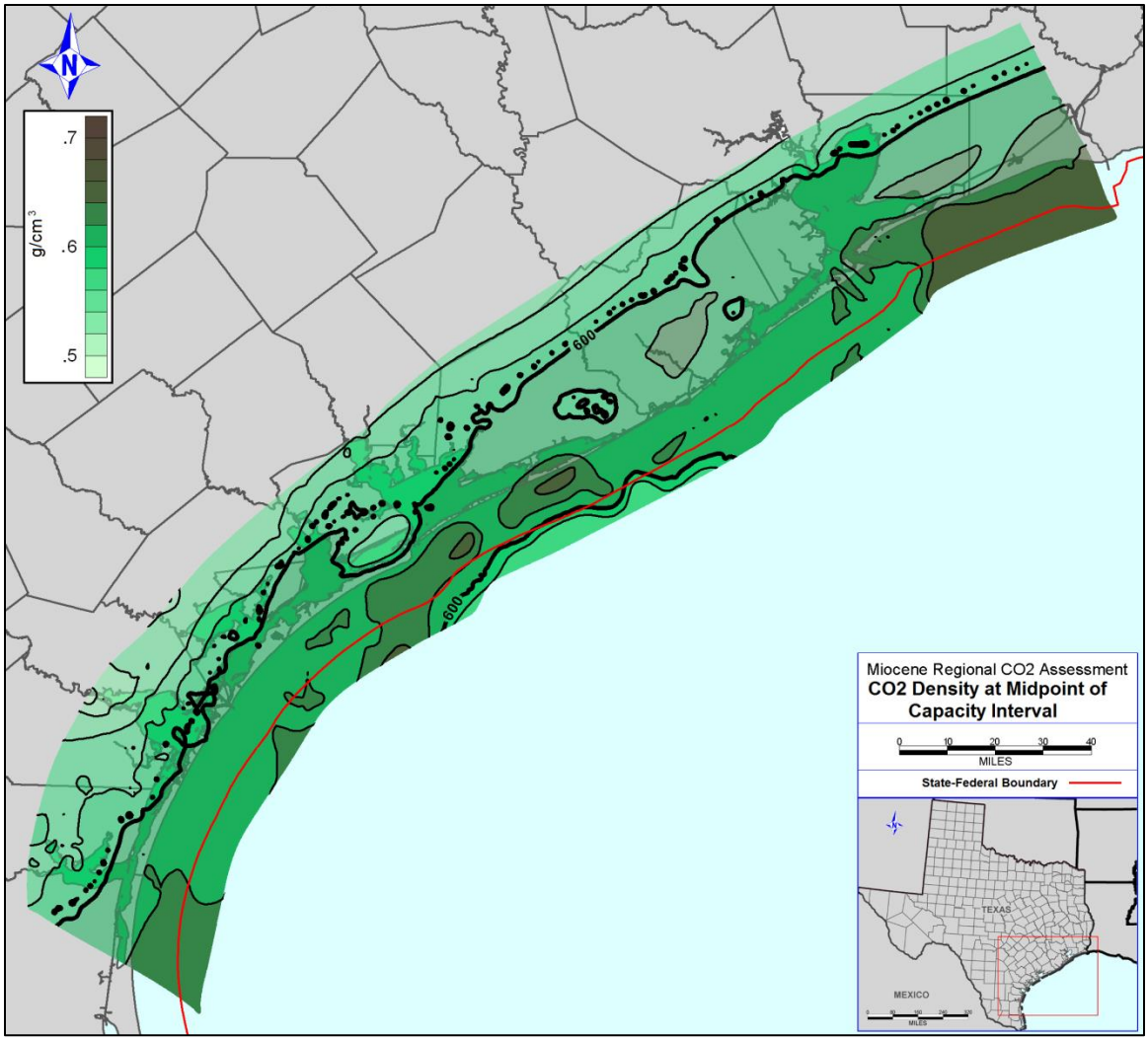

Figure 2.2.8: CO_2 density at midpoint of capacity interval.

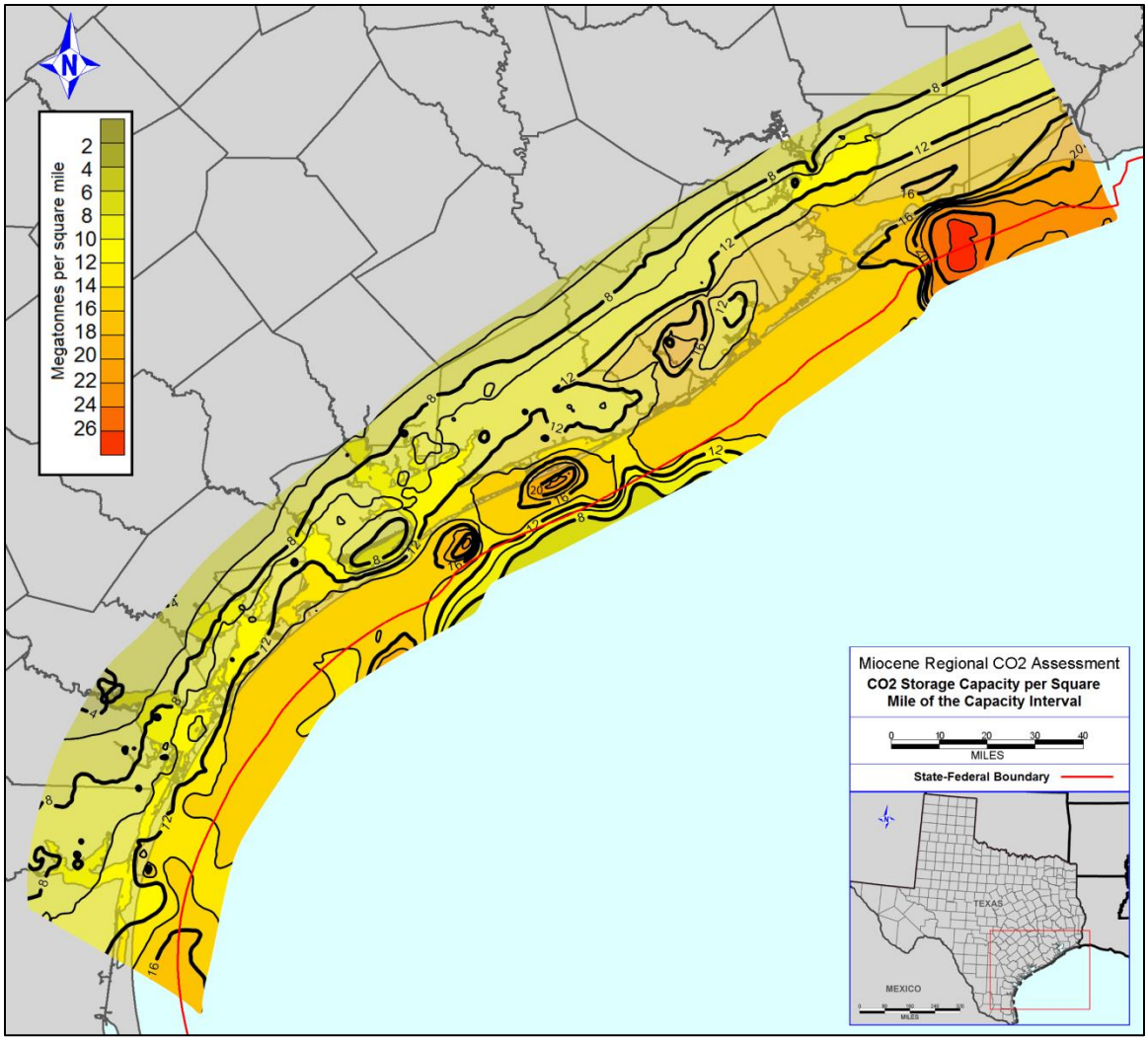

Figure 2.2.9: CO_2 storage capacity of the capacity interval per square mile.

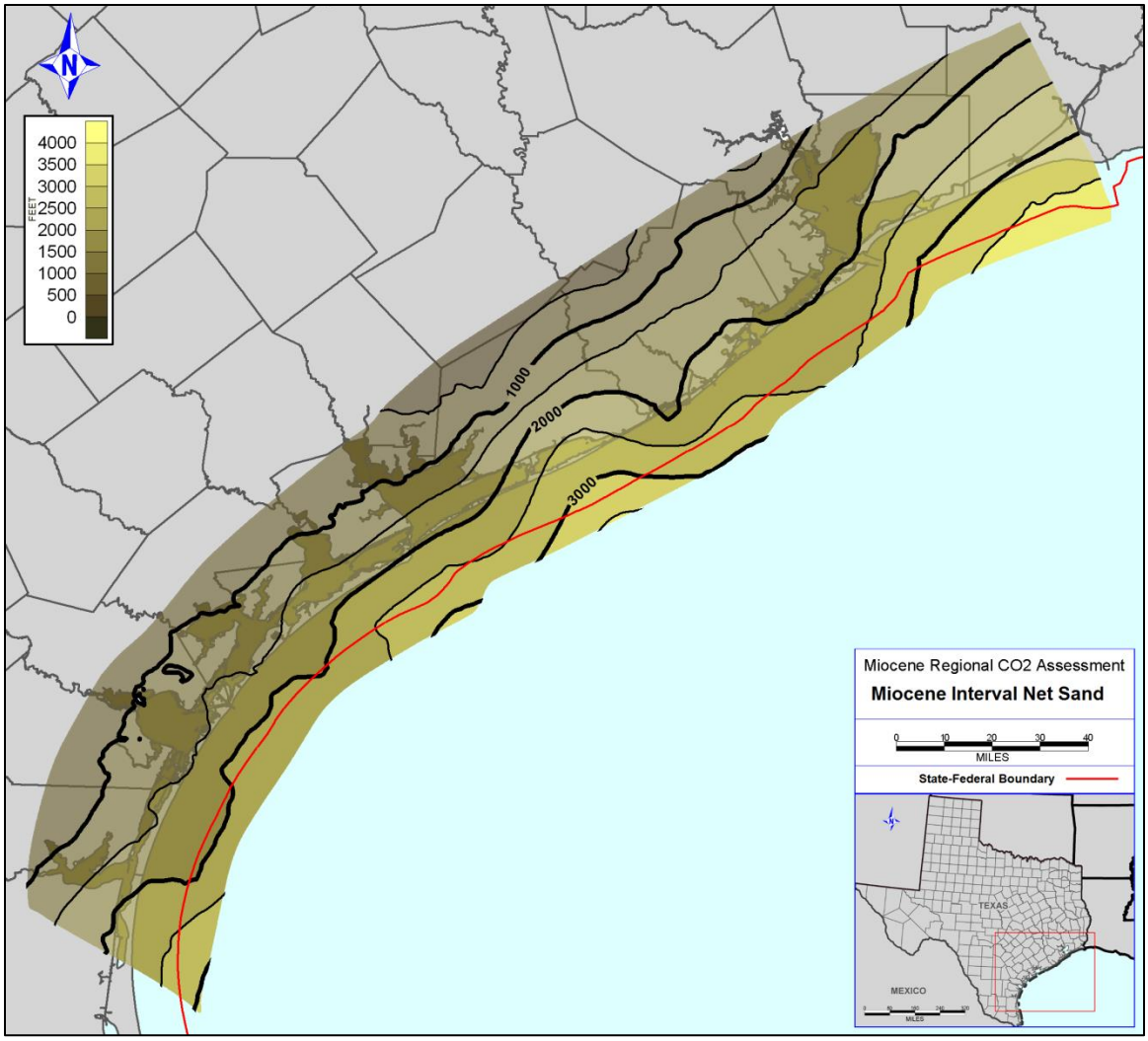

Figure 2.2.10: Net sand in Miocene interval picked in 1,009 raster SP curves.

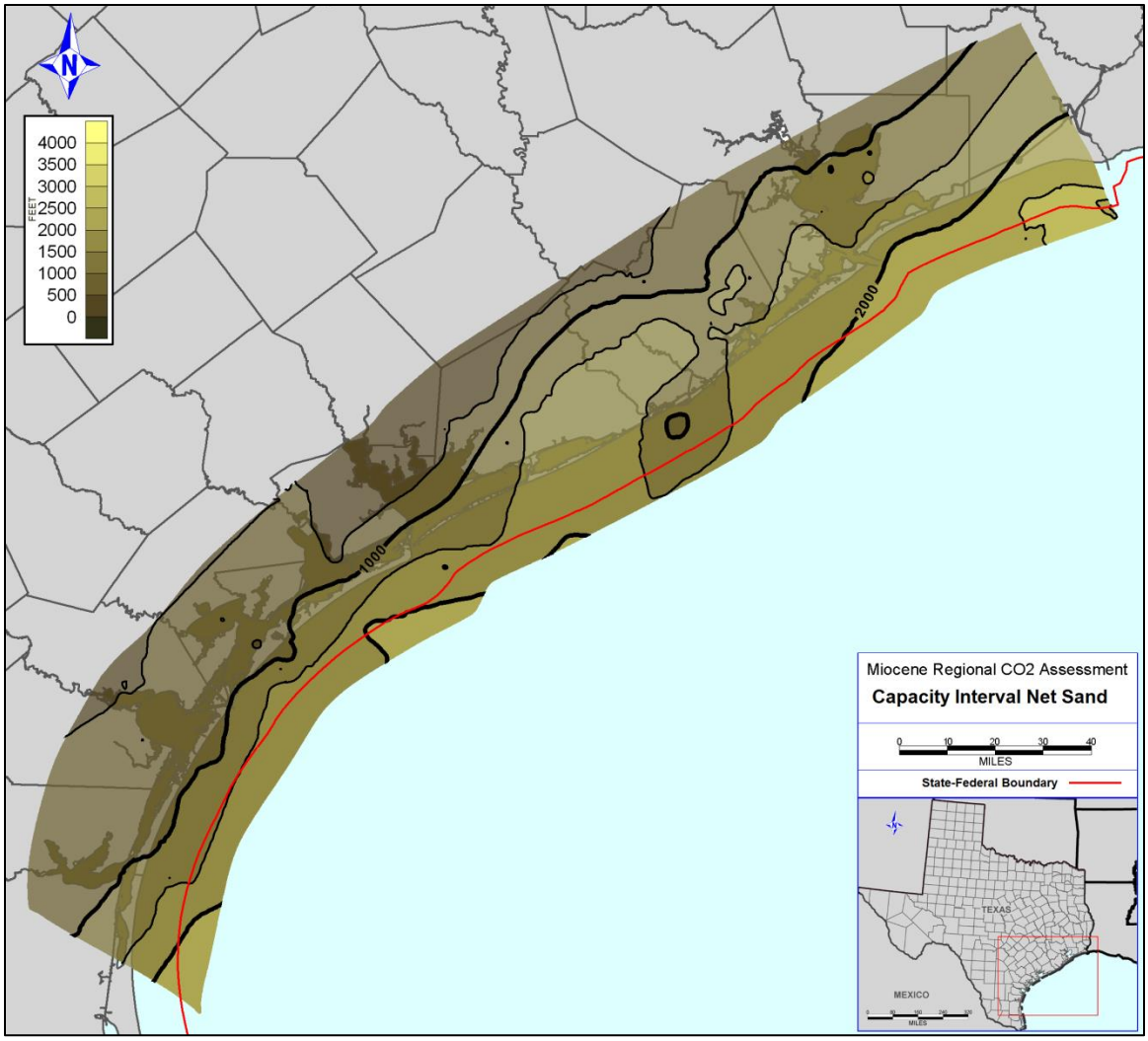

Figure 2.2.11: Net sand of capacity interval picked in 1,009 raster SP curves.

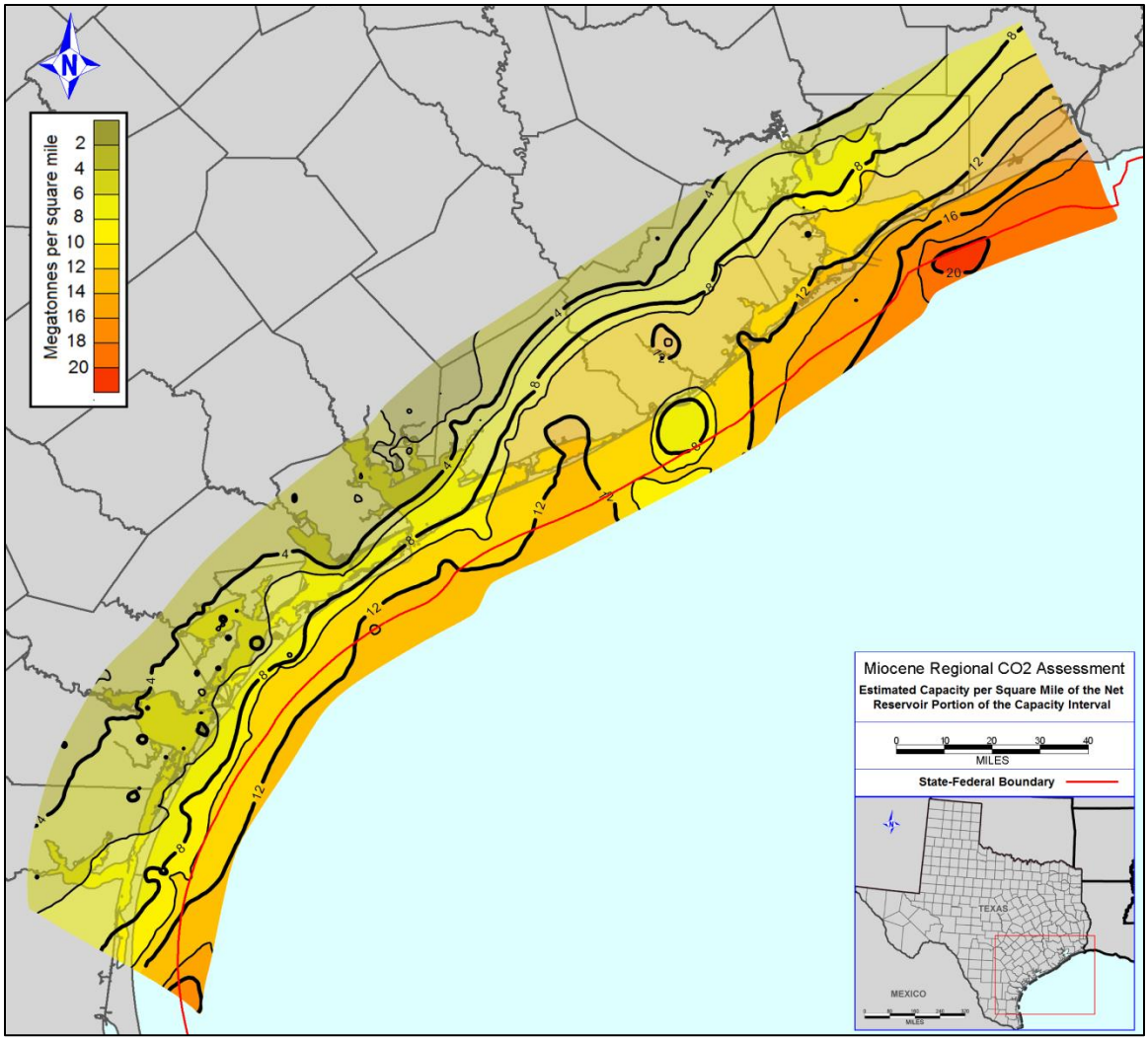

Figure 2.2.12: Estimated storage capacity per square mile of the net reservoir portion of the capacity interval.

CHAPTER 2.3: SIMPLE DYNAMIC ANALYTICAL MODEL

To further refine capacity estimates and to test the validity of the regional assessments performed in chapter 2.2, a portion of the study area is used for simple dynamic analytical modeling. Using Geoprobe, (Halliburton; version 5000; Houston, TX)

Permedia (Halliburton; version 5000; Houston, TX), and Matlab (Mathworks; version R2013a; Natick, MA), a 26,496 acre (107 km^2) subset of the study area is mapped from seismic data, structurally analyzed, and used as a reservoir input for dynamic modeling. In addition to refined reservoir characterization and fluid flow considerations, dynamic modeling yields a preliminary understanding of the time required to fill a reservoir to capacity. This aspect of time consideration is important but often not considered in capacity assessments.

Model Site and Depth Interval

Selecting an area for dynamic modeling is based primarily on the structure of the subsurface from seismic horizon mapping. Using the LM2 regional horizon map generated by Nicholson (2012) (figure 2.3.1) from the SEI 3D seismic volume, the structure of the subsurface can be examined for CO_2 injection suitability. Initial closure assessment of this horizon paired with log and production data suggest that the area southwest of San Luis Pass has a structure, thickness, fluid content, and areal extent that is representative of a typical saline aquifer within the offshore capacity interval. The non-uniqueness of the model interval characteristics is important for ensuring the broader application of the model-to-regional scale comparison results to the entire study area.

To accurately generate required inputs for the simple dynamic analytical model, the structure of the reservoir interval must be mapped in depth with high confidence. This requires that the 3D seismic data be depth converted over the model area. Depth conversion is performed in Landmark DepthTeam (Halliburton, version 5000, Houston, TX) using 16 checkshots, 10 synthetic seismograms from sonic logs, and 6 mapped time horizons (Zeng, 2012). The resulting depth volume is used for all subsequent seismic mapping, attribute extraction, and inversion generation.

The reservoir interval of interest within the model area and capacity interval is selected based on seismic amplitude and continuity paired with SP, gamma ray, sonic, and resistivity curves examined through log-seismic ties. Figure 2.3.2 shows a log-seismic tie with stratigraphic interpretations for a key well in the model area, which we refer to as "well A" (API: 42706301770000). The selected reservoir lies above the Amph. B shale interval near a sequence boundary associated with the progradational, fluvio-deltaic, MM sequence. The model interval is mapped at a zero amplitude crossing above (+/-) and below (-/+) a reflection minimum. The reflector is chosen for its amplitude strength, continuity, and apparent tie to a thick sand package as measured in the low SP and gamma ray logs in intersecting wells. Faults are mapped in detail and used as barriers in subsequent 3D flow model analyses. Fault consideration is informed by prior work in the San Luis Pass area (Nicholson, 2012). The resulting structure map of the top of the model interval is shown in figure 2.3.3. The area shown in the structure map represents the dynamic reservoir model area (DRMA), the extent of which is important in subsequent regional-reservoir comparisons.

Dynamic Model Algorithm

The model algorithm used for the simple dynamic analytical calculation was developed by Jain and Bryant (2011) and considers simplified reservoir properties to calculate cumulative CO_2 injected with time for a given reservoir. The model algorithm requires reservoir inputs for:

S_{wirr}	irreducible water saturation
φ	porosity
T	temperature
P	pressure

Z	depth
κ	permeability
h	thickness
A	area
μ_w	water viscosity
μ_g	gas viscosity
k	salinity
n	Corey model relative permeability exponent
m	Corey model relative permeability exponent
K^o_{rg}	end point gas saturation
P_l	injection pressure limit
ρ	CO_2 density at reservoir conditions

The Jain and Bryant (2011) model algorithm assumes that properties are homogeneous throughout the reservoir. Reservoir structure is not considered in the calculation. In the model, the geometry of the input area for the reservoir is idealized and represented as a square with an area matching that of the input parameter. The well array is assumed to be a continuous line of injectors intersecting the midpoint of two opposite sides of the square (figure 2.3.4). Relative permeability between CO_2 and water is assumed to be uniform and is calculated in the model algorithm using the Corey-type model (Corey, 1954; Burton et al., 2008) by specifying inputs of n, m, K^o_{rg}, and S_{wirr} in the following equations:

$$K_{rw} = \left[1 - \left(\frac{1-S_w}{1-S_{wirr}}\right)\right]^m \qquad (12)$$

and

$$K_{rg} = K^o_{rg}\left(\frac{1-S_w}{1-S_{wirr}}\right)^n \qquad (13)$$

Boundary conditions are assumed to be open at the edges of the square reservoir parallel to the line of injectors, and closed at those boundaries that are perpendicular to the injection line. The model assumes that CO_2 moves with a Buckley-Leverett type front (Buckley, 1942). Here, CO_2 flow is assumed to be piston-like with uniform areal and vertical sweep efficiency and uniform gravity override. Open boundaries, homogeneous properties and high sweep efficiencies result in overly optimistic capacity estimates, and for this reason Jain and Bryant (2011) indicates that results from these calculations should be scaled similar to an efficiency factor.

In the simulation, wells inject CO_2 at a constant pressure, which is defined by the P_l parameter. Injection continues until one of 3 scenarios occurs: (1) the CO_2 plume front migrates to the edge of the reservoir, (2) the pressure limit (P_l) is reached at the edge of the reservoir, or (3) 100 years elapse. When any of these conditions are met, the simulation is ended and the run is flagged to specify which of the three scenarios occurred.

Model Input

The Jain and Bryant (2011) model assumes that, within the areal extent of the injected CO_2 plume, the end point saturation is reached and the reservoir is uniformly filled with CO_2. Because this scenario is most likely to occur only in an area where injected CO_2 is trapped within an enclosure, the dynamic calculation is only applied to the closure areas observed in the model horizon. Closure and fetch area analysis is performed on the top of the reservoir interval using Permedia software (figure 2.3.5). A fetch area is defined as an area in which all points drain updip to a common closure. In this case, a fetch area represents a common area of updip CO_2 migration and accumulation. CO_2 migrates updip because of gravity effects driven by the density

contrast between supercritical CO_2 (0.6-0.8 g/cc) and brine (~1.1 g/cc). Supercritical CO_2 is buoyant in the reservoir and migrates to the shallowest areas with time. Spill points are located where a fetch area outline meets the outline of its corresponding closure area. If filled to a spill point, a closure can no longer contain additional CO_2. The areas of closures 1-4 are, as used in this study, are as follows:

Closure 1 2,566 acres (10.4 km^2)

Closure 2 909 acres (3.7 km^2)

Closure 3 582 acres (2.4 km^2)

Closure 4 685 acres (2.8 km^2)

An input thickness of 99.5 feet (30.3 meters) for the reservoir interval is determined using the average isopach value between the upper and lower reservoir seismic horizons within the combined area of closures 1-4 (4,742 acres [19.2 km^2]). An input depth of 4,828 feet (1,472 meters) is determined by averaging the horizon depth values of the top of the model reservoir within the combined closure area, and adding half of the input thickness to approximate the midpoint of the reservoir. Using the bottom hole temperature from raster log well headers in 11 wells, the following average temperature gradient is calculated:

$$T = 0.01256Z + 75, \qquad (14)$$

where,

T=temperature (Fahrenheit)

Z=depth (feet)

The calculated input depth is used for Z in equation 14 and an average reservoir temperature of 135.6° F (57.6° C)is obtained.

By observing the pressure trend of the offshore Miocene reservoirs studied by Nicholson (2012) (figure 2.2.2), reservoirs at depths ~10,000 feet (3,048 meters) are typically near hydrostatic pressure. Thus, with the absence of any available pressure data, the following hydrostatic pressure gradient is used to calculate an average reservoir pressure:

$$P_h = 0.433Z + 14.696, \qquad (15)$$

where,

P_h=Hydrostatic pressure (psi)

This pressure gradient assumes water density of 1 g/cc and surface pressure of 14.696 pounds/in^2 (psi) (101.3 Kpa). The resulting reservoir pressure calculated for the input depth is 2,105 psi (14.5 Mpa).

The fracture pressure of a reservoir can typically be estimated to be 70-90% of lithostatic pressure (Du Rouchet, 1981). Stuart (1960) found that the fracture pressure in the Gulf of Mexico is roughly 85% of lithostatic or greater. Because injection pressure of CO_2 should not reach the fracture pressure of the reservoir, we assume an injection pressure limit of 80% of lithostatic pressure. This pressure limit is referred to as the fracture pressure in our study. A lithostatic pressure gradient is determined for the DRMA by integrating a density curve from well A. Because no bulk density curve is available for this well, an approximate density curve is calculated from the existing sonic curve using the following equation (Gardner et al., 1974):

$$\rho = .23V^{.25} \qquad (16)$$

where,

ρ=Bulk density (g/cc)

V=Velocity (from sonic log) (ft/s)

Pressure is calculated by integrating the resulting density curve with respect to depth from 0 to 6,000 feet (0 to 1,829 meters) using a 1 foot (.3 meter) increment. Because the sonic converted density log begins at a depth of 795 feet (242 meters), a constant density of 1.967 g/cc is used from 0-795 feet (0-242 meters) (i.e., value of the first reading). A best fit linear curve is plotted through the data (figure 2.3.6) and the following equation is found to describe the trend with an R^2=0.999:

$$P_{lith} = .91Z + 14.696 \qquad (17)$$

where,

P_{lith}=Lithostatic pressure (psi)

Equation 17 is applied to the reservoir depth to obtain a lithostatic pressure of 4,409 psi (30.4 Mpa) and an injection pressure limit of 3,527 psi (24.3 Mpa).

Salinity is calculated from water resistivity using the deep induction resistivity log (ILD) in well A (figure 2.3.2) in order to constrain brine density and viscosity. Water resistivity is calculated using Archie's law (Archie, 1942):

$$R_t = \frac{a}{\Phi^m}\frac{1}{S_w{}^n}R_w \qquad (18)$$

where,

R_t=Measured resistivity from ILD log (ohm·m)

a= Tortuosity factor (assume 1)

m=Cementation exponent (assume 2)

S_w=Water saturation (assume 1 since zone is water bearing)

n=Saturation exponent (assume 2)

R_w=Water resistivity

A porosity value of 0.33 is calculated over the interval by obtaining an average sonic reading of 110 μs/foot within the reservoir from well A and applying equation 2. An

average R_t reading of 0.231 ohm·m is observed over the reservoir interval and, using equation 18, an R_w of 0.025 ohm·m is calculated. A temperature of 146° F (63.3° C) is obtained by applying equation 14 to the midpoint depth of the reservoir interval observed in well A (5,661 feet [1726 meters]). Using the calculated Rw and T along with Schlumberger's Resistivity Nomograph for NaCl Solutions (2000), a water salinity of 190,000 ppm is obtained.

CO_2 and brine viscosities are calculated using the National Institute for Standards and Technology Chemistry WebBook (Fenghour et al., 1998; NIST, 2011) (CO_2) and the Consortium for Research in Elastic Wave Exploration Seismology (CREWES) Fluid Property Calculator (Batzle and Wang, 1992; Ursenbach, 2007) (brine), with the P, T, and salinity inputs obtained above. Parameters μ_w and μ_g are found to be 0.8177 cP (0.8177 mPa·s) and 0.0467 cP (0.0467 mPa·s), respectively.

Porosity, permeability, and irreducible water saturation inputs cannot be confidently constrained for the study area. To observe the effect of these unknown parameters and to better understand the potential range of capacity the Jain and Bryant (2011) calculation is repeated with varying samples of φ, κ, and S_w. All other inputs are held constant. Samples of φ, κ, and S_w are obtained from the Atlas of Northern Gulf of Mexico Gas and Oil Reservoirs (Seni, 2006). For the purposes of this study, we assume that water saturation measured in the gas reservoir is equal to the irreducible water saturation in the presence of CO_2. For each reservoir in the atlas dataset, a single value of φ, κ, and S_w is reported. The φ, κ, and S_w measurements for 6,206 unique offshore Gulf of Mexico Miocene-aged gas reservoirs are extracted from the dataset for subsequent processing. The statistical distribution for each parameter of these data samples is shown in figure 2.3.7 along with crossplots showing the empirical relationship between φ, κ, and

S_w observed in the dataset. Note that permeability is distributed logarithmically and is displayed as $\log_{10}$Permeability. Each triplet of φ, κ, and S_w for the 6,206 reservoir samples is used as the input variable for a single simulation with all other inputs remaining constant in each calculation. The result is 6,206 individual simulations in which the φ, κ, and S_w from one of each of the 6,206 analog reservoirs is applied. φ, κ, and S_w remain associated for each reservoir, which allows the simulation to more accurately portray the range of possible reservoir properties. If these properties are sampled independently, the natural relationship among porosity, permeability, and water saturation (figure 2.3.7) is ignored and the simulation results for some simulations could become less realistic (depending on the sampled parameters). Though porosity is measured from sonic data in well A, using multiple samples from a dataset acquired over the region of interest yields a distribution of results that is more broadly applicable when used for regional comparison. This method is not a traditional Monte Carlo simulation, and is in no way related to the Monte Carlo simulations described in Chapter 2.2 that are used to determine E.

Measurements for n, m, K^o_{rg} used to generate CO_2-water relative permeability curves are not available in or near the study area. Instead, these parameters are chosen to match the base case curves used in the Lawrence Berkeley National Laboratory inter-comparison project (Pruess et al., 2002; Zeidouni et al., 2009). Because the inter-comparison project curves are created using a Mualem (1976) (water) and modified Corey (1954) (gas) permeability model, the relative permeability curves generated in the Jain and Bryant calculation (Burton et al., 2008) do not match perfectly. However, the two curves overly one another closely (figure 2.3.8), using 2.6, 10, and 1 for n, m, and K^o_{rg}, respectively. These parameters are held constant while varying Sw_{irr}, which is

extracted from the S_w data in the 6,206 Miocene reservoir samples and used to calculate a set of relative permeability curves for each model run. The extracted S_w value is used in a model calculation with the corresponding values of φ and κ for that reservoir.

Simulation output for each model calculation includes a fill time and injected volume of CO_2. To compare volumetric results, CO_2 density is calculated at reservoir conditions and multiplied by the injected volume. Because volume is reported at the end of injection when pressure is elevated, CO_2 density is calculated for the reservoir pressure limit (3527 psi [24.3 Mpa]). Though this pressure may not be uniform across the entire reservoir and thus overestimate density, most of the reservoir is likely at or very near the pressure limit. Temperature changes are not considered by the model and the input reservoir temperature of 135.6^o F (57.6° C) is used in the calculation of CO_2 density. The NIST calculator is used with a Span and Wagner (1996) equation of state to determine a density of .792 g/cc. Table 2.3.1 summarizes the inputs used in the 6,206 model calculations.

Table 2.3.1: Summary of input parameters for the simple dynamic analytical model. φ, κ, and S_w are populated for 6,206 offshore Miocene reservoirs from the Atlas of Northern Gulf of Mexico Gas and Oil Reservoirs (Seni, 2006). Each set of φ, κ, and S_w is used for an individual model calculation.

Summary of Simple Dynamic Analytical Model Inputs			
Parameter	**Property**	**Value**	**Source**
S_{wirr}	Irreducible Water Saturation	10-78%	6,206 Miocene reservoirs
Φ	Porosity	0.12-0.37	6,206 Miocene reservoirs
T	Temperature	135.6° F (57.6° C)	11 log headers in DRMA
P	Pressure	2,105 psi (14.5 Mpa)	Hydrostatic gradient
Z	Depth	4,828 feet (1,472 meters)	Seismic mapping
κ	Permeability	0.08-3686 mD (7.9×10^{-17} -3.6×10^{-12} m^2)	6,206 Miocene reservoirs
h	Thickness	99.5 feet (30.3 meters)	Seismic mapping
A	Area	4742 acres (19.2 km^2)	Closure analysis
μ_w	Water Viscosity	0.8177 cP (0.8177 mPa·s)	CREWES calculator
μ_g	Gas Viscosity	0.0467 cP (0.0467 mPa·s)	NIST calculator
k	Salinity	190,000 ppm	ILD and DT (well A)
n	Corey exponent (gas)	2.6	Inter-comparison project
m	Corey exponent (water)	10	Inter-comparison project
K^o_{rg}	End point gas saturation	1	Inter-comparison project
P_l	Pressure limit	3,527 psi (24.3 Mpa)	80% of lithostatic pressure
ρ	CO_2 density	.792 g/cc	NIST calculator

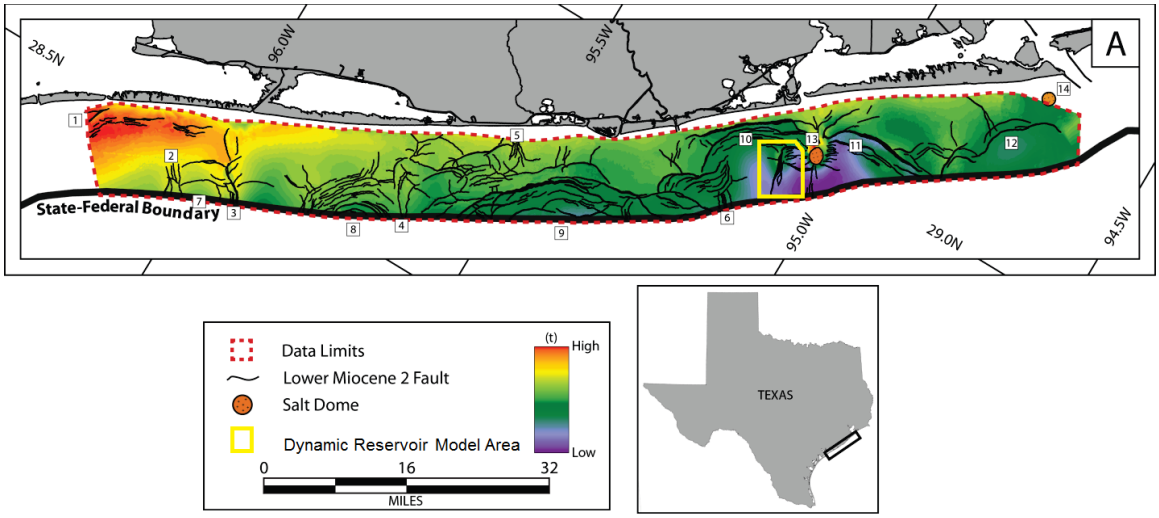

Figure 2.3.1: Time structure and faults of LM2 horizons (modified from Nicholson,2012). Yellow box indicates site selected for dynamic modeling.

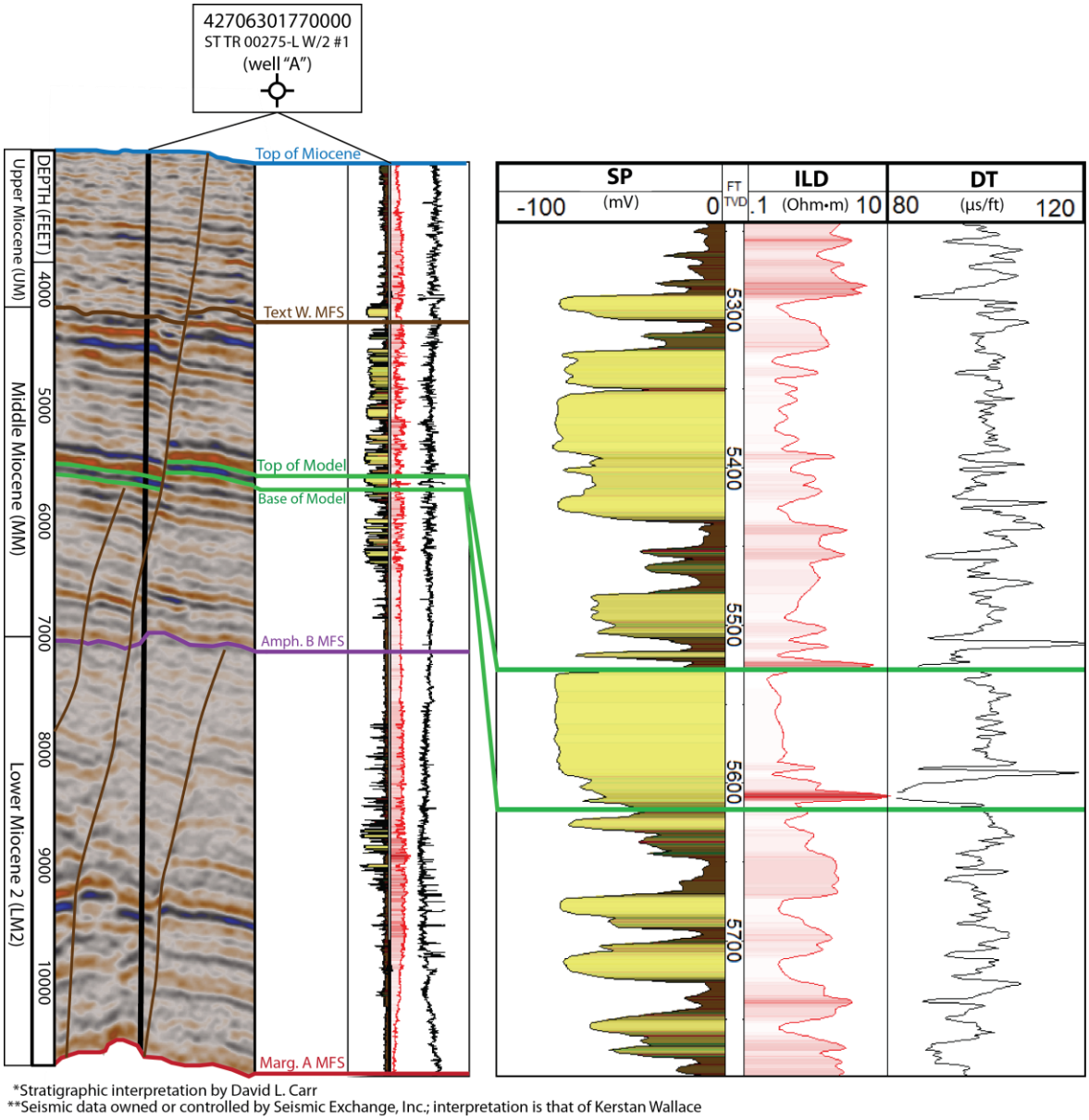

Figure 2.3.2: Seismic column and corresponding well log from well 42706301770000 (well A). Expanded log section shows reservoir interval. Location of well A is shown in figure 2.1.1 and 2.3.3.

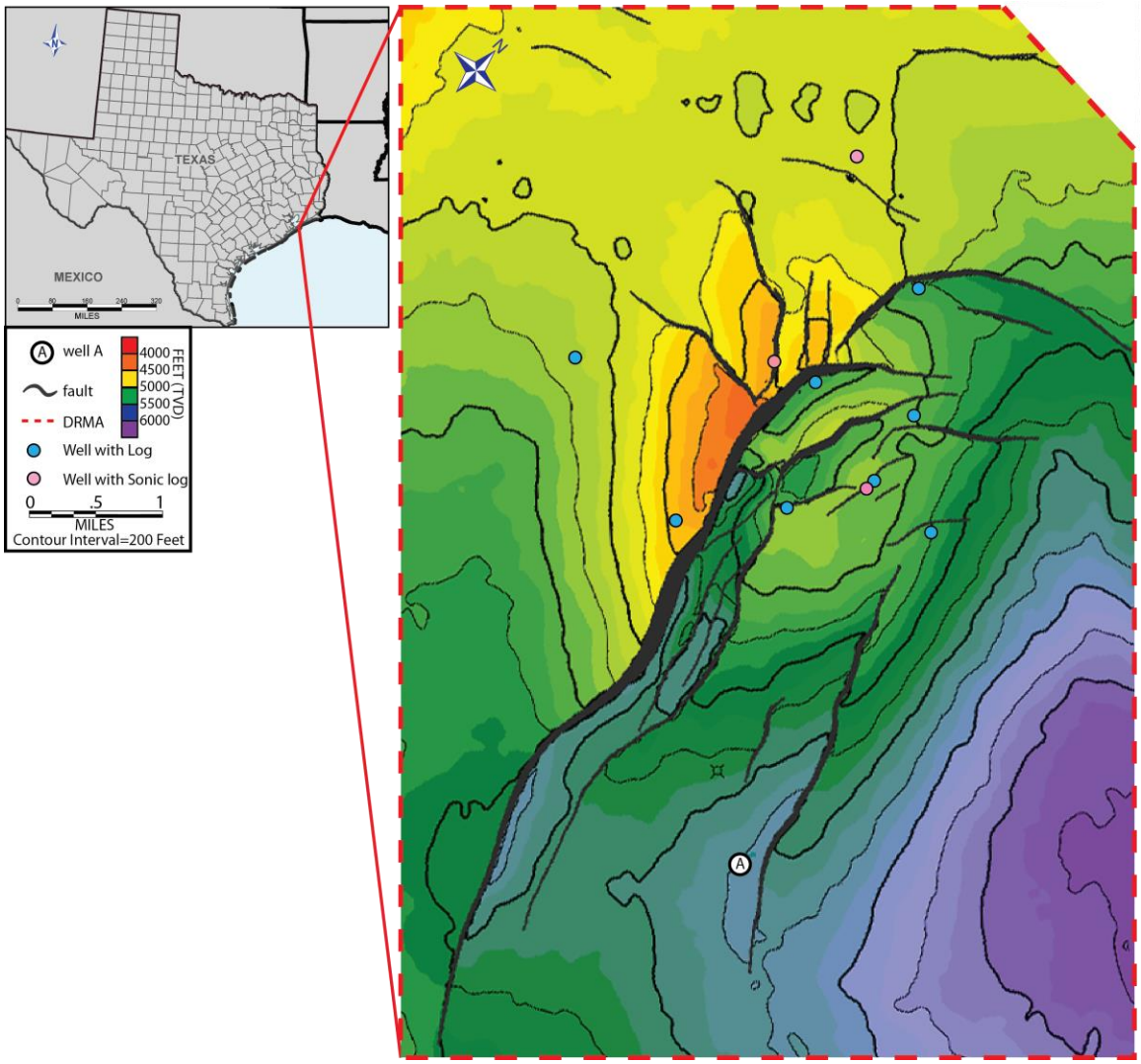

Figure 2.3.3: Structure map of the top of model interval. The location of the well A is shown along with the locations of wells with logs (blue). Wells with sonic logs (in addition to well A) are highlighted in pink.

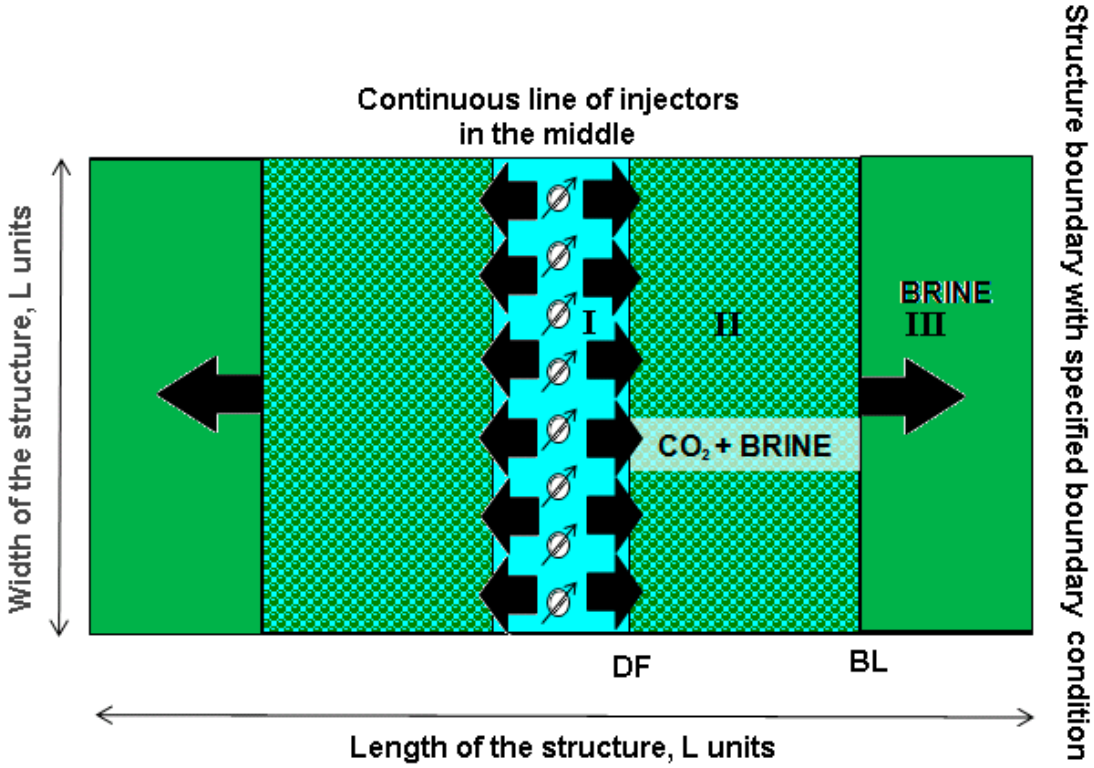

Figure 2.3.4: Schematic illustration showing map view of well array and CO_2 flow direction from Jain and Bryant (2011).

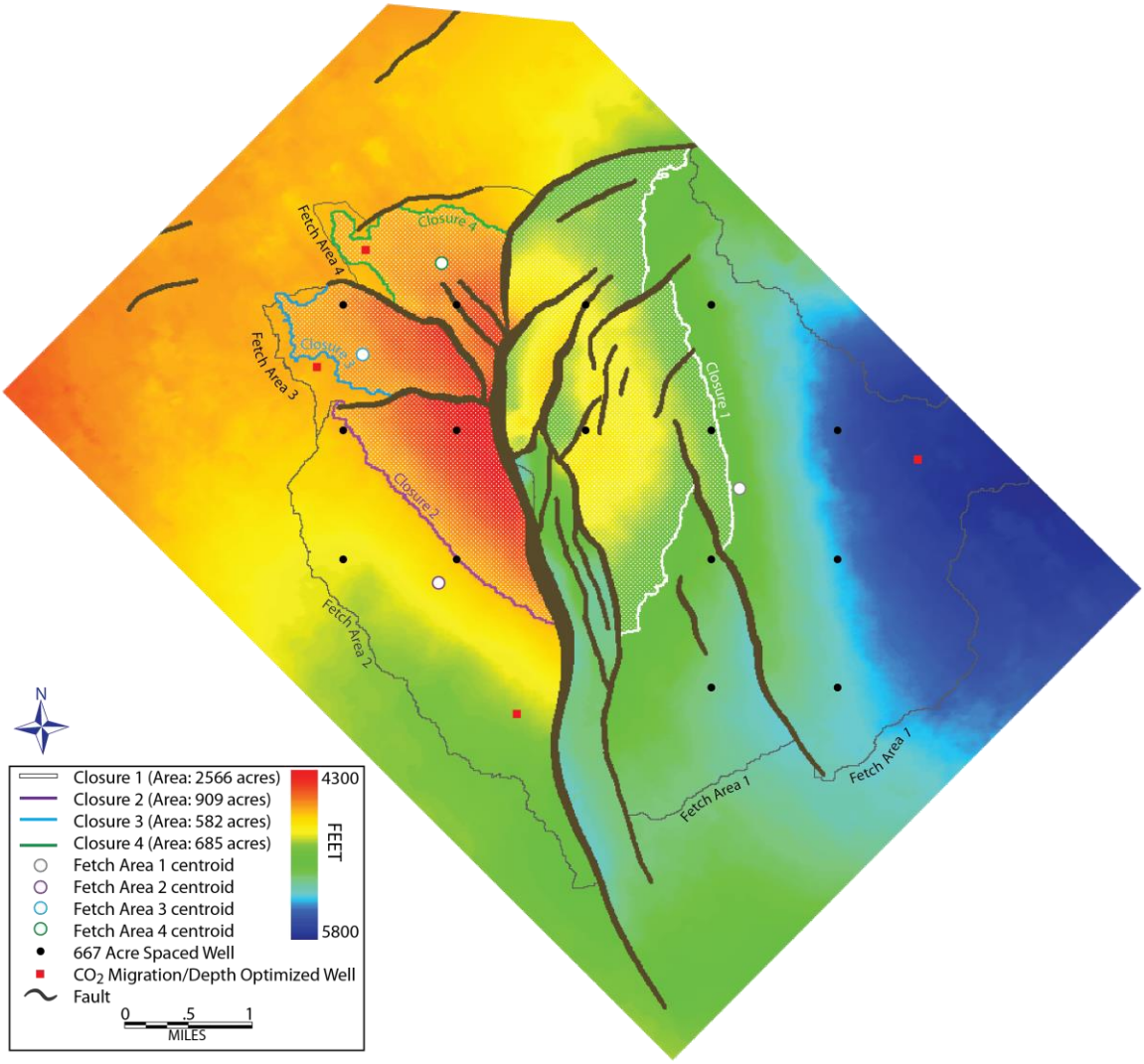

Figure 2.3.5: Closure and fetch area polygons plotted with subsurface structure of the top of the model interval.

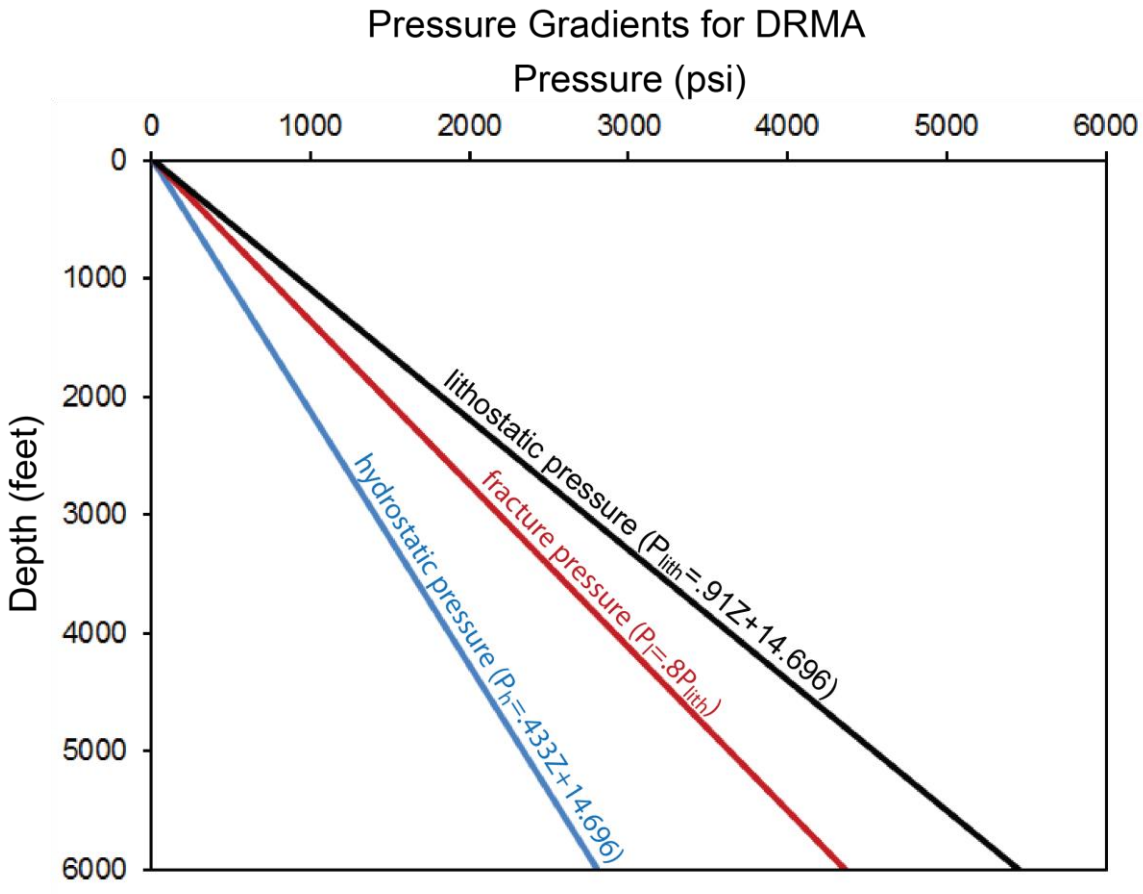

Figure 2.3.6: Pressure gradients used in DRMA.

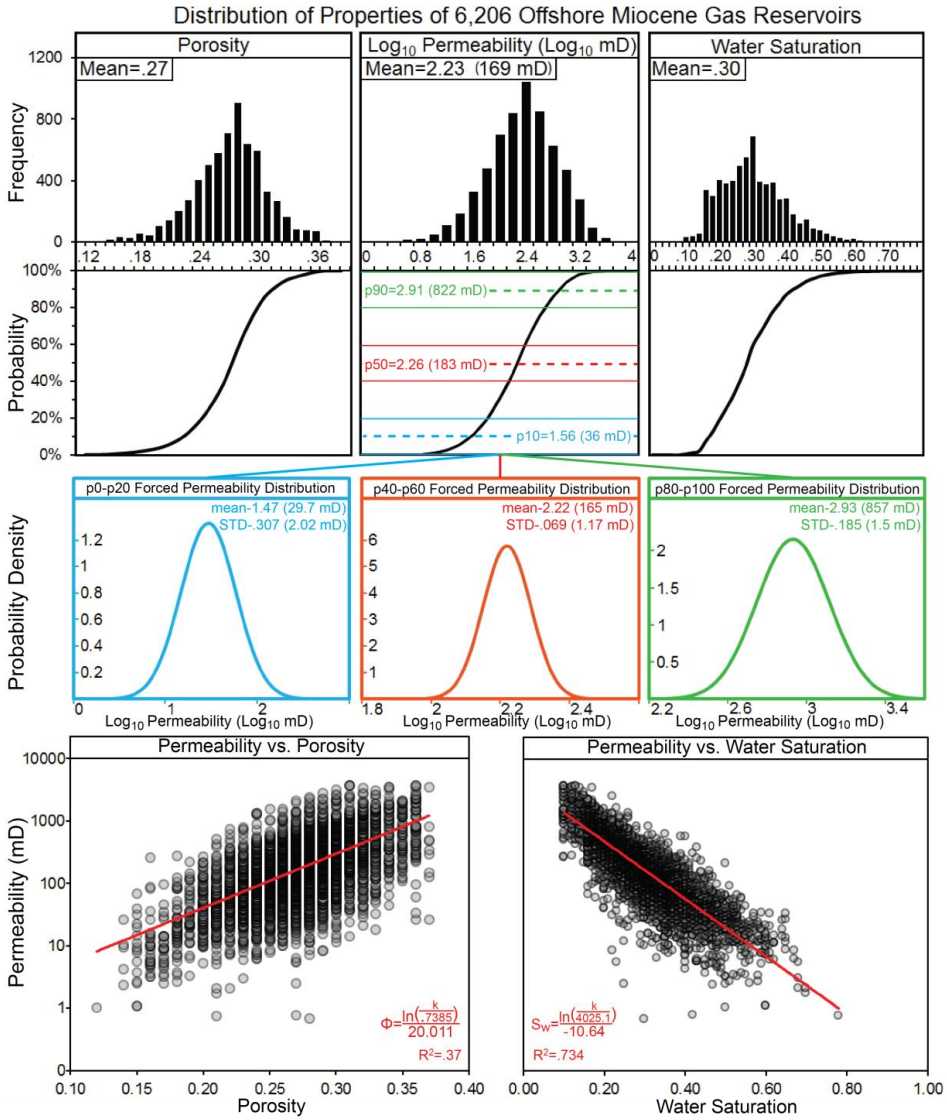

Figure 2.3.7: Distribution and relationships of the reservoir properties of the Miocene subset of 6,206 gas reservoirs from the Atlas of Northern Gulf of Mexico Gas and Oil Reservoirs (Seni, 2006). From top to bottom the rows of plots show (1) histogram distribution of porosity, permeability and water saturation, (2) cumulative distribution probability plots of porosity, permeability, and water saturation, (3) probability density of permeability for P_0-P_{20}, P_{40}-P_{60}, and P_{80}-P_{100} ranges, and (4) cross plots of permeability vs. porosity and permeability vs. water saturation.

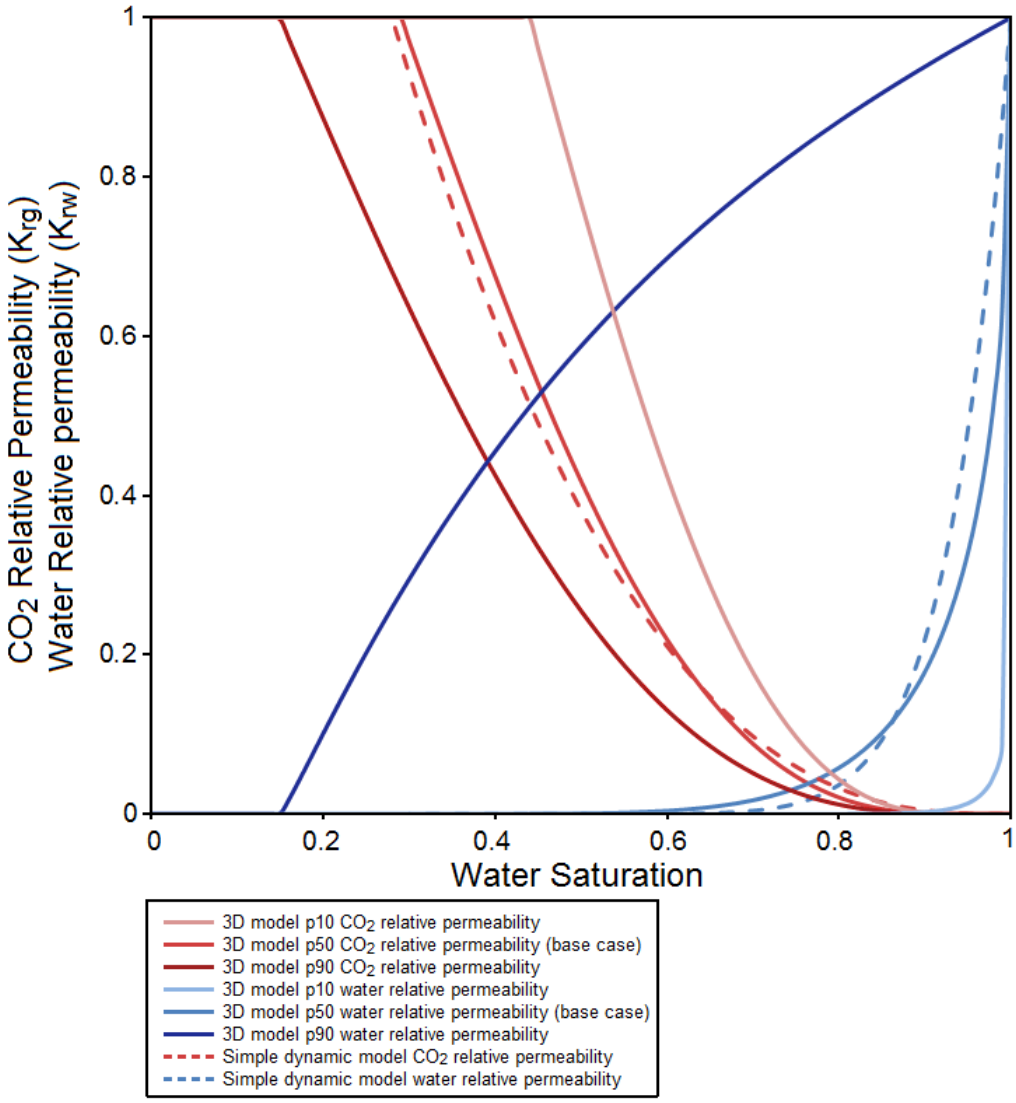

Figure 2.3.8: Relative permeability curves for simple dynamic model (dashed) and 3D flow model (solid). Base case curves are shown for the 3D dynamic flow model and high and low reservoir quality cases used in additional model cases. Simple dynamic relative permeability is plotted here with a Sw = 0.29 to match the 3D flow model base case.

CHAPTER 2.4: 3D DYNAMIC FLUID FLOW SIMULATION

3D flow simulations are performed in CMG (Computer Modelling Group; version 2012.10; Calgary, AB) using the DRMA interval and location. A total of 27 model cases are simulated to capture the potential range of capacity with the variation of unconstrained parameters. In general, these cases are divided into 3 model scenarios: homogeneous, statistically heterogeneous, and seismic-based heterogeneous. A base case along with 8 variation cases is designed for each of the 3 model scenarios to produce the 27 model cases ([1 base case + 8 variation case] x 3 scenarios). The 8 variation cases are chosen to test the effect of the unknown parameters that are suspected to have the largest influence on CO_2 storage capacity. The goal of the dynamic flow simulations is to observe the CO_2 plume volume and distribution along with the pressure distribution in 3 dimensions with time and estimate reservoir capacity from the injection totals. The model cases do not represent Monte Carlo simulation and population of the 3D models is separate from the population of the simple dynamic analytical model. Any overlap between the 3D model and simple dynamic analytical inputs is explicit.

Model Generation

Using the upper and lower seismic horizons discussed in Chapter 2.3, a grid mesh is generated in DecisionSpace (Halliburton; version 5000; Houston, TX) (figure 2.4.1). A total of 288,781 grid blocks are created by using 10 evenly spaced layers between the two reservoir surfaces and a cell size of 200 x 200 feet (61 x 61 meters) in the *i* and *j* directions. The *k* dimension at each cell location is determined by the thickness of the reservoir divided by 10 (number of layers). The average grid cell thickness is 9.5 feet (2.9 meters). Fault locations are stored in the grid mesh, and cells located within a fault gap

are left null. This reservoir mesh is used for all subsequent modeling. Only the properties within the grid cells are altered.

Homogeneous Model Scenario

The homogeneous model base case assumes constant values of porosity and permeability. The permeability value is chosen from the distribution of properties of the 6,206 reservoirs (Chapter 2.3). The P_{50} permeability value of 183.66 mD (1.8×10^{-13} m^2) is selected from the cumulative probability distribution for use in the base case (figure 2.3.5). Permeability in the *i* direction is set to equal permeability in the *j* direction (horizontal isotropy). Permeability in the *k* direction is set to equal 20% of the permeability in the *i* and *j* direction (vertical anisotropy such that Kv/Kh is everywhere = 0.2). Though the P_{50} permeability value represents a measurement in a discrete reservoir sample in the 6,206 reservoir dataset with corresponding porosity and water saturation values, these porosity and water saturation values are not selected for use in the base case as they may be anomalously high or low. That is, the porosity and water saturation associated with the P_{50} permeability reservoir might not accurately reflect the broader trend observed in the empirical relationship among porosity, permeability, and water saturation. To preserve the relationship between these parameters, the following equations, derived from the cross plots in figure 2.3.7, are applied to the P50 permeability value:

$$\varphi = \frac{\ln\left(\frac{k}{.7385}\right)}{20.011} \qquad (19)$$

and

$$S_w = \frac{\ln\left(\frac{k}{4025.1}\right)}{-10.64} \qquad (20)$$

Using equations 19 and 20 with the P_{50} permeability value of 183.66 mD (1.8×10^{-13} m^2), base case porosity and water saturation values of 0.275 and 0.29 are calculated, respectively.

CO_2-water relative permeability curves are generated using the base case assumptions from Zeidouni et al. (2009), where the gaseous phase is calculated using the Corey curve (1954):

$$k_{rg} = \left(1 - \hat{S}\right)^n \left(1 - \hat{S}^n\right) \qquad \text{where:} \qquad \hat{S} = \frac{S_w - S_{wirr}}{1 - S_{wirr} - S_{gc}}, \qquad (21)$$

where,

k_{rg}=Relative permeability of gas in the presence of water

S_w=Saturation of the aqueous component

S_{gc}=Gas saturation downstream of the trailing shock of CO_2 (~.05) (Zeidouni et al. 2009)

n=Empirical permeability exponent

And the aqueous phase is calculated using the function proposed by Mualem (1976):

$$k_{rw} = \sqrt{S^*}\left(1 - \left(1 - [S^*]^{1/\lambda}\right)^{\lambda}\right)^2 \qquad \text{where:} \qquad S^* = \frac{S_w - S_{wirr}}{1 - S_{wirr}}, \qquad (22)$$

where,

k_{rw}=Relative permeability of water in the presence of gas

λ=Empirical permeability exponent

The base case assumes values of λ =0.457, n=2, Sw_{irr} is assumed equal to S_w of 0.29, calculated with equation 20. Figure 2.3.8 shows the base case relative permeability curves.

Well placement is determined using the closure analysis discussed in Chapter 2.3. In the base case scenario, each of 4 wells used (1 well per closure) are located at the centroid of a fetch area polygon (figure 2.3.5). The wells are designated well 1-4, with

the value corresponding to the numbered fetch areas and closures. These well locations provide the greatest likelihood that injected CO_2 will remain in the study area while avoiding extreme proximity to faults. All injected CO_2 must remain within the study area for subsequent meaningful model comparisons. Though it is technically impossible for CO_2 to leave the reservoir in the simulator, if CO_2 reaches the edge cells, then we assume it has migrated outside the simulated area and the resulting capacity is not used for comparison.

Injection rate in the base case model is variable and controlled by a constant pressure limit. Pressure should not exceed fracture pressure at any point in the reservoir during injection. The divergence in hydrostatic and fracture pressure gradients (figure 2.3.6) suggests that shallower points will fracture with a smaller pressure change (ΔP) above hydrostatic pressure than deeper points. To ensure that the shallowest portion of the reservoir model does not reach the fracture pressure, a trial-and-error method is used to determine the pressure limits for each well. For every simulation, a model is run with well injection pressure limits equal to the fracture pressure. This injection pressure limit is calculated for the reservoir depth at each well location using equation 17 to determine lithostatic pressure and multiplying by 0.8 to obtain fracture pressure (pressure calculations explained in Chapter 2.3). At the shallowest grid cell in each resulting model, the final pressure is obtained. The fracture pressure for this cell is calculated and subtracted from the modeled final pressure. This difference is then subtracted from the fracture pressure calculated for each well location. All models are then run again using these modified pressure limits. The base case pressure limits then become:

Well 1 3,510 psi (24.2 Mpa)

Well 2 3,243 psi (22.4 Mpa)

Well 3 3,107 psi (21.4 Mpa)

Well 4 3,131 psi (21.6 Mpa)

Each well injects CO_2 at its calculated pressure limit for the duration of the simulation (up to 100 years). This trial and error method is selected for the determination of pressure limits to maximize the injection rates without ever exceeding fracture pressure at the shallowest point in the reservoir. Due to software limitations, it is not currently possible to assign a pressure monitoring well to the shallowest point in the reservoir for the purpose of limiting injection from other wells. Though it is possible to add the maximum allowable ΔP for the shallowest point in the reservoir to the hydrostatic pressure at each well location, the resulting pressure limits will be lower than necessary because pressure does not fully equilibrate over 100 years. Thus, it is not possible to easily predict the maximum pressure limit without first running a trial simulation.

Initial reservoir temperature is assumed to be uniform at 135.6^{o} F (57.6° C) (described in chapter 2.3). Initial reservoir pressure is calculated as a function of depth using a hydrostatic pressure gradient (equation 15). Thermodynamic fluid properties such as critical temperature and pressure, viscosity, density, binary interaction coefficients, solubility, etc. are populated using the default fluid model for CO_2 and brine in CMG. Additional assumptions of the base case include closed boundaries and zero fault transmissibility. The homogeneous base case model inputs are summarized in table 2.4.1.

The base case model is varied 8 times to test the importance of variable inputs and to determine a possible range of capacity results. Again, it is important that the effect of unknown parameters be understood, and through these variation cases, a range of capacity can be obtained for this refinement step. The model cases evaluated in addition to the base case are (1) high quality reservoir, (2) low quality reservoir, (3) open

boundary conditions, (4) open fault transmissibility, (5) single injection well, (6) 15 injection wells, (7) optimized well placement, and (8) constant injection rate.

Cases 1 and 2 are created using geologic values from the aggregated Miocene subset atlas data. The high reservoir quality scenario is populated with the P_{90} permeability value of 822 mD (8.1×10^{-13} m^2). Corresponding values of porosity and water saturation are calculated using equations 19 and 20, and are found to be 0.35 and 0.149, respectively. The aqueous phase relative permeability coefficient, λ, is also increased to reflect the overall increase in reservoir quality. A new value of 2.557 is selected from the high end member value used by Zeidouni et al. (2009). Case 2 is calculated much the same way as Case 1. A P_{10} permeability value of 36.13 mD (3.5×10^{-14} m^2) is used to calculate porosity and water saturation values of 0.194 and .443, respectively. Parameter λ is decreased to 0.157, the low end member used by Zeidouni et al. (2009). The high and low quality reservoir relative permeability curves are shown in figure 2.3.8.

Cases 3 and 4 test the effect of pressure barriers. Case 3 (open boundaries) is created by applying a volume modifier of 10,000 to the edge cells of the reservoir model. Though the displayed geometry remains intact, any CO_2 flow or pressure change in these modified cells is calculated using a volume 10,000 times the actual volume. Case 4 (completely transmissive faults) is achieved by assigning a transmissibility of 1 to all faults.

Case 5 and 6 test the effect of the number of wells used for injection. The location of the single well used in Case 5 is the same as well 1 in the base case. Case 6 is aimed to observe the outcome of a maximum well scenario. The legal maximum is constrained by the Texas Administrative Code, Title 16, Part 1, Chapter 3, Rule §3.37, which states, “No

well for oil, gas, or geothermal resource shall hereafter be drilled nearer than 1,200 feet to any well completed in or drilling to the same horizon." This minimum well spacing would require 318 wells to populate the fetch areas within the DRMA. The high cost of offshore wells is assumed to hinder this kind of development, making this maximum value unrealistic. Instead, a maximum well count of 15 is selected for the purpose of creating a hypothetical scenario. Though drilling 15 individual wells for CCS in this single structure is still unlikely, the number should allow for contrast and comparison to the single well case and base case (4 well). The 15 wells are evenly spaced by a distance of 5,390 feet (1,643 meters) within the fetch areas (figure 2.3.5).

The optimized well placement tested in case 7 is determined primarily by two factors, CO_2 migration distance and well depth to reservoir. By maximizing the travel length of migrating CO_2, the potential for capillary trapping and CO_2 dissolution in brine is increased because additional surface area is encountered by the CO_2. Maximizing the injection depth creates a greater allowable pressure increase, which can be seen in the divergence of the hydrostatic and lithostatic curves (figure 2.3.6). Also, high pressure injection in deep wells results in increased CO_2 density that mitigates pressure buildup through smaller injection volumes. Thus, to maximize well placement, the deepest well locations with the greatest distance to the edge of a closure area are selected. The distance of the CO_2 travel path is assessed using the fill spill tool on the top reservoir horizon in Permedia. This tool shows the length of the buoyancy driven flow path for any selected point on the horizon and the resulting accumulation within a closure. To uniformly test each fetch area, each cell along the buffered perimeter of the fetch area polygon is tested. A buffer is used to avoid the placement of wells so near to the edge of the fetch area that CO_2 could migrate outside of the study area. The size of the buffer is determined by

running preliminary simulations and measuring the maximum plume radius in the downdip direction. This distance is found to be 2,545 feet (776 meters). In all fetch areas, the longest travel paths were very near the deepest points. The resulting optimized well placement is shown in figure 2.3.5.

The constant injection rate used in case 8 is determined from an initial model run performed on the homogeneous base case. The total injected CO_2 for each well is divided by the length of injection (100 years) and used as the new constant injection rate. The rates calculated are as follows:

Well 1	81.6 tonnes/day
Well 2	33.6 tonnes/day
Well 3	13.6 tonnes/day
Well 4	18.5 tonnes/day

This method is repeated for the statistical heterogeneous and seismic-based heterogeneous base cases to determine the respective constant injection rates. The base case injection pressure limit for each well is set as a second condition for injection. If, while injecting at a constant rate, pressures were to reach the set limit, injection rate are then adjusted to maintain, but not exceed, the maximum pressure at the well bore.

Statistically Heterogeneous Model Scenario

The primary difference between the homogeneous model and the statistically heterogeneous model is the introduction of random heterogeneity in the porosity and permeability fields. As in the homogeneous case, a heterogeneous base case model is generated and deviated by the 8 case variations discussed previously. This only requires the modification of the base case, along with cases 1, 2, and 7. Though cases 3, 4, 5, 6,

and 8 require that the mesh properties be updated to match the statistically heterogeneous base case, they do not require any change in the case set up.

The permeability field is populated using a range of values from an idealized "forced normal" distribution, which, in this study, refers to the use of a normal distribution curve generated by a Microsoft Excel (Microsoft; version 2010; Redmond, WA) function to describe non-normally distributed data. Specifically, this refers to the extraction of the mean and standard deviation of a subset of permeability data within a specific probability range for use in the norminv Excel function. This function generates a bell curve from which values with a given probability are extracted. Using the norminv Excel function with random numbers between 0 and 1 as the input probability values results in a population of random permeability values that have a normal distribution with a mean and standard deviation matching the input mean and standard deviation. Though the use of random numbers as input probabilities oversamples the tails of the normal distribution curve, the steep slope of the cumulative probability curve over the mean greatly reduces any impact of the oversampling on the resulting permeability distribution. Again, it is important to remember that the goal of this permeability population is merely to introduce random heterogeneity and observe the effect on capacity. Whether or not the distribution of the permeability values used in the population of the 3D model is completely representative of the 6,206 Miocene reservoir subset is not of great importance. Because the 6,206 permeability measurements are each for different reservoirs and do not represent the distribution of a permeability field for a single reservoir, matching this dataset is, again, not necessary. The primary use of this data in the generation of 3D models is to obtain reasonable permeability ranges for different reservoir qualities observed in the region. Though the forced normal distribution does not

represent the true distribution of the data in this case, it allows for the population of reservoir mesh cells with random permeability values that fall within a narrow range of values and have an expected mean. For the purposes of this study, this is sufficient to create the intended heterogeneous permeability field for an average (base case), high quality (case 1), and low quality (case 2) reservoir.

For the base case, a mean and standard deviation is taken from the P_{40}-P_{60} permeability values in the Miocene subset from the offshore atlas. This mean and standard deviation are used in the norminv Excel function which is applied with no local correlation to 288,781 random numbers (one for each cell of the reservoir mesh). Note that the logarithmic distribution of permeability requires that the norminv function is applied using the $\log_{10}$Permeability mean and standard deviation. The calculated $\log_{10}$Permeability is afterwards converted back to natural values. Figure 2.3.7 illustrates the range of the cumulative probability values from which the mean and standard deviation are obtained for use in the resulting base case forced normal permeability distribution (shown in red). Porosity is populated by applying equation 19 to the permeability values. In this way, cells with high permeability also have high porosity. Each of the 10 model layers is populated by this process, creating variations of permeability both horizontally and vertically (figure 2.4.2). Permeability is only populated in the *i* direction; the *j* direction is set to equal *i* and the *k* direction is set to equal 20% of *i*.

Cases 1 and 2 (high and low quality reservoir) are created by repeating the steps used in populating the heterogeneous base case, only with different values for the average and standard deviation used to generate forced normal distributions for populating permeability. The high quality reservoir is populated by taking the mean and standard

deviation of the Miocene reservoir subset with permeability values in the P_{80}-P_{100} range. The low quality reservoir uses the mean and standard deviation from the P_0-P_{20} permeability range. Again, the data samples within these ranges alone do not have a natural normal distribution; they are forced into a normal distribution for the purposes of populating heterogeneous models with relatively low, average, and high quality reservoir properties. The same random numbers used in the norminv function to generate permeability in the base case are used for the high and low quality reservoirs. This creates a consistent permeability distribution between the base case and cases 1 and 2; only the scale of permeability values changes. Figure 2.3.7 shows the forced normal permeability distributions used in the low quality, and high quality reservoir. In this figure, the probability ranges are highlighted from which the mean and standard deviation for each forced normal distribution is taken. Porosity is calculated as described in the base case. Water saturation and λ values for cases 1 and 2 do not change from those used in the homogeneous model scenario.

With the introduction of random heterogeneity, optimal well placement (case 7) becomes contingent on injectivity along with migration distance and depth. Permeability is used as a proxy for injectivity in this study. To determine the best location for each well, permeability values are averaged over the 10 layers within each cell and re-gridded with a cell size of 1,000 x 1,000 feet (305 x 305 meters) (figure 2.4.3). The large grid size shows permeability over an area with the same order of magnitude as the early plume size. Injecting in grid cell area with high average permeability should allow for minimal pressure build up at the well and a higher injection rate. The cells that have the largest average permeability and are fully within a fetch area are selected for optimized well sites

(figure 2.4.3). The final well location is selected by choosing the model mesh cell with the highest layer-averaged permeability falling within the larger optimal cell.

The remaining cases (3, 4, 5, 6, and 8) are left unchanged from the homogeneous model. Only the porosity and permeability fields are updated to incorporate the changes made in the statistically heterogeneous base case.

Seismic-Based Heterogeneous Model Scenario

The final refinement step for capacity estimation is the population of the 3D model with seismically constrained porosity and permeability fields. Many seismic attribute-to-log property relationships are examined to develop the best methodology for permeability and porosity population with the data available. The results of these comparisons for our dataset show very weak to no correlation. These seismic property-log signature ties are likely unsuccessful for the following reasons: (1) time-depth conversion error at individual wells, (2) proximity of wells to faults (figure 2.3.3), (3) poor quality sonic curves in data wells.

In spite of potential log-seismic issues, a seismic inversion of the amplitude depth volume from 4,500 to 6,000 feet (1,372 to 1,829 meters) is generated for the DRMA using Hampson-Russell software services (CGG; version HRS-9 R1.5; Paris, France) and sonic logs from 4 wells (figure 2.3.3) (Ditkof, 2013). Density logs are not available for any well in the DRMA, so pseudo density logs are calculated using equation 16. Though the resulting inversion volume appears geologically reasonable, it does not show a strong correlation to most SP, gamma ray, or resistivity logs in the DRMA. Because the inversion volume is generated primarily with fault proximal sonic logs with no density curves, the potential error may be large.

Lacking confirmation from well log data, the seismic inversion volume is used as a hypothetical example of a seismically derived model population. The resulting inversion volume consists of the impedance, or density·velocity, in a given unit. These impedance values are sampled to the reservoir mesh by averaging the values that fall within a 3D cell. The primary factors controlling density and velocity include lithology, fluid content, and porosity. Fluid content is relatively uniform over the DRMA. Deep resistivity curves in each of the 12 available well logs suggest that the interval is saturated with brine. Porosity is most likely heterogeneous over short distances in the reservoir. However, for the DRMA, we assume that porosity changes are relatively minor. With this assumption, we propose that changes in lithology are primarily driving the changes observed in the impedance volume. To use this information in a way that allows for model population, a simple 2 facies sand-shale system is proposed. Though more than 2 facies likely exist in the reservoir, they cannot be confidently resolved in our data.

Impedance curves are generated by multiplying sonic and sonic-derived density curves together for the 4 wells in the DRMA with sonic data. Using gamma ray and/or SP to identify sandy and shaley intervals, an impedance cutoff of 18,000 g/cc·ft/s (5,486 g/cc·m/s) is determined for which values below are identified as shale and values above are identified as sand. Within the facies designated as sand, a large range in values is observed. Impedance values in the reservoir interval reach up to 40,000 g/cc·ft/s (12,192 g/cc·m/s). Values falling between the sand-shale cutoff and the maximum likely represent a mixed lithology. Well log observations show that beds of sand and shale are present at thicknesses below seismic resolution and, as a result, are sensed as a single unit by the seismic wave. From the available data, however, differentiation of the effect of porosity

from the effect of thin beds on impedance is not possible. The inverse relationship between porosity and impedance suggests that a sand unit with very high porosity should have low impedance; however the relatively low density of shale suggests that a shaley sand may also have low impedance. The relationship between lithology, porosity, and impedance creates difficulty when trying to obtain additional reservoir quality facies for impedence values between 18,000 and 40,000 g/cc·ft/s (5,486 and 12,192 g/cc·m/s). For this reason, the model is left as a simplified 2 facies model.

Porosity and permeability values must be assigned to each facies. The shale facies is automatically assigned porosity and permeability values of 0. Though in reality these shale facies will have non-zero porosity and permeability, limitations of the simulator make the modeling of zones with very low porosity and permeability difficult. Because these zones will effectively serve as impermeable baffles, assuming 0 porosity and permeability is a reasonable simplification for the purposes of simulation. The method by which permeability and porosity values are assigned to the sand facies is very similar to the methodology used to build the statistically heterogeneous model. For the seismic-based heterogeneous base case model, all cells defined as sand are populated with the P_{40}-P_{60} forced normal distribution of permeability, as described in the statistically heterogeneous base case. A new set of random numbers are generated and used as the input in the norminv Excel function. Permeability in the *i* direction is equal to the *j* direction (laterally isotropic) and multiplied by 20% in the *k* direction. Porosity is calculated from permeability with equation 19. Figure 2.4.4 shows the seismically derived and statistically populated permeability distribution for layers 1, 5, and 10. The color scale reflects the lithology, where brown is shale and yellow-gold is sand.

As in the statistically heterogeneous model, cases 1 and 2 are generated by applying the P_{80}-P_{100} and P_0-P_{20} forced normal permeability distributions to the reservoir, though the permeability field is only populated in the sand facies. Again, the spatial distribution of permeability does not change, only the intensity, or scale, of the permeability is altered. Directional permeability is defined as in all previous models, and porosity is calculated with equation 19.

Case 7 is generated using the same methodology as in the statistically heterogeneous model with the newly generated permeability distribution. Resulting averaged permeability and well locations are shown in figure 2.4.5. Note that in fetch area 1, the grid cell with the highest permeability is not selected due to its proximity to the closure. The selected site for fetch area 1 shows high permeability in addition to great depth and large potential CO_2 migration distance.

Table 2.4.1: Summary of inputs for homogeneous 3D flow model.

Summary of Homogeneous 3D Flow Model Base Case Inputs			
Parameter	**Property**	**Value**	**Source**
S_{wirr}	Irreducible Water Saturation	29%	6,206 Miocene reservoirs
Φ	Porosity	.275	6,206 Miocene reservoirs
T	Temperature	135.6° F (57.6° C)	11 log headers in DRMA
P_{init}	Initial Pressure	1,878-2,575 psi (12.9 -17.8 Mpa)	Hydrostatic gradient
Z	Depth	4,306-5,915 feet (1,312-1,803 meters)	Seismic mapping
h	Thickness	0-141 feet (0-43 meters)	Seismic mapping
κ	Permeability	183.66 mD (1.8×10^{-13} m^2)	6,206 Miocene reservoirs
A	Area	26,496 acres (107 km^2)	Seismic mapping
k	Salinity	190,000 ppm	ILD and DT (well A)
n	Corey exponent (gas)	2	Zeidouni et al., 2009
λ	Mualem exponent	.457	Zeidouni et al., 2009
D	Duration	100 years	Assumption
P_{well1}	Pressure limit in well 1	3,510 psi (24.2 Mpa)	80% of lithostatic pressure
P_{well2}	Pressure limit in well 2	3,243 psi (22.4 Mpa)	80% of lithostatic pressure
P_{well3}	Pressure limit in well 3	3,107 psi (21.4 Mpa)	80% of lithostatic pressure
P_{well4}	Pressure limit in well 4	3,131 psi (21.6 Mpa)	80% of lithostatic pressure
Bound	Boundary Conditions	Closed	Assumption
Fault	Fault transmissibility	0	Assumption

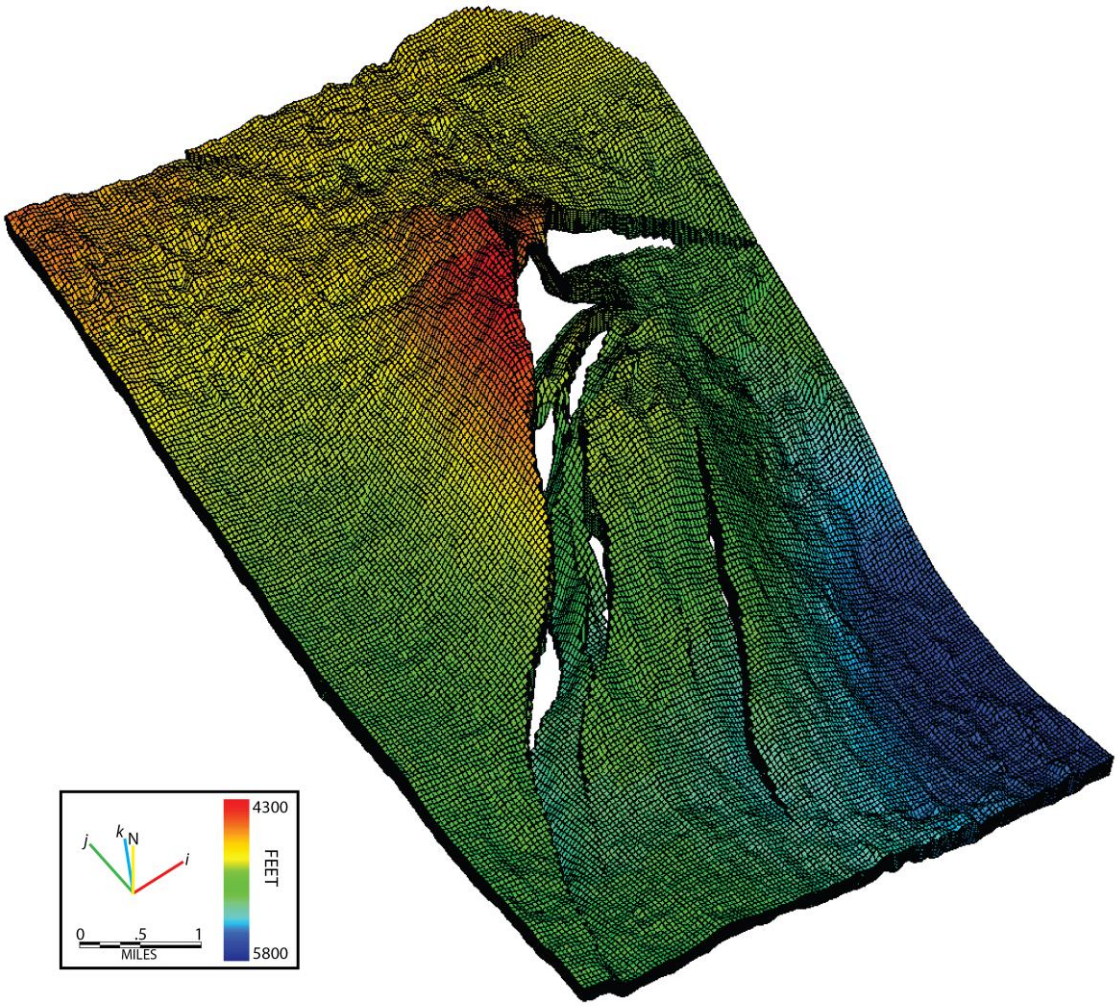

Figure 2.4.1: 3D view of reservoir model mesh colored by depth structure with grid cell outlines superimposed. See figure 2.3.1 and 2.3.3 for geographic location.

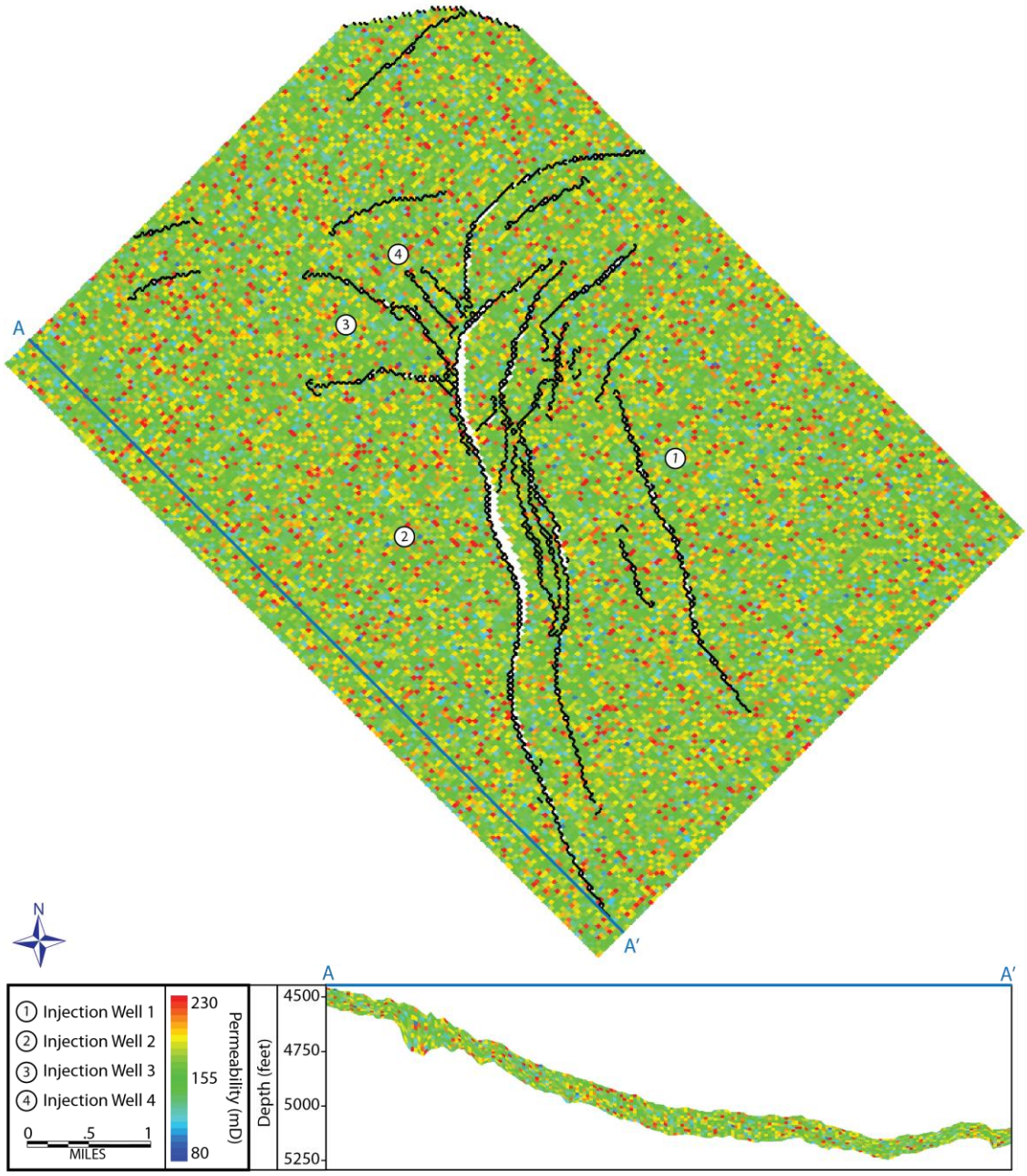

Figure 2.4.2: Top layer (layer 1) of statistically heterogeneous model base case with injection well locations. Cross section A-A' shows a sample of the vertical permeability heterogeneity.

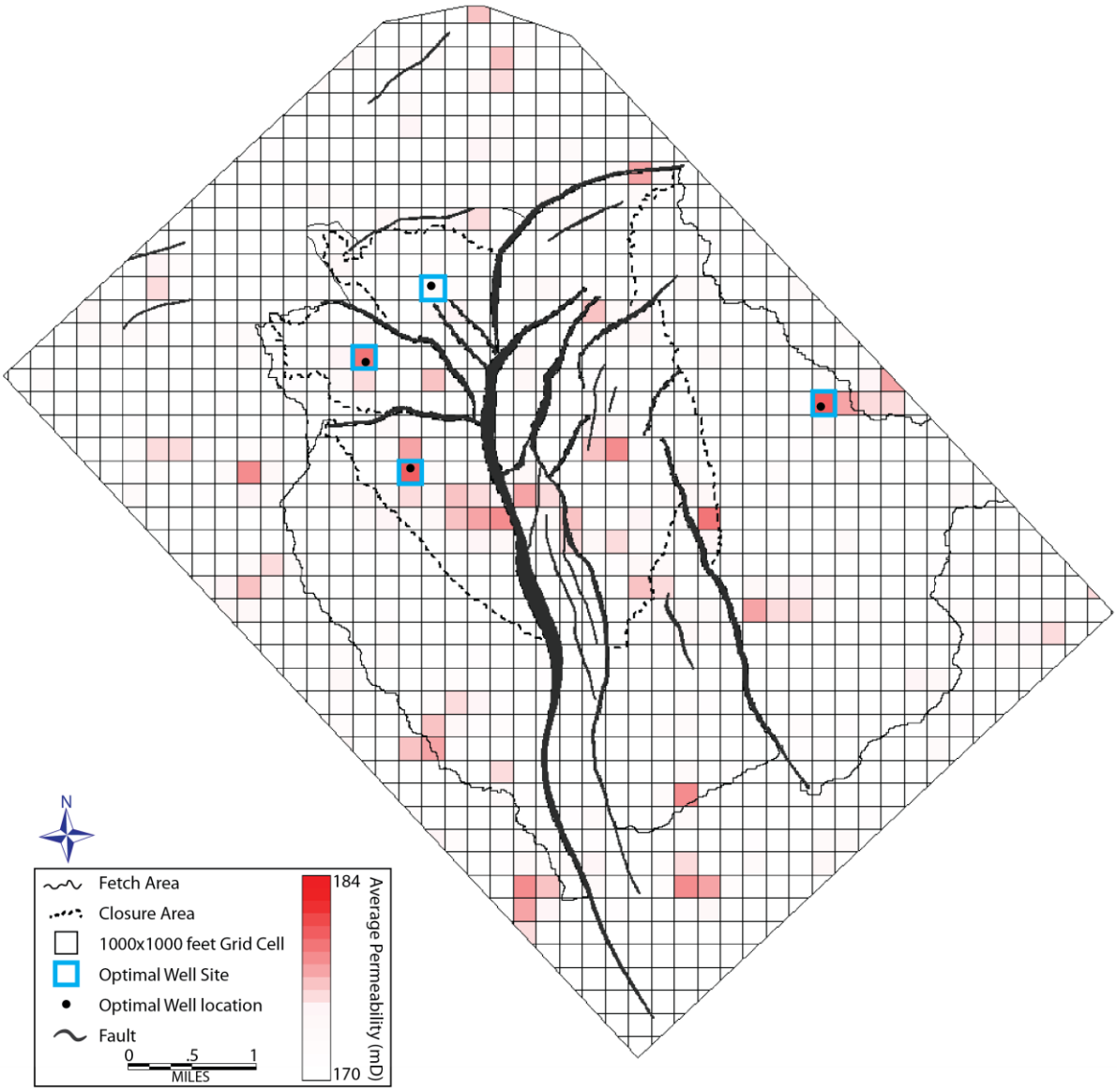

Figure 2.4.3: 10 layer average permeability of statistically heterogeneous model gridded with 1,000 x 1,000 feet (305 x 305 meter) cells. Optimal well sites are outlined in blue within which the optimal well locations are shown.

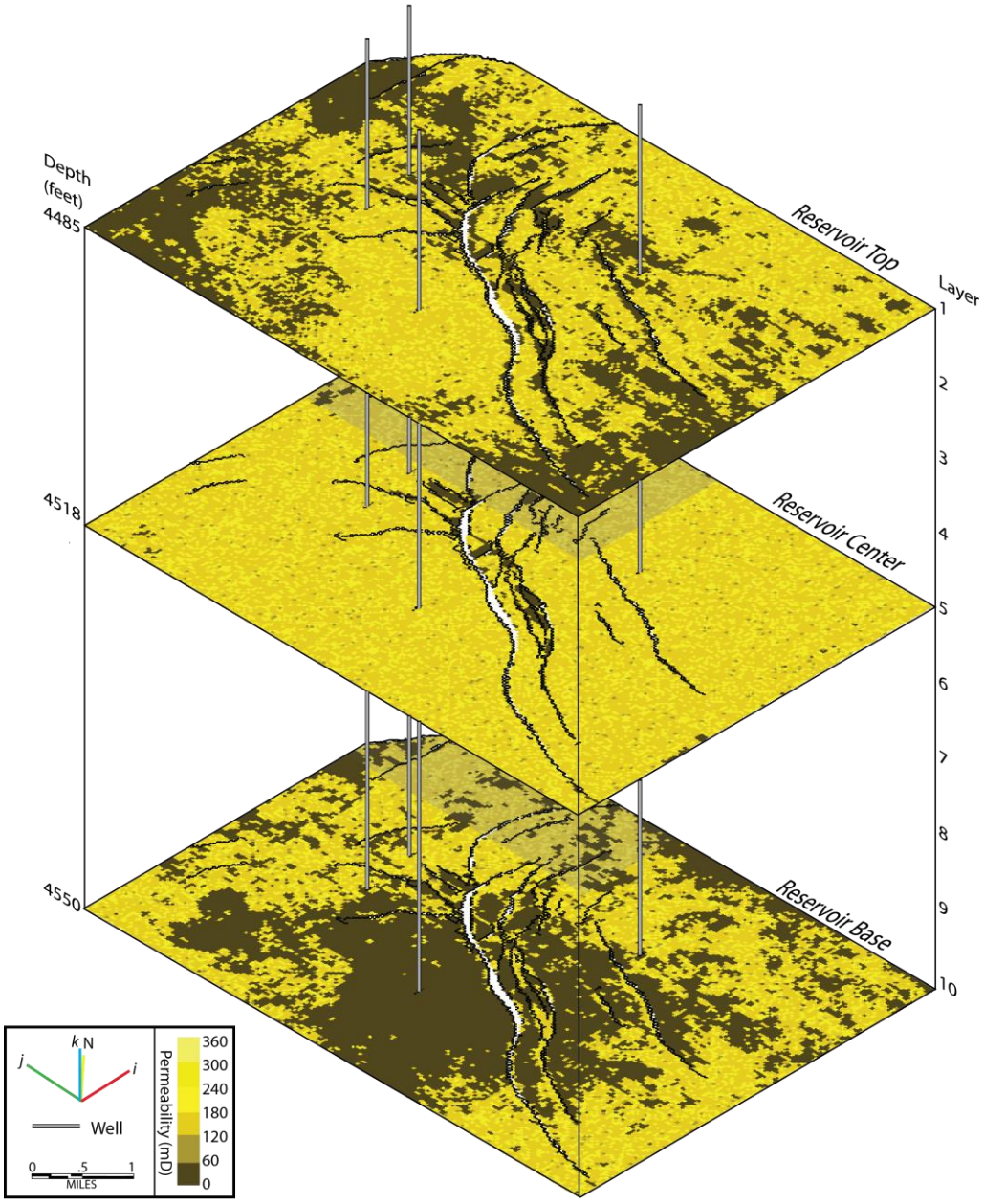

Figure 2.4.4: Layers 1, 5, and 10 colored by inversion and statistically populated permeability for the seismic-based heterogeneous bas case model. Color scale is chosen to reflect lithology (brown=shale; yellow=sand). Locations of injection wells are shown.

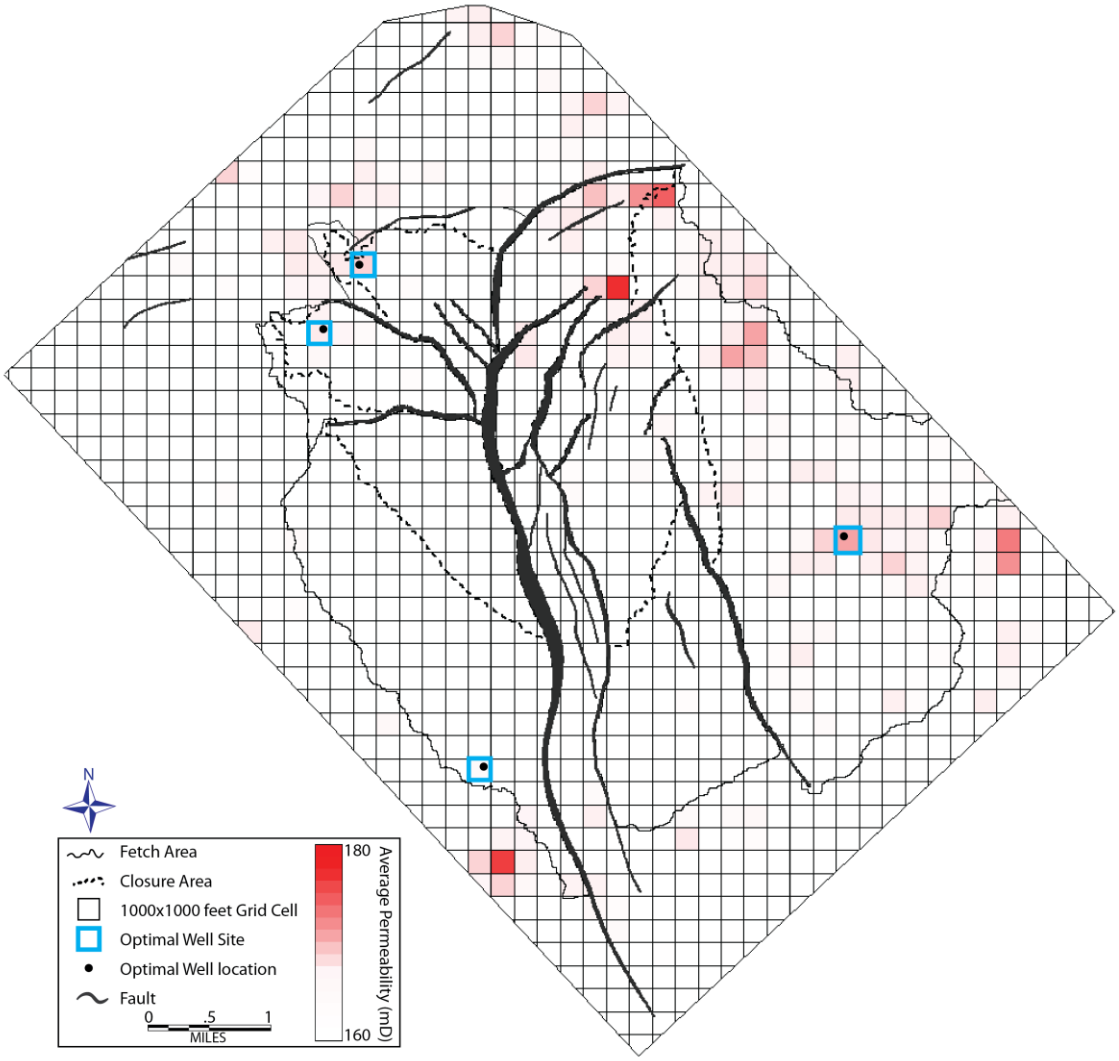

Figure 2.4.5: 10 layer average permeability of seismic-based heterogeneous model gridded with 1,000 x 1,000 feet (305 x 305 meter) cells. Optimal well sites are outlined in blue within which the optimal well locations are shown.

Chapter 3: Results

CHAPTER 3.1: REGIONAL STATIC MODEL RESULTS

The capacity map shown in figure 2.2.9 displays the potentially storable volume of CO_2 per square mile of the study area using the NETL methodology (which uses gross stratigraphic thickness). When integrated over an area of interest, a total estimated capacity can be obtained for that area. Over the entire study area, an estimated 172 Gt of CO_2 can be stored within the Miocene capacity interval of interest here. Maximum and minimum computed storage values are 27.6 and 2.4 Megatonnes (Mt)/square mile, respectively. Average and standard deviation are 10.8 and 5.2 Mt/square mile, respectively. The capacity distribution shows relatively low potential updip, and increasing storage potential in the basinward direction. The updip section of the capacity distribution shows more regular, strike parallel orientation of contour lines, whereas the downdip section shows an irregular "bulls-eye" pattern.

Refined capacity results that use net sand rather than gross stratigraphic thickness are shown in the capacity map in figure 2.2.12. Integrating the net capacity values over the project area yields a total estimated capacity of 129 Gt. Maximum, minimum, mean, and standard deviation of the calculated grid values are 21.8, 1.1, 9.5, and 4.8 Mt/square mile, respectively. Capacity values increase in the basinward direction with a general trend that is aligned with the shoreline updip and somewhat more irregular downdip.

The difference in total estimated storage between gross and net sand derived capacity is 43 Gt (25% reduction). Figures 3.1.1 and 3.1.2 show the distribution of the absolute difference and relative difference between gross and net derived capacity estimates. The absolute difference distribution is generated by subtracting the net capacity grid from the gross capacity grid and relative difference is determined by

dividing absolute difference by the net capacity estimate. Positive values (red) represent areas where the gross capacity calculation exceeds the net capacity calculation, and negative values (blue) represent areas where net capacity exceeds gross capacity. Maximum, minimum, mean, and standard deviation of the calculated difference distribution are 12.2, -10.7, 1.2, and 3.6 Mt/square mile, respectively. Spatial distribution of the difference has a trend that is roughly aligned with the coast line. Results indicate that 73% of the calculated grid values are positive (overestimated in gross calculation). Significant negative values are mainly present along the middle of the southern edge of the study area. The relative difference distribution is roughly the same as the absolute difference distribution. Updip, where capacity is lower, relative difference can become very high, almost reaching a value of one. Only very few areas show no change from the gross to net capacity calculations.

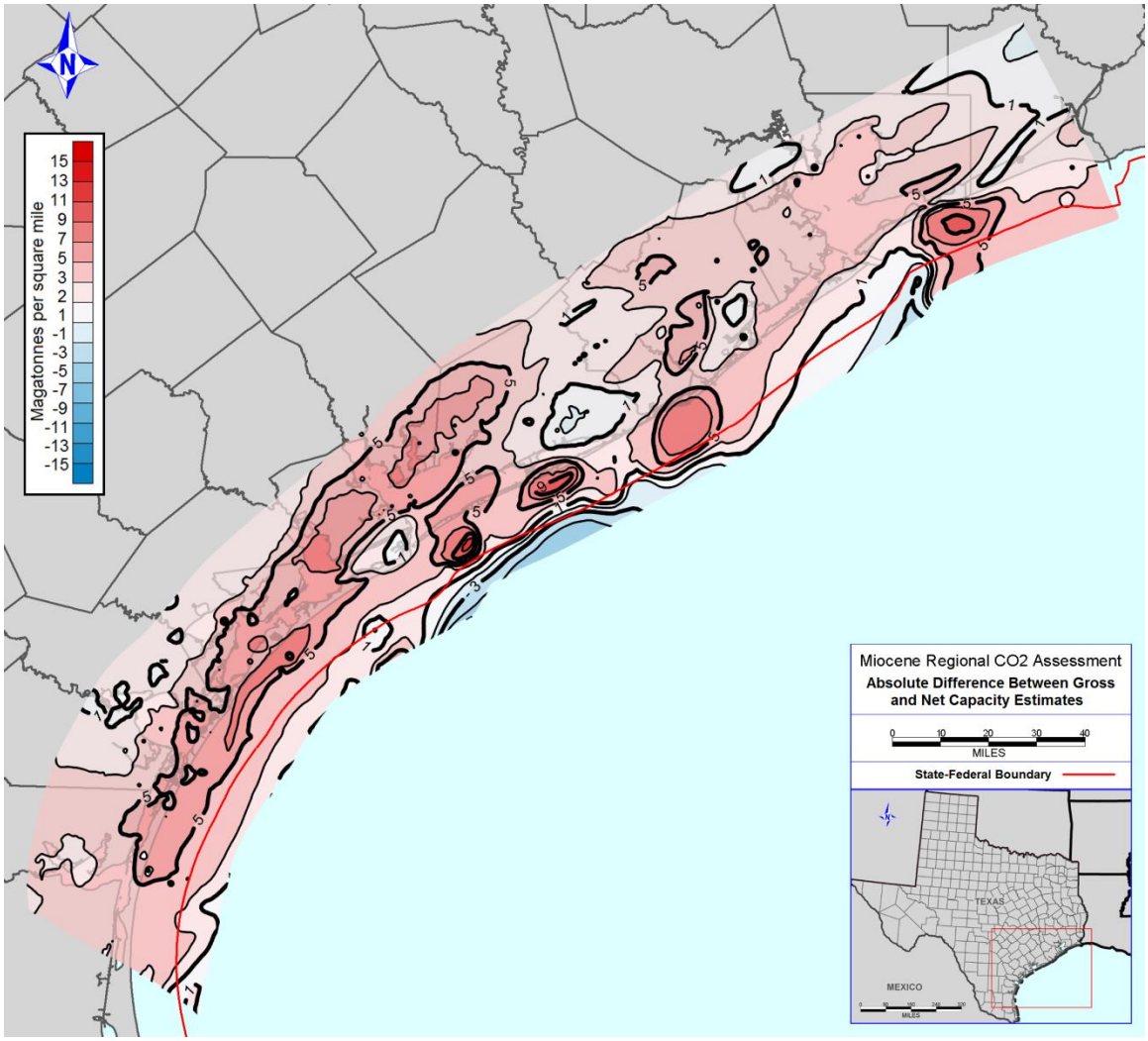

Figure 3.1.1: Distribution of the difference between gross regional capacity estimate (NETL method) and net regional capacity estimate (net sand refined).

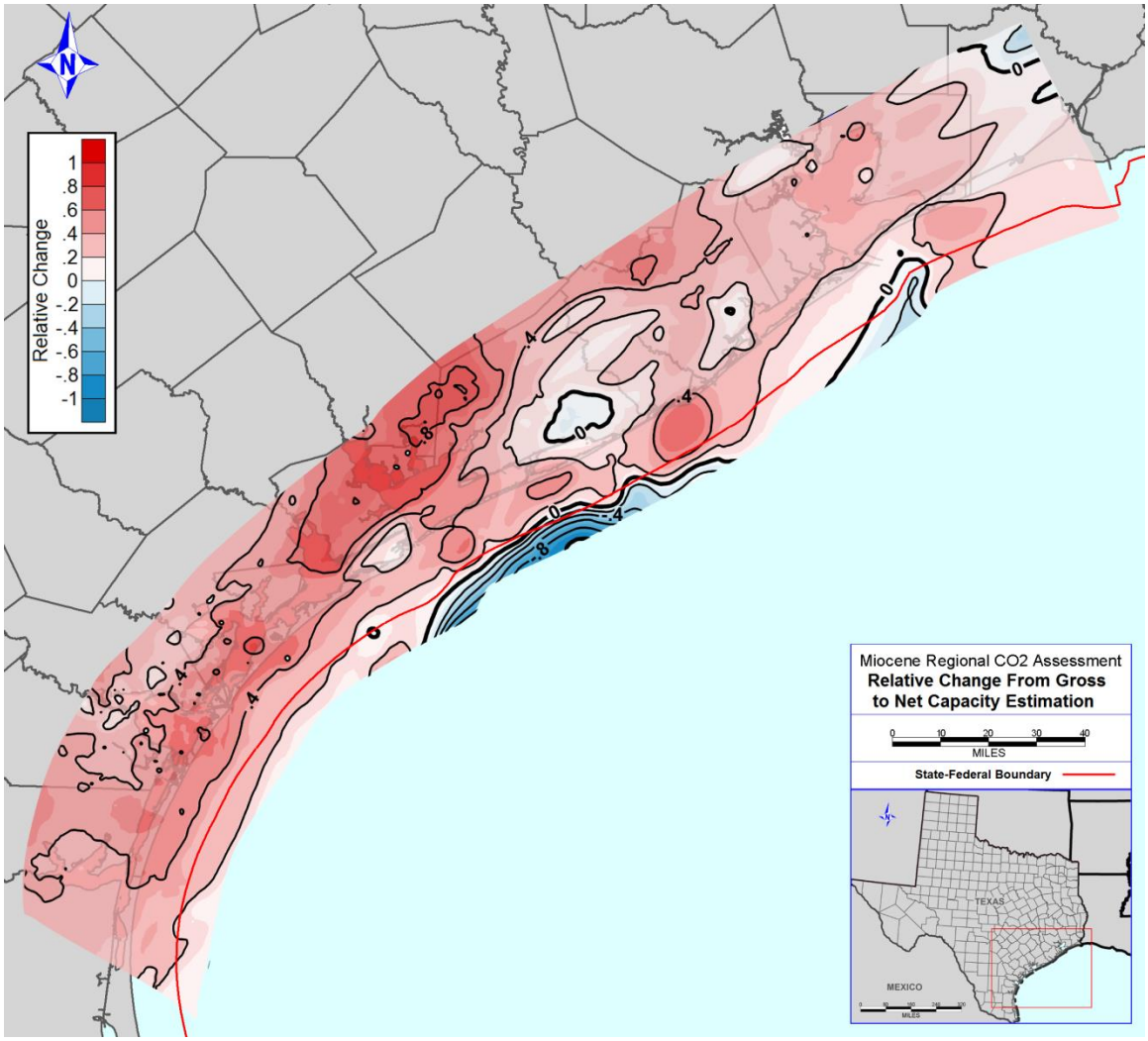

Figure 3.1.2: Relative difference between gross and net capacity estimations (unitless).

CHAPTER 3.2: SIMPLE DYNAMIC ANALYTICAL MODEL RESULTS

Results from the 6,206 model runs (1 run per sample) using a simple dynamic analytical solution to estimate capacity (see Chapter 2.3) are shown in figure 3.2.1. The distribution is colored by the data flag indicating which simulation-ending condition is met. These conditions, again, are (1) the CO_2 plume front migrates to the edge of the

reservoir, (2) the pressure limit (P_l) is reached at the edge of the reservoir, or (3) 100 years elapse. The mass of CO_2 injected varies along a mostly normal distribution from 1.6 Mt to 48.1 Mt. Mean and standard deviation are 30.3 Mt and 6.7 Mt, respectively. The P_{50} value of the resulting capacity distribution is 30.9 Mt. Only conditions 1 (plume shutoff) and 3 (time shutoff) are met with the given input data. The reservoirs flagged with maximum time shutoff constitute the greater portion of the model runs that have an injected mass less than 20 Mt.

The measured fill times fall along a positively skewed distribution with the exception of 628 samples that have fill times of 100 years, which correspond to runs that were shut off due to the time limit. Excluding the time-flagged reservoirs, the average fill time is 31.4 years (38.3 years with all samples included).

The probability distribution in figure 3.2.1c shows the difference in cumulative probability between samples with condition 1 and samples with condition 3. Comparing each curve to the total (black) shows the relative portion of the total cumulative probability from which each of the two sets of samples is comprised. From this plot and from the frequency histogram, model runs with condition 3 are observed to inject significantly less mass than model runs with condition 1.

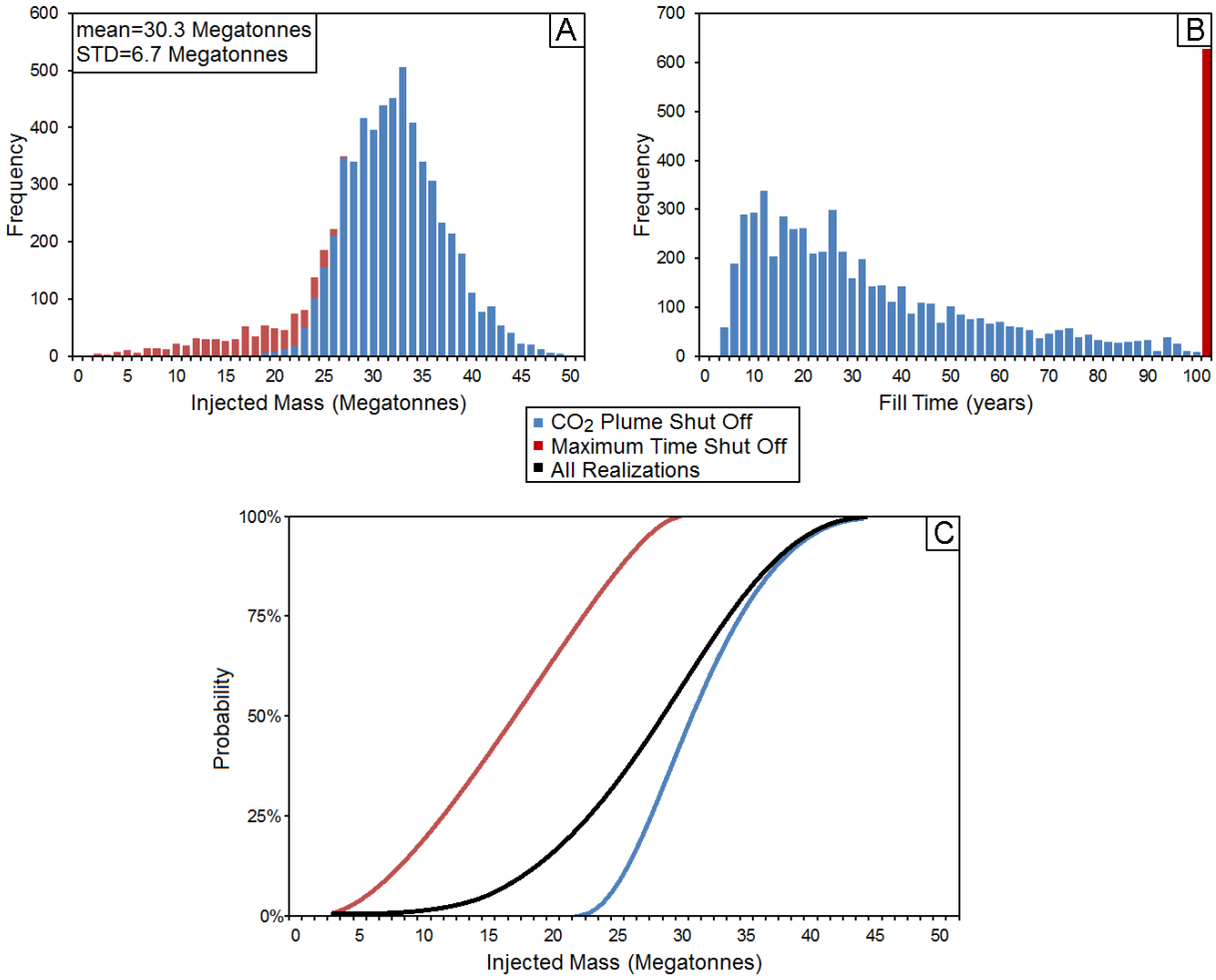

Figure 3.2.1: Simple analytical modeling results: Distribution of injected mass (a) and fill time (c) for model runs of 6,206 samples of porosity, permeability, and water saturation populated from the Miocene subset of the Atlas of Northern Gulf of Mexico Gas and Oil Reservoirs (Seni, 2006). Cumulative distribution probability plot (c) shows the probability values for both shut off flags and the probability values for all model runs combined.

CHAPTER 3.3: 3D DYNAMIC FLUID FLOW SIMULATION RESULTS

Results from fully-numeric (finite difference) 3D flow simulations show the distribution of the CO_2 plume with time for the 27 model cases previously discussed. Figure 3.3.1 shows the evolution of the CO_2 plume for the homogeneous base case. At time 0, injection has not yet begun. After the 1st year of injection (t=1) the CO_2 plumes are mostly centered on each injection well with radii of 0.3-0.5 miles (.5-.8 km). The 2nd, 3rd, and 4th years of injection (t=2, 3, and 4) show very minimal expansion of each plume and a slight oblong distortion in the updip direction. Injected CO_2 from well 1 is obstructed by a nearby fault, against which CO_2 becomes pooled. After 25 years (t=25) the plume geometry is significantly oblong, extending nearly linearly in the updip direction. CO_2 saturation within the plume changes character by showing a reduction in area of intermediate values of gas saturation (0.1-0.9) leaving plume areas either fully saturated (0.9-1) or very nearly unsaturated (<0.1). After 25 years of injection, CO_2 from well 2 shows disconnection between plume areas with full saturation. After 50 years of injection (t=50), CO_2 from wells 2 and 4 has reached the highest point of the nearest closure, whereas CO_2 from wells 1 and 3 has not. At the end of the simulation period (t=100), CO_2 from all wells has reached the top of the nearest closure. The final geometry of the CO_2 plume is shown in 3 dimensions in figure 3.3.2. Here, the structural effect on plume geometry is more clearly illustrated. Though the CO_2 plume expands relatively evenly in all directions initially, the geometry eventually becomes extended toward structural highs.

The distribution of the CO_2 plume with depth is shown in figure 3.3.3. The figure shows that most of the CO_2 is present in the upper ~10 feet (3 meters) of the reservoir (layer 1). Almost no CO_2 is present in the lower ~50 feet (15.2 meters) of the reservoir

(layers 5-10). The most substantial accumulation of CO_2 near the base of the reservoir is associated with the migration limiting fault affecting injection from well 1. CO_2 from this accumulation can be observed in all layers of the model. This characteristic is not seen in any other accumulations in the base case.

Results of different cases for the homogeneous model scenario are shown in figure 3.3.4. For each of the 8 cases, the final (t=100) plume distribution is shown along with the individual and cumulative well injection profiles through time. All well injection profiles are exponential with asymptotes at total injection values indicating that injection rate decreases with time. Cumulative injection (black curve) shows the sum of the mass injected for all wells. For the base case, it can be seen that well 1 reaches its final injected mass within the first 35 years of injection. Wells 2, 3, and 4 reach their final injected mass within 3 years of injection.

Final plume distributions for cases 1, 2, and 4 are very similar to the base case, though injection profiles differ. Case 1 shows that wells rapidly reach their maximum injected mass, which is greater than cases 2 and 4. Case 2 shows that wells 2-4 quickly reach a maximum injected mass, but injected mass from well 1 is still increasing when the simulation ends. Case 4 shows injection profiles nearly identical to the base case.

Cases 5 and 6 show the effect of variations in well number. In case 5, a large CO_2 plume is observed around the injection well and is contained in the associated closure. The injection profile shows a more steadily rising injected mass curve than the base case. Case 6 shows 15 wells with various geometries and saturations of CO_2 surrounding each well. The resulting injection profiles show that 14 wells quickly reach a very small maximum and a single well shows a more steady increase with a maximum reached after

~30 years of injection. In case 6, as in all cases, the well intersecting the reservoir at the deepest point has the greatest maximum injected mass.

Case 7 shows overall broader plume geometries and a greater areal extent of CO_2. The corresponding well injection profiles are similar to the base case, except in case 7 the curves for wells 2-4 are more closely spaced and injection from well 1 is greater. Case 8 shows narrow plume geometries with a small areal extent. The CO_2 plumes only extend in the updip direction of the injection well; they do not surround the well to the extent of most other cases. Injection profiles for case 8 are linear for the first ~90 years of injection, after which they decay exponentially.

Case 3 shows widespread distribution of CO_2. The final geometry of the CO_2 plume indicates that CO_2 has entered the volume modified edge cells, and therefore can be assumed to have left the study area. The injection profile shows steadily rising injected mass curves for each well. Wells 2-4 reach a maximum value within 60 years of injection. Well 1 shows increasing injected mass at the time the simulation is ended. Note the change in scale on the y-axis for case 3 (figure 3.3.4).

Results from the statistically heterogeneous and seismic-based heterogeneous base case models are shown in figures 3.3.5 and 3.3.6, respectively. Because porosity and permeability are not uniform and can contain zero values, a color scale is chosen to highlight impermeable zones with no porosity (white). The statistically heterogeneous base case shows a plume distribution very similar to the homogeneous base case. Though the plume is partially disrupted at the surface of the seismic-based heterogeneous model, where permeability is non-zero, the geometry is nearly identical to the statistical heterogeneous and homogeneous scenarios. Figure 2.4.4 shows that the middle of the reservoir contains a much more continuous permeability profile with fewer shale zones.

This continuous profile is observed in the plume geometry with depth, as the saturation becomes more even and matches the homogeneous base case. The total injected mass decreases from the homogeneous to statistical heterogeneous to seismic-based heterogeneous base case models, but the trend of the injection curves is nearly identical. Plume geometries and injection profiles for the 8 cases of the heterogeneous scenario are very similar to the homogeneous scenario. The primary difference between the results from the three scenarios is the maximum injected values in the well profiles.

Table 3.3.1 and figure 3.3.7 show the resulting total injected mass for each of the 27 cases. The homogeneous scenario cases range from 3.7-116.2 Mt of injected mass, the statistically heterogeneous scenario cases range from 3.5-114.4 Mt, and the seismic-based heterogeneous scenario cases range from 3.1-64.0 Mt. The statistically heterogeneous scenario results are less than or equal to the homogeneous scenario results for every case except the constant injection rate case. Seismic-based heterogeneous scenario results are less than homogeneous scenario results and less than statistically heterogeneous scenario results for every case. With the exception of open boundary cases, all cumulative injection results fall between 3.1 and 6.9 Mt with an average and standard deviation of 5.1 and .9 Mt, respectively. The low reservoir quality case shows the lowest injected mass and the open boundary case shows the greatest injected mass for each of the three model scenarios. High reservoir quality cases consistently yield the second largest injection results.

Reservoir fill time varies between homogeneous, statistically heterogeneous, and seismic-based heterogeneous scenarios. Figure 3.3.8 shows the cumulative injection profile for the base cases of each of the 3 scenarios. The dotted vertical line indicates at which point no additional CO_2 is injected, which is equivalent to the fill time. For the

homogeneous, statistical heterogeneous and seismic-based heterogeneous base cases, fill times are 45, 63, and 57 years, respectively.

Table 3.3.1: Cumulative injection results for 27 model cases of the dynamic 3D flow model.

3D Flow Model Injected Mass Results (Mt)			
	Homogeneous	**Statistically Heterogeneous**	**Seismic-Based Heterogeneous**
Base Case	5.4	5.3	4.5
High Quality Reservoir	6.9	6.8	5.7
Low Quality Reservoir	***3.7***	***3.5***	***3.1***
Open Boundaries	***116.2***	***114.4***	***64.0***
Open Faults	5.6	5.3	4.6
1 Well	6.0	5.7	5.0
15 Wells	5.4	5.2	4.8
Optimized Array	5.4	5.3	4.9
Constant Rate Injection	4.8	5.1	4.5

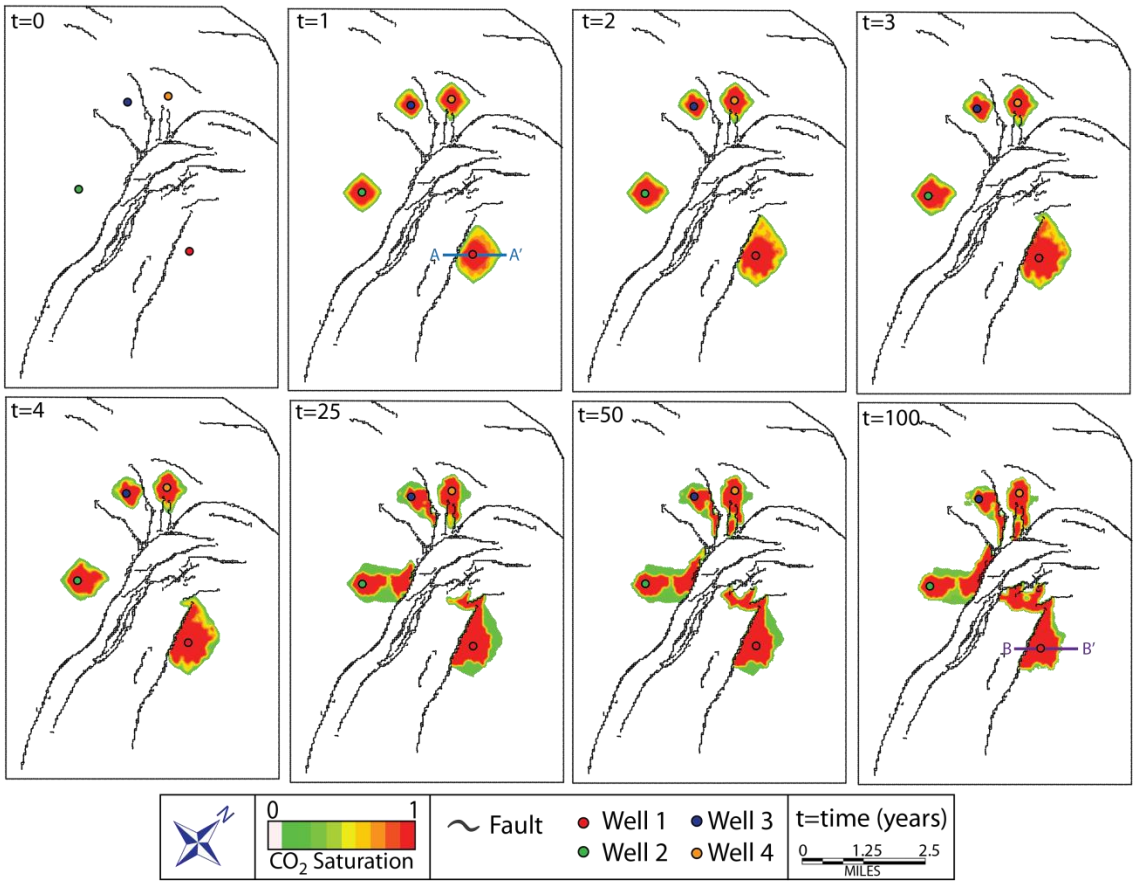

Figure 3.3.1: CO_2 plume geometry with time for homogeneous base case 3D model. t=0 indicates time before injection and each subsequent time shows the plume geometry t=n years after injection. Cross section A-A' and B-B' are discussed in chapter 4.3 and shown in figure 4.3.1.

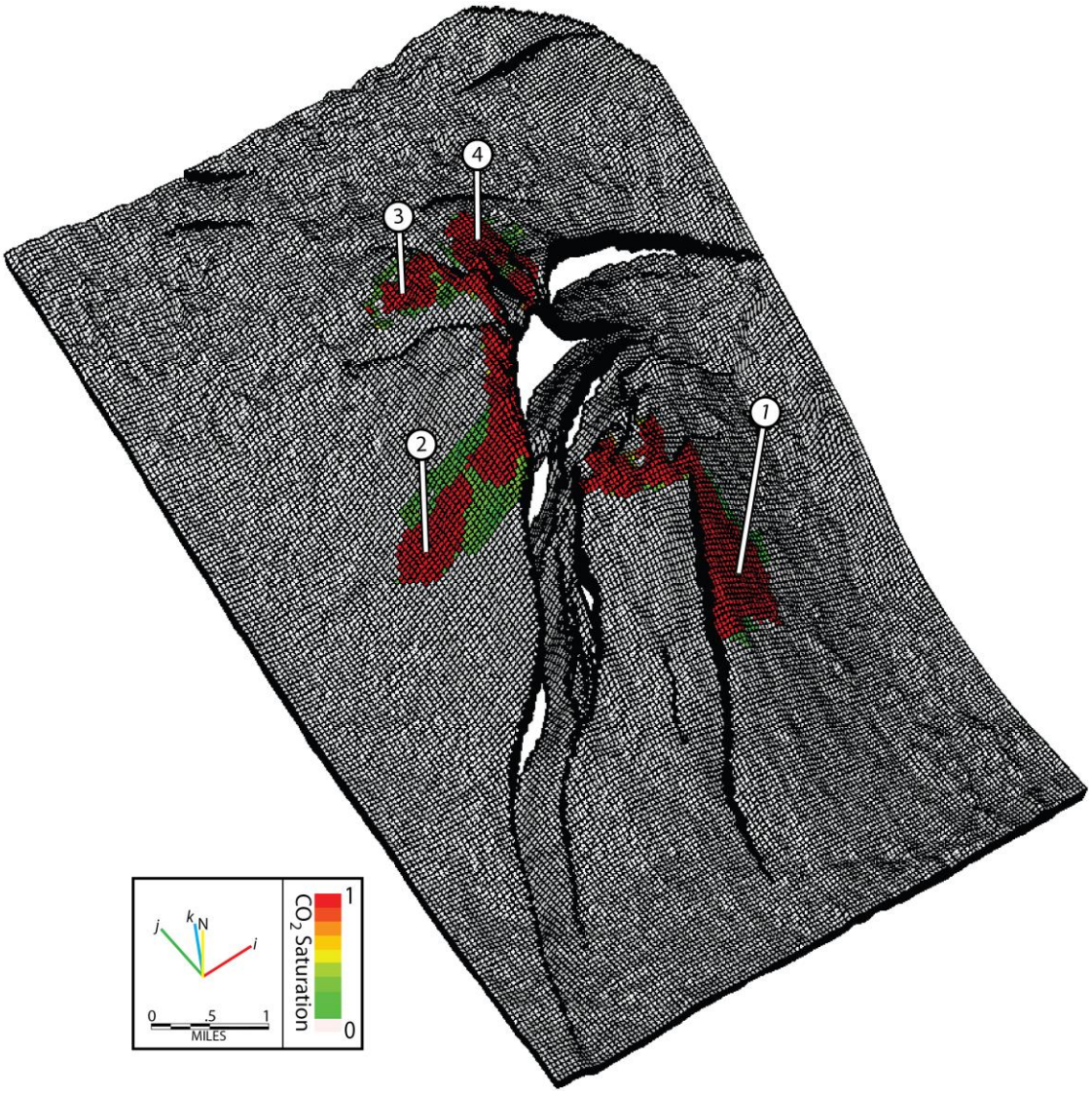

Figure 3.3.2: 3D view of homogeneous base case reservoir model at the end of simulation (100 years). CO_2 plume distribution is shown as saturation fraction for the top of the reservoir.

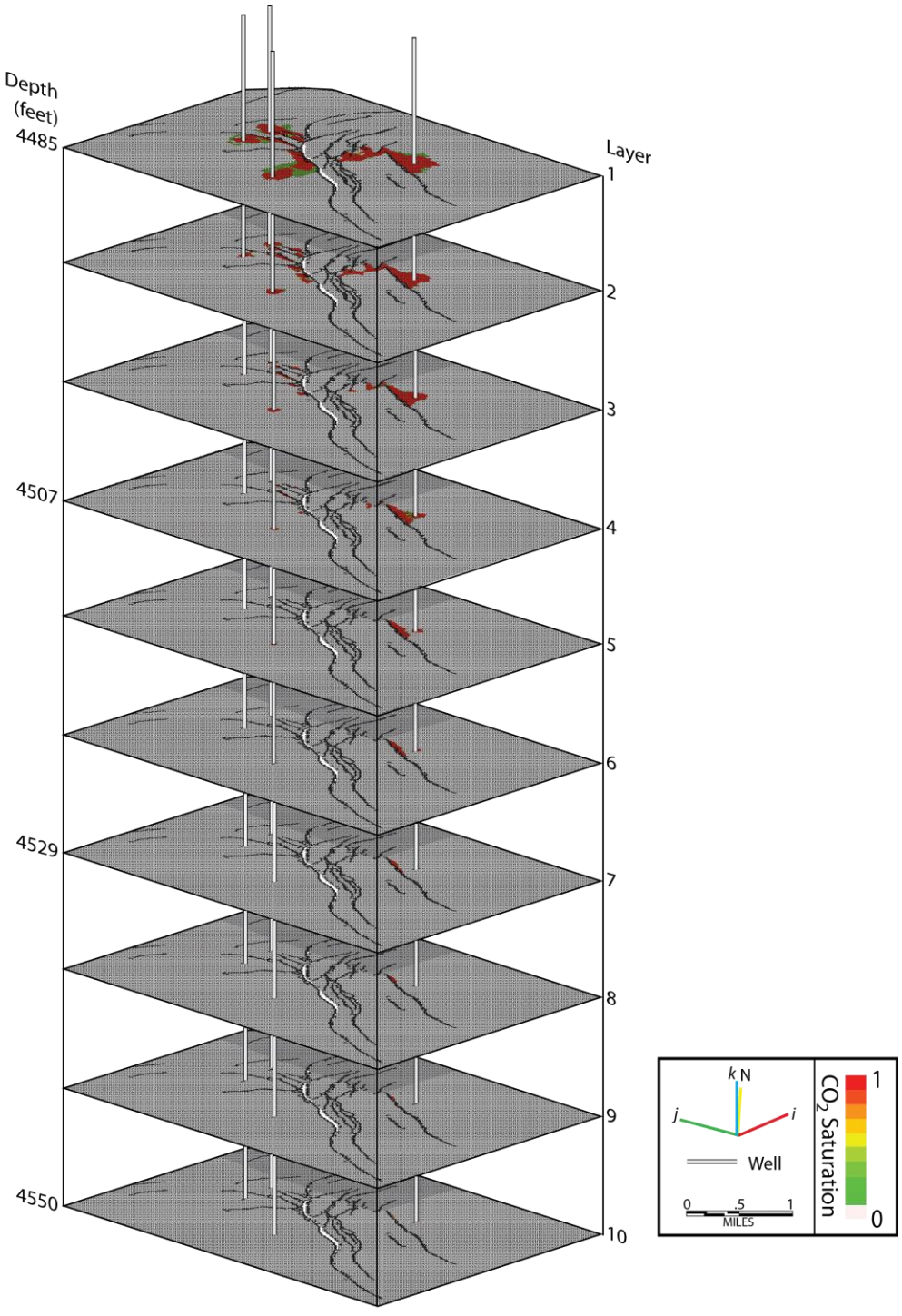

Figure 3.3.3: Tops of reservoir layers 1-10 showing CO_2 plume distribution for homogeneous base case.

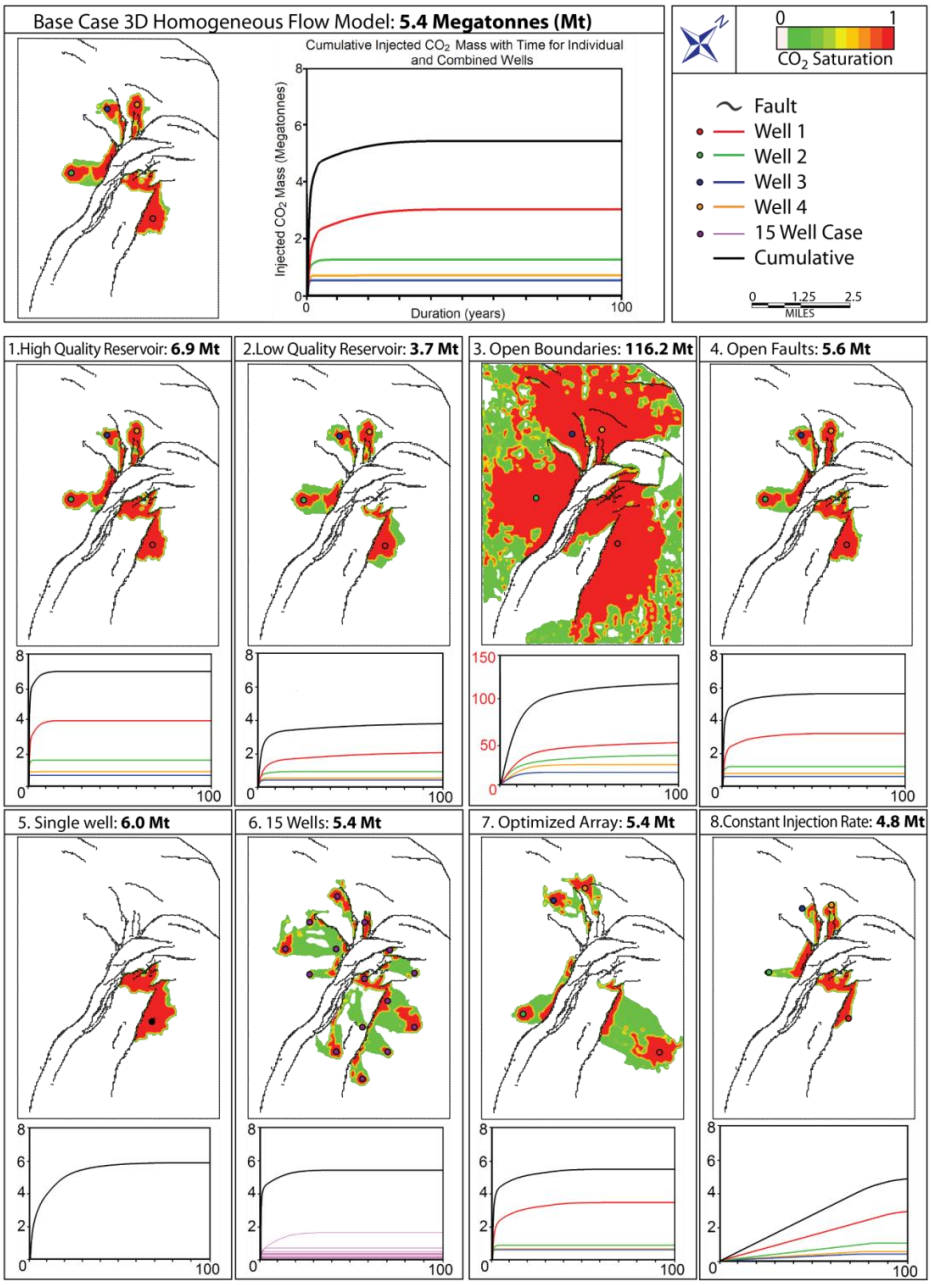

Figure 3.3.4: Final plume geometries at the top of the reservoir and injection profiles for cases 1-8 for homogeneous model scenario. Y-axis of all plots is injected CO_2 mass (Mt) and x-axis is duration (years). Note the change in y-axis scale on case 3.

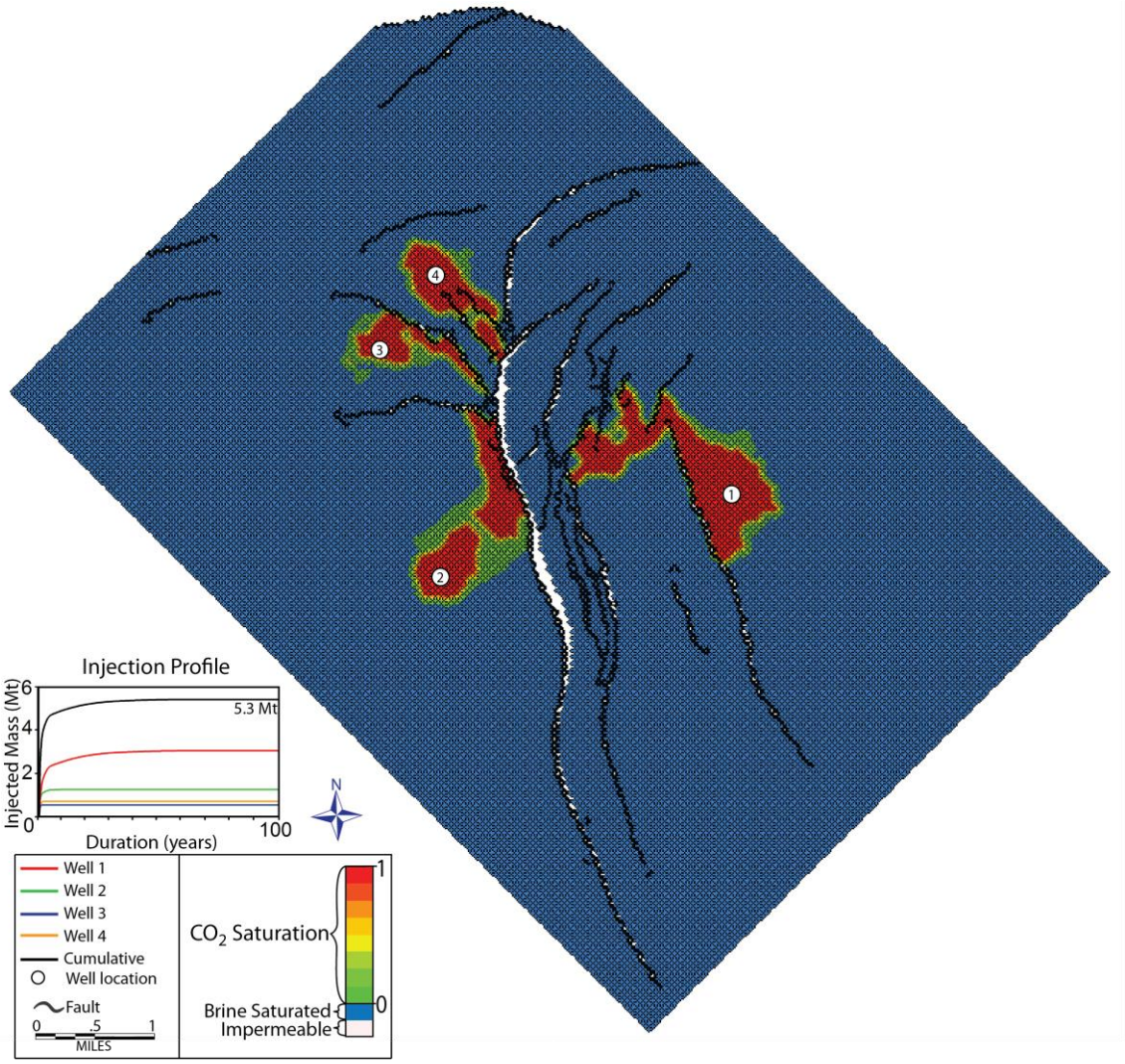

Figure 3.3.5: Final plume geometry at the top of the reservoir and injection profile for statistical heterogeneous scenario. Color scale is chosen to identify any impermeable zones, though not present in this case. CO_2 plume is indicated by the color spectrum from green to red.

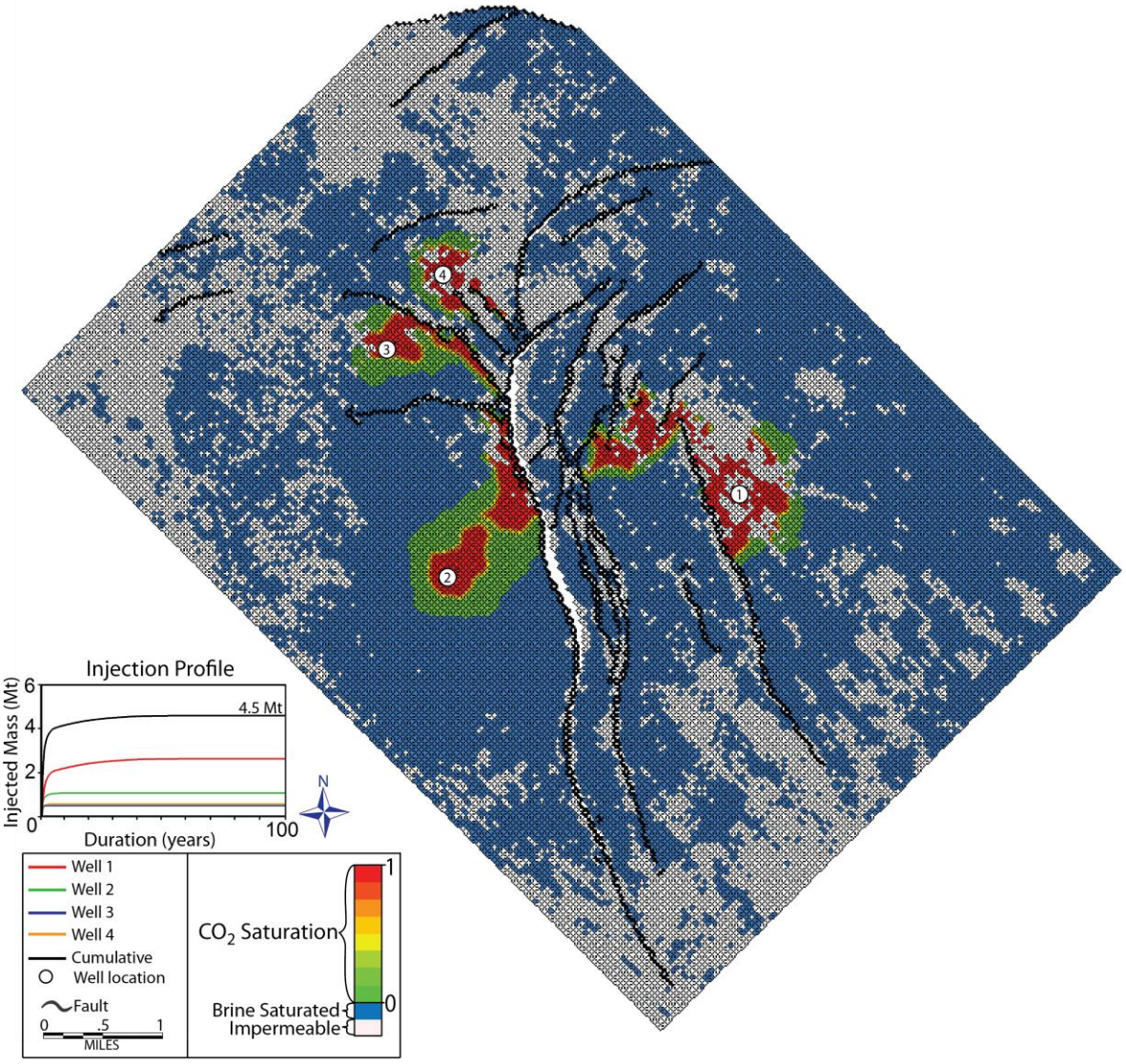

Figure 3.3.6: Final plume geometry at the top of the reservoir and injection profile for seismic-based heterogeneous scenario. Color scale is chosen to identify any impermeable zones, shown in white. CO_2 plume is indicated by the color spectrum from green to red.

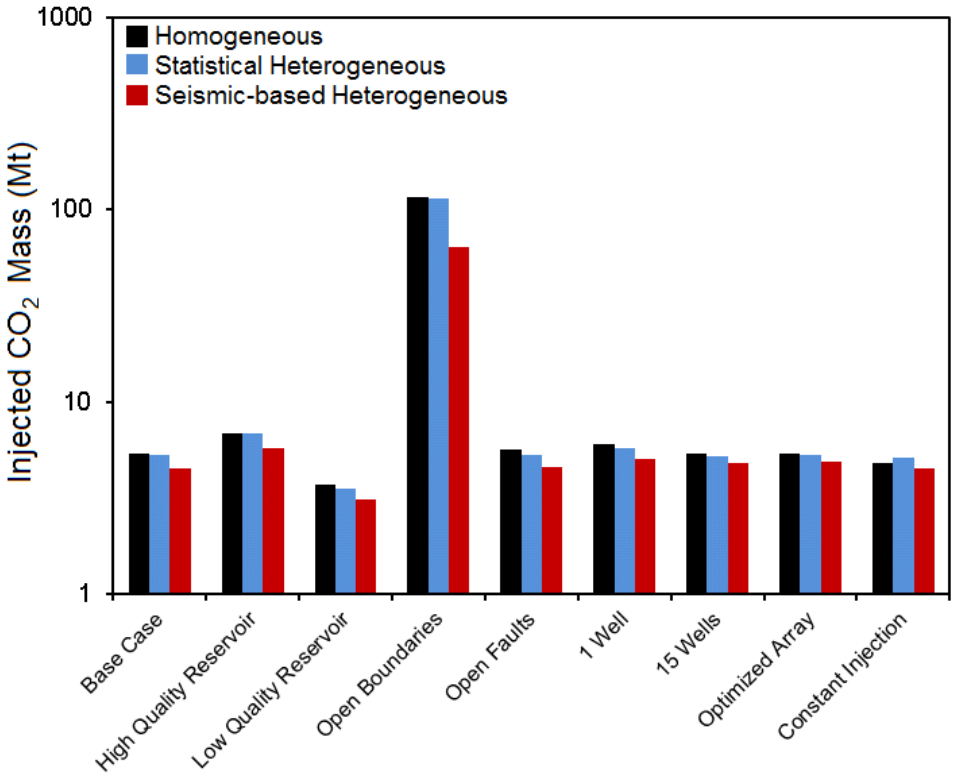

Figure 3.3.7: Bar graph of injected CO_2 mass (Mt) for each case of homogeneous, statistical heterogeneous and seismic-based heterogeneous models. Note that the y-axis uses a logarithmic scale.

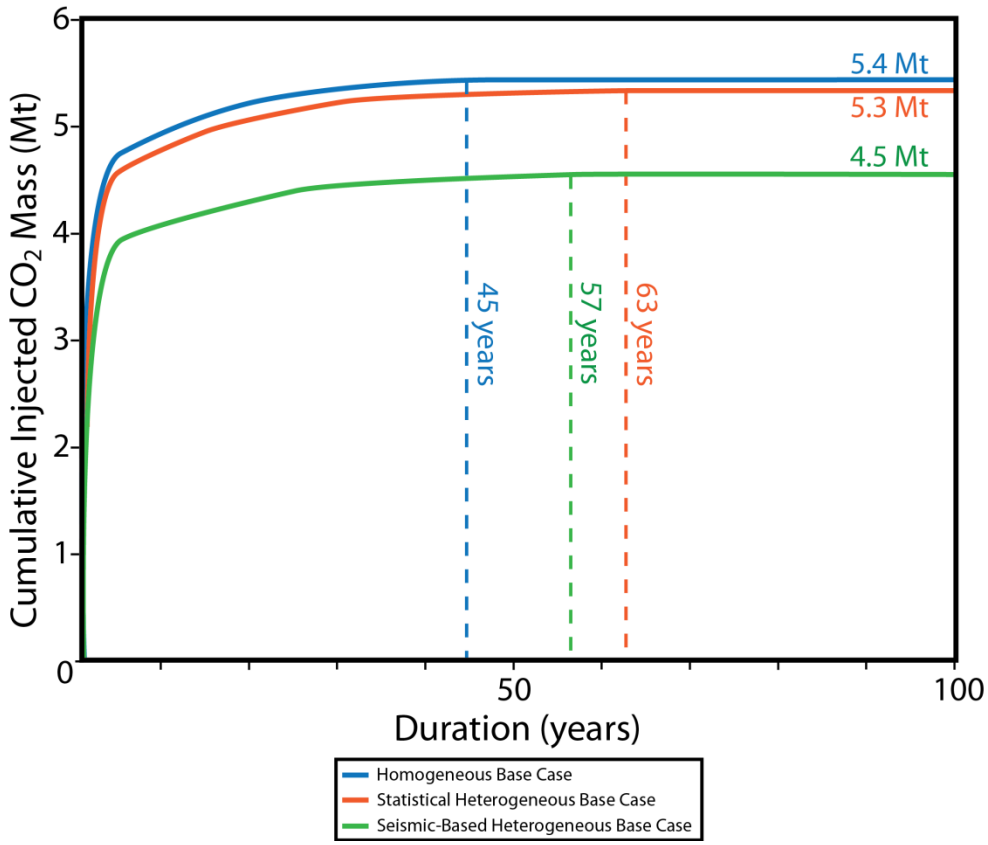

Figure 3.3.8: Cumulative injection vs. time of homogeneous, statistical heterogeneous, and seismic-based heterogeneous base case models. Dotted vertical line indicated time after which no additional CO_2 is injected.

Chapter 4: Interpretation

CHAPTER 4.1: INTERPRETATION OF REGIONAL STATIC MODEL

Only φ_{tot}, ρ, and h_g vary in equation 1 and can influence the distribution of storage capacity. In the regional capacity input grids, φ_{tot} varies from 22-38%, ρ from 0.5-0.7 g/cc, and h_g from 0-7,000 feet (0-2,134 meters). The spatial distribution of h_g is very similar to the distribution of ρ. This is due to the use of a depth midpoint in the calculation of CO_2 density. Because the top of the capacity interval is generally constant at a value of 3,300 feet (1,006 meters), the input midpoint depth is determined primarily by the depth of the base of the capacity interval. Thus, where the base of the capacity interval is deeper, the interval thickness is greater and CO_2 density will be higher. The positive relationship between ρ and h_g paired with the large range of h_g over the study area result primarily in a thickness-controlled capacity distribution. This can be observed in the overall similarity in the distribution seen the capacity interval isopach and gross storage capacity maps (figures 2.2.6 and 2.2.9) as well as the capacity interval net sand and net storage capacity maps (figures 2.2.11 and 2.2.12). The basinward increase in storage capacity is a reflection of the seaward expansion of the capacity interval (figure 2.2.1).

In the updip section of the study area, the base of the Miocene defines the base of the capacity interval as it is shallower than the top of overpressure. Thus, updip isopach and storage capacity distributions show a regular, strike-parallel orientation reflecting the relatively uniform, seaward dipping base of the Miocene. In downdip areas, the base of the capacity interval is defined by the top of overpressure, as the latter becomes shallower than the base of the Miocene. The resulting bulls-eye pattern in the capacity distribution is a reflection of the irregular nature of the top of overpressure.

Estimated capacity decreases from gross to net calculations. This is not because h_g decreases from gross to net, but rather that h_g decreases more than E (storage efficiency factor) increases from gross to net calculations (see equation 1). Dividing the net sand map by the capacity interval isopach map yields an average net-to-gross ratio of 0.28, and by dividing equation 9 by equation 10, the P_{50} net-to-gross ratio used by the NETL is found to be 0.44. This suggests that the net-to-gross ratio estimated by the NETL is larger than the actual net-to-gross ratio in the offshore Texas Miocene interval by approximately 60%. The distribution of the net-to-gross ratio in the capacity interval is not uniform. Thus, correcting the gross efficiency factor so that gross results match net results depends on the area over which the calculation is integrated. For example, over the entire study area, gross E would need to be 0.015 rather than 0.02 to generate matching gross and net capacity estimates. This change, however, would not be the same over a different areal extent.

The relative difference between the gross and net capacity estimates (figure 3.1.2) shows spatial variations caused by the irregular distribution of the net-to-gross ratio of the capacity interval. Where the relative change is high, the net-to-gross ratio is much lower than the assumed 0.44, and gross capacity is overestimated when compared to net capacity. Where relative change is most negative, the actual net-to-gross ratio is much higher than the assumed value. For example, the area of dark blue in figure 3.1.2 contains relatively large sand thicknesses (figure 2.2.11) paired with relatively low isopach thicknesses (figure 2.2.6) resulting in an above average net-to-gross ratio. Because the net-to-gross ratio is anomalously high in this area, gross capacity is underestimated when compared to net capacity.

CHAPTER 4.2: INTERPRETATION OF SIMPLE DYNAMIC ANALYTICAL MODEL RUNS

The resulting distributions of the model runs of 6,206 samples of Miocene-specific gas reservoir geology (figure 3.2.1) suggest the dependency of injected mass and fill time on φ, κ, and S_w. Recall that fill times are rarely considered for more than a few simulations of interest (i.e. a specific reservoir model), so the large number of analytical results here are important for anticipating the variability of fill times that a wide spectrum of reservoirs might be associated with and the geologic controls that influence those fill times. To better determine the nature of the relationship between these variables, cross plots between φ, κ, and S_w and injected mass and fill time are generated (figure 4.2.1). Points shaded in blue represent model runs that shut off because condition 1 (plume shutoff) is met and those in red shut off because condition 3 (time shutoff) is met. The exponential decay trend shown in the plot of injected mass vs. fill time suggests that quick filling reservoirs typically have a larger capacity. All points with condition 3 are near or below the expected values of the exponential trend.

The primary reservoirs of interest for CCS are those that can be quickly filled with large amounts of CO_2. To better observe the factors that contribute to this kind of reservoir performance, all reservoirs that are filled with greater than 30 Mt in less than 20 years are highlighted in yellow. These cutoffs are arbitrarily chosen to represent the high-end of reservoir performance.

The factors most closely tied to fill time and injected mass will be those with the least amount of scatter in the cross plots. Permeability has a very strong, exponential relationship to fill time. Because permeability primarily affects fluid flow rates, this relationship is expected. The relationship indicates that a permeability greater than 1,000 mD (9.9×10^{-13} m^2) will result in a fill time of less than 10 years and correspond to

simulation-ending criteria of condition 1 (plume shutoff). The relationship also indicates a very large range in potential fill times for samples below 100 mD (9.9×10^{-14} m^2). Porosity and water saturation vs. fill time do not show exceptionally strong correlations to fill time, though a weak negative trend is present between porosity and fill time and a weak positive relationship between water saturation and fill time.

The cross plots between injected mass and φ, κ, and S_w, show fairly strong correlations with clearly observable trends. Because the injected mass is highly dependent on the available pore volume, we expect that porosity and water saturation are primary influences. A positive relationship exists between porosity and injected mass and a negative relationship exists between water saturation and injected mass, as expected. The strong exponentially increasing relationship present between permeability and injected mass is most likely explained through the relationship observed between φ, κ, and S_w in the atlas dataset (figure 2.3.7). That is, reservoirs with high permeability tend to have high porosity and low water saturation and thus are able to store larger amounts of CO_2. The relatively low scatter in the permeability vs. injected mass plot can also be partially explained by a condensing effect in the scatter plot at low permeabilities due to the logarithmic nature of permeability in the dataset. Bacause permeability is logarithmically distributed, it is plotted with a large range on the y-axis. The large scale essentially condenses the scatter of points in the lower range of permeability values. Though porosity and water saturation are influences on injected mass, a relatively high amount of scatter still exists in the resulting cross plots. The imperfect correlation between porosity and water saturation observed in the Miocene gas reservoir atlas data allows for the possibility of reservoirs with low porosity to also have a low water saturation and high porosity reservoirs to have high water saturation, which counters our

expectations. In these reservoirs, the available volume for CO_2 storage is not accurately described by only porosity or water saturation. To better observe the relationship between pore space and injected mass, a cross plot between available pore space $[(1 - S_w)\Phi]$ and injected mass is generated (figure 4.2.2) and shows a strong positive correlation. Deviation from the trend is observed only in reservoirs where CO_2 injection terminated as a result of condition 3. This can be explained by under-filling of reservoirs due to time constraint. Given enough time these reservoirs would most likely fall along the trend.

These results indicate that of φ, κ, and S_w, κ has the largest influence on the time needed to fill the reservoir and that available pore space is the dominant factor influencing the amount of CO_2 that can be stored. Any relationship between porosity, water saturation, and fill time is likely a result of the observed relationship between φ, κ, and S_w. Likewise any relationship between permeability and injected mass is likely due to the relationship between permeability, porosity, and water saturation. The high performance reservoirs (yellow) indicate that large available pore space and high permeability are necessary for large injection in a short amount of time. Of these two factors, the available pore space will likely limit the feasibility of a project. The permeability vs. fill time plot clearly shows that, even with relatively low permeability (100-500 mD [9.9×10^{-14}-4.9×10^{-13} m^2]), a quick fill time (< 20 years typically) can be achieved. When considering already rapid fill times, increasing permeability will only significantly reduce fill time to a point. That is, 1 Darcy (9.9×10^{-13} m^2) magnitude flow is not necessary to fill a reservoir in a feasible time scale; with 100-500 mD (9.9×10^{-14}-4.9×10^{-13} m^2) material, a project can be equally feasible. Thus, available pore space will ultimately set very high quality reservoirs apart from average reservoirs. This finding is emphasized by the slope of the trend in figure 4.2.2. Here, a 50% change in available

pore space corresponds roughly to a 45% change in injected mass. This is very near to the direct relationship that is assumed in the NETL method (equation 1).

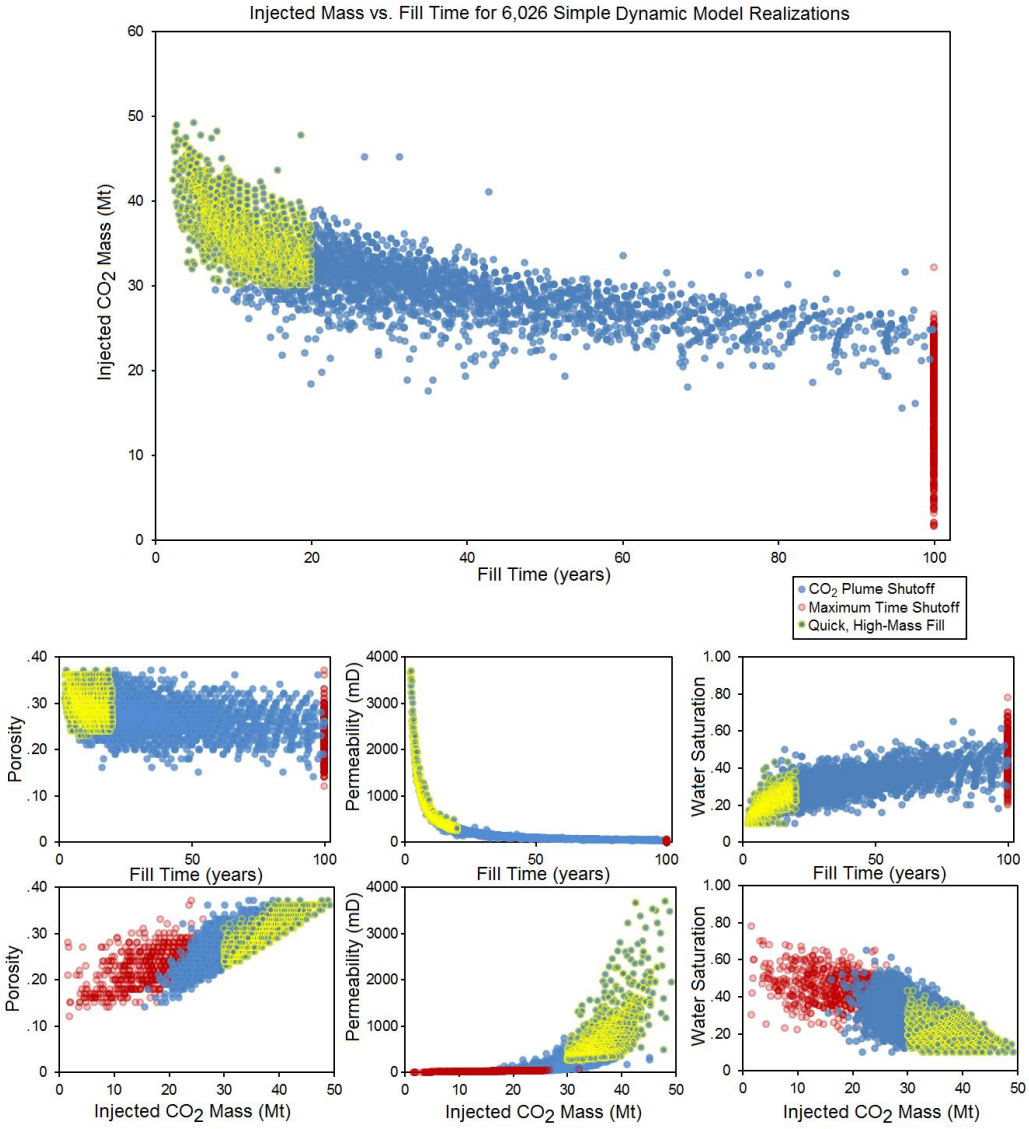

Figure 4.2.1: Cross plots of porosity, permeability, water saturation, injected CO_2 mass, and fill time for model runs of 6,206 samples using the simple dynamic analytical model. Red shaded points represent reservoirs that shutoff due to condition 3 (time shutoff) and blue shaded points represent reservoirs that shutoff due to condition 1 (plume shutoff). Yellow highlighted points represent high performance reservoirs that fill quickly with large amounts of CO_2.

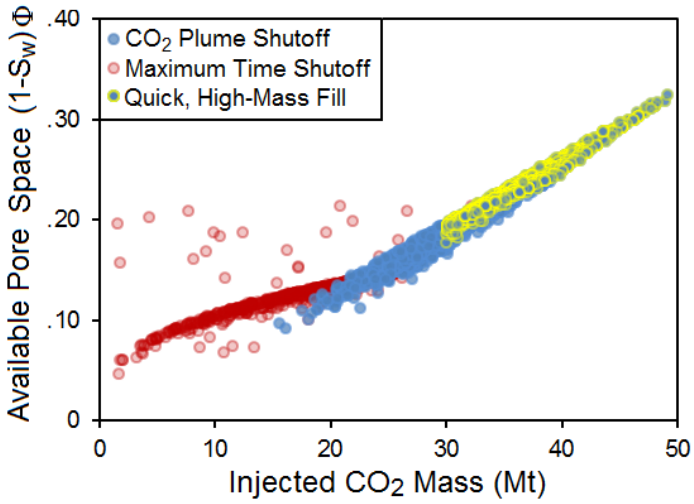

Figure 4.2.2: Available pore space vs. injected CO_2 mass. Available pore space is defined as $(1 - S_w)\Phi$.

CHAPTER 4.3: INTERPRETATION OF 3D DYNAMIC FLUID FLOW SIMULATIONS

The CO_2 plume distribution with time in the homogeneous base case model result shows a quick radial expansion, after which plume growth is relatively minimal and geometry change is limited to updip extension (figure 3.3.1). This is due to the constant pressure injection condition used in the model. Because no limit is given for the maximum injection rate, when injection starts the rate is theoretically infinite. Though in the following instant the pressure perturbance is felt (constrained by boundary conditions) and the injection rate rapidly declines, the rate is still extremely high in the early times of injection (t<1). This is reflected in the very rapid plume development seen from t=0 to t=1. After 1 year the pressure has already been significantly elevated, causing a large reduction in the injection rates that limits plume expansion.

The effect of gravity does not seem to play an important role in the areal distribution of CO_2 when the injection rate is very high (>.001 Mt/day). The large initial velocity of CO_2 flowing through the reservoir likely overrides the effect of the dipping

beds (~7° over majority of injection area) in the reservoir. This result is observable in the nearly radially symmetric plume geometry at t=1. Decreasing injection rate and increasing plume size serve to slow the velocity of the CO_2 plume front after 2 years, and subtle buoyancy effects become observable as the plume begins extending in the updip direction. The velocity override from gravitational effects can also be observed in the shrinking of downdip saturated areas with time. From t=4 to t=25, a loss in the amount of intermediately saturated zones is observed, as is a downdip shrinkage of the plume. This is due to the variation in injection rate and the increase in simulation time. With high initial injection rates (>.001 Mt/day), radial plume development forces CO_2 downdip. The CO_2 front at high velocity is more disperse, shown by the intermediately saturated zones (yellow) at t=1-4 in figure 3.3.1. When the injection rate is low (0-.001 Mt/day) and 25 years have passed, CO_2 that initially migrated downdip changes flow direction and begins to move updip. This slow moving CO_2 has a condensed front and lacks intermediate saturation. In these downdip areas where CO_2 has initially invaded and subsequently left, CO_2 with a residual saturation of <0.1 appears to migrate back toward the edge of the fully saturated plume with time.

After 25 years, CO_2 becomes relatively stationary and updip migration becomes minimal. One expectation might be that, after 100 years, CO_2 will have migrated to the uppermost portion of the reservoir and fill the closure to a uniform depth. The simulation results suggest this is not the case; rather, given infinite time, the CO_2 might only migrate slightly further updip than after 100 years. Without the injection of more CO_2 to increase the differential pressure between the injection well and the top of the closure, the capillary pressure of the pore space can no longer be exceeded and CO_2 becomes trapped

by capillary forces in the pore. Steeper dip (> 10° degrees) of the reservoir or additional injected CO_2 would allow for more significant updip migration.

The effect of faulting on plume distribution with time is illustrated vertically in figures 3.3.1 and 4.3.1. Faults running perpendicular to flow (strike-oriented) will create a barrier to CO_2 migration. This creates a pooling effect both horizontally and vertically along the fault (figure 3.3.3). Faults oriented parallel to flow (dip-oriented) have little effect on the plume distribution. Seal integrity of the faults is not examined in this study (see Nicholson, 2012), but from the model results, we see that further study of the fault sealing capability is necessary to better assess the capacity of the reservoir.

Vertical CO_2 distribution is ultimately controlled by buoyancy effects. Figure 3.3.3 shows that at the end of the simulation, almost all of the injected CO_2 is contained in the upper 10 feet (3 meters) of the reservoir, though the wells are perforated throughout the entire interval. CO_2 is mainly present in the lower portion of the reservoir when pooled against a fault. This is most notable in the plume associated with well 1. Figure 4.3.1 shows the early and late vertical CO_2 plume distribution in cross section for well 1. The initial high injection rate and flow velocity allows CO_2 to migrate laterally at depth to some degree though, even initially, the gravity override is apparent from the conical shape of the plume. After 100 years of injection, CO_2 has migrated vertically and has become more confined to the upper half of the reservoir. Where flow is restricted by a fault barrier, the CO_2-brine contact becomes horizontal with time due to the effects of gravity and continued updip migration of the plume.

The well injection profile for the base case (figure 3.3.4) shows that each of the 4 wells injects a unique total mass that is achieved over variable amount of time. The controlling factor on relative well performance in a given simulation is always the depth

of the reservoir at the well bottom-hole elevation. This is due to the constant pressure injection condition applied to the reservoir model. Because the pressure limit for each well is calculated based on the depth of the underlying reservoirs, the wells located above the deepest portions of the reservoir will have the highest pressure limit. Figure 2.3.6 shows the increasing divergence of fracture pressure limit gradient from the hydrostatic gradient with depth. At greater depths the difference between hydrostatic and fracture pressure, or ΔP, increases. ΔP effectively determines the performance of wells, where a large ΔP allows greater total injected mass. Because deeper wells are able to elevate pressure more significantly than shallower wells, deep wells very rapidly increase the pressure in the entire reservoir model. This increased pressure is soon "felt" by shallower wells and their injection ceases. Though the connectivity between wells is limited by fault barriers, closed boundary conditions force the rapidly increasing pressure to propagate through the few available conduits.

In addition to a larger allowable ΔP, deep wells are also able to inject CO_2 at higher density than shallow wells. The effect of high density injection is twofold. First, greater density allows for a larger mass of CO_2 to be injected in a smaller volume. Second, the smaller volumes allow for a slower pressure buildup and enhanced injection.

Cases 1 and 2 show the effect of varying φ, κ, and S_w, which proves to be qualitatively similar to the effect observed in the simple dynamic model (Fig. 4.2.1). Increasing porosity and decreasing water saturation (case 1) increases capacity, whereas decreasing porosity and increasing water saturation (case 2) decreases capacity. The final plume distributions show almost no difference among the base case, case 1, and case 2. This suggests that the fluid flow behavior is very nearly identical, only the scale is different. That is, the plume footprint is the same but the increased or decreased pore

space creates a larger or smaller volume that can be occupied by CO_2. Increasing permeability causes wells to reach their maximum injected mass more quickly, as seen by the sharply increasing well injection profiles of case 1. Decreasing permeability results in a long fill time, as seen by the steadily increasing and asymptotic injection profiles of case 2. In these samples, changing permeability controls the velocity at which pressure can propagate through the reservoir, which in turn determines how quickly the wells stop injection. When permeability is high and pressure propagation is rapid, the pressure front reaches the reservoir edge boundary early in the simulation. When the pressure front reaches this boundary it is diverted and pressure is elevated throughout the reservoir. The elevated pressure shuts off injection in shallow wells early and eventually the pressure footprint from the deepest well covers the entire reservoir, which no longer allows for pressure dissipation and injection from the deepest well ceases. When permeability is low, pressure propagation is slow and wells are able to inject longer before pressure is elevated in the reservoir.

The result from case 3 (open boundaries) shows the largest capacity of any of the cases considered, roughly 20 times larger than the base case. Open boundary conditions allow for very efficient dissipation of pressure that is reflected in the gradually increasing well injection profiles and high injected mass. Injection from wells is eventually limited by the rate at which the high pressure front can dissipate, which is very high initially but becomes less as the pressure footprint becomes larger with time. The spread between the well injection profiles in case 3 is much less than the base case. For example, the relative difference between the highest mass injector and the second highest mass injector (well 1 and 2) is much less in case 3 than in the base case. This is due to a decrease in the interference between wells in case 3. Wells can only interfere with one another if the

pressure front from one well expands enough to reach another well. In a closed boundary system, this condition is met quickly, since pressure propagation is stopped at the boundary and the pressure front is diverted to cover the entire reservoir. When pressure propagation is not stopped at the boundary, the pressure front will move more slowly, and speed will decrease with time. This allows shallow wells to inject longer before pressure increase from a deep well arrives, and as a result, the relative difference in the total injected mass between wells is reduced.

Defining faults as open has a minimal effect on the simulation results. This is mostly due to the large offset between most faults in the reservoir. Transmissibility across the fault is only possible in the simulation where offset is less than reservoir thickness and an overlap exists in the reservoir interval between the hanging wall and foot wall. That is, fluid can only be transmitted horizontally through a fault. Within the reservoir, overlaps across faults occur in very few areas. For this reason, the effect of opening fault transmissibility is minimal. The edges of faults are areas where offset decreases to zero and the fault becomes susceptible to horizontal transmissibility in the simulation. The effect on plume distribution is observable at the northern edge of the fault closest to well 1 (figure 3.3.4). The CO_2 plume shows slightly more southward extension on the downthrown (western) side of the fault than is seen in the base case. The overall effect of horizontally transmissible faults on capacity, however, is minor (~0.2 Mt).

Injection from a single well (case 5) yields a higher total injected mass than injection from 4 wells (base case). Injection from 15 wells (case 6) yields roughly the same injected mass as injection from 4 wells but less than from 1 well. Optimizing well locations for depth (case 7) also yields final injected mass results that are roughly similar to the base case. This suggests that the relative performance of a well array in the

simulation cannot be predicted by well count, depth, or location alone. Given the strong effect of pressure on injection, considering the behavior of the pressure distribution from a given number and location of wells is necessary to understand the effect on capacity.

The method by which pressure limits are assigned for each injection well in different cases is important to remember. Injection rates in some cases are more heavily discounted than in others depending on the amount by which the shallowest point exceeds fracture pressure at the end of injection in the initial models. Recall that the structural relief being considered is ~2,000 feet (610 meters). Thus, even if certain well arrays can inject more CO_2, the overriding condition that the reservoir cannot exceed fracture pressure essentially dampens the effect of well count and placement. The reason that the single well case results in higher overall injection than the base case, case 6, and case 7 might be due to the significant pressure barrier that separates the only injection well from the shallowest point in the reservoir. Thus, the injection well in case 5 cannot easily elevate the pressure of the reservoir beyond fracture pressure and, as a result, the injection pressure limit in the initial model requires a smaller reduction than in other well array cases. The presence of injection wells on the western side of the major fault trend in the DRMA may be a large factor in limiting injection in a homogeneous model.

The result from case 8 suggests that using a constant injection rate does not allow as much storage of CO_2 over a 100 year interval as using a constant injection pressure. The injection rates are determined by dividing the total injected mass for each well in the base case by 100 years. Thus, at the end of injection, wells in case 8 must reach the same total values as their base case counterparts unless they are shutoff early from pressure limitations. The well injection profiles for wells 1-4 in case 8 decay exponentially near the end of the simulation, indicating that pressure increase has shut off injection.

To assure that well interference is not prematurely ending injection, an additional test is performed by applying a constant injection rate to the single well case for the homogeneous scenario. The injection rate is determined by dividing the final injected mass from constant pressure injection by the duration of the simulation, and the previously determined pressure limit is left as a secondary condition. The results of this test confirm that constant pressure injection yields a greater injected mass than constant rate injection in the simulation. Figure 4.3.2 shows the constant pressure (black) and constant rate (red) results. The figure shows that a constant injection rate can be maintained for roughly 90 years (solid red line) until the pressure limit is reached. Subsequently, injection becomes pressure limited (dashed red line), and injection rate declines exponentially. The grey line shows the projection of constant rate injection if no pressure limit is enforced to illustrate that the two simulations would result in the same overall injected mass after 100 years.

The distribution of the CO_2 plume in case 8 differs considerably from the base case. The relatively slow injection in case 8 allows for significant gravity influence on the plume distribution during the entire length of injection. The results in figure 3.3.4 show that CO_2 in case 8 is present only updip of the injection wells, whereas in the base case, a portion of injected CO_2 is present downdip of the well. This illustrates the strong effect gravitational influence on plume distribution in the low velocity injection of case 8.

The effect of introducing heterogeneity to the 3D flow model is to reduce overall capacity in almost every case. There is a small reduction of injected mass with increased heterogeneity that can be observed in the model results (table 3.3.1). This suggests that even with the same average porosity and permeability as a homogeneous system, a heterogeneous system will perform less favorably. The difference is small in this case,

but the introduced heterogeneity is also relatively small. The random population of values in the statistically heterogeneous case does not allow for the well-connected baffles that may be present in a natural system and that would likely have a greater effect on storage capacity. Seismic-based heterogeneous model results show a decrease in injected mass from the statistically heterogeneous model. This is due to the presence of minor impermeable baffles which hinder fluid flow and detract from the available space for CO_2 occupation. Presence of baffles will not only create sharper pressure increases locally, but will also effectively shrink the size of the reservoir and cause pressure to rise more quickly in closed boundary cases.

One large discrepancy between the homogeneous and the seismic-based heterogeneous model results is the open boundary case. The roughly 45% decrease from the homogeneous to seismic-based model highlights the influence these impermeable baffles present in natural systems. The presence of impermeable zones compartmentalizes the reservoir and hinders pressure dissipation, causing capacity of the reservoir to decrease.

With increasing model heterogeneity, the injected mass of CO_2 for case 8 (constant injection rate) approaches the values of injected mass for the base case. The difference in injected mass between the base case and case 8 for the homogeneous, statistical heterogeneous and seismic-based heterogeneous model scenarios is 0.6, 0.2, and 0 Mt, respectively. Thus, the discrepancy between constant rate injection and constant pressure injection decreases with heterogeneity. This effect is partially due to decreasing constant injection rates with increasing heterogeneity. That is, with increased heterogeneity, the base case injected mass values used to calculate the injection rates for case 8 decrease. With lower constant injection rates, it becomes easier for wells to inject

without reaching the pressure limit. The enhanced performance of case 8 with increasing heterogeneity is also due to differences in pressure dissipation in homogeneous and heterogeneous systems. Homogeneous systems are able to rapidly dissipate pressure which enables high initial pressure rates and overall increased capacity. With the slow pressure buildup of the constant injection rate case, the velocity of the pressure front is not maximized in the initial years of injection and near the end of injection, the large size of the pressure front hinders any additional dissipation. Heterogeneous scenarios, however, are not able to maximize initial injection rates to the same degree as in the homogeneous scenario, because low permeability zones hinder rapid pressure dissipation. The slow pressure build up associated with constant rate injection allows additional time in which pressure can propagate through low permeability cells and avoid the impermeable zones present in heterogeneous models.

The similarity in plume distribution between homogeneous and heterogeneous models suggests that random heterogeneity does not significantly divert fluid flow. That is, no obvious preferential permeability pathway is taken by the CO_2; they do not occur in the model as a result of random assignment. This results in a lack of connectivity between high permeability cells, which may be overcome with assignment of correlation lengths. However, for this site, data do not allow any correlation length assignment to be made. The random population of permeability used in the statistical heterogeneous model and in the sand facies of the seismic-based heterogeneous model does not allow for existing well-connected high permeability conduits that may serve as significant preferential pathways. The presence of impermeable zones in the seismic-based heterogeneous model does not cause significant diversion of CO_2 flow. That is, the final plume geometry is nearly identical to the base case, only CO_2 is forced into the underlying layer where an

impermeable zone is present at the top of the reservoir. CO_2 does not flow around baffles in the simulation; rather it flows above or below them. Any effect on CO_2 flow path by random heterogeneity is not significant enough to overcome the effects of high flow velocity from large injection rate or gravitational buoyancy effects.

Fill time variations in the base cases for the homogeneous and heterogeneous models (figure 3.3.8) appear to be affected primarily by presence of heterogeneity and secondarily by pore volume. The slowest filling reservoir of the three is the statistical heterogeneous model. Low permeability cells in the statistical heterogeneous model may serve as bottlenecks to pressure dissipation and slow down the propagation of the pressure front. This allows injection to continue longer, but at a slightly lower rate than the homogeneous model. Though more varied in the permeability field, the seismic-based heterogeneous model is able to be filled faster than the statistical heterogeneous model. This is likely due to the slight decrease in reservoir pore volume from the presence of zero-porosity zones. Including these zones creates a smaller reservoir that can be filled faster.

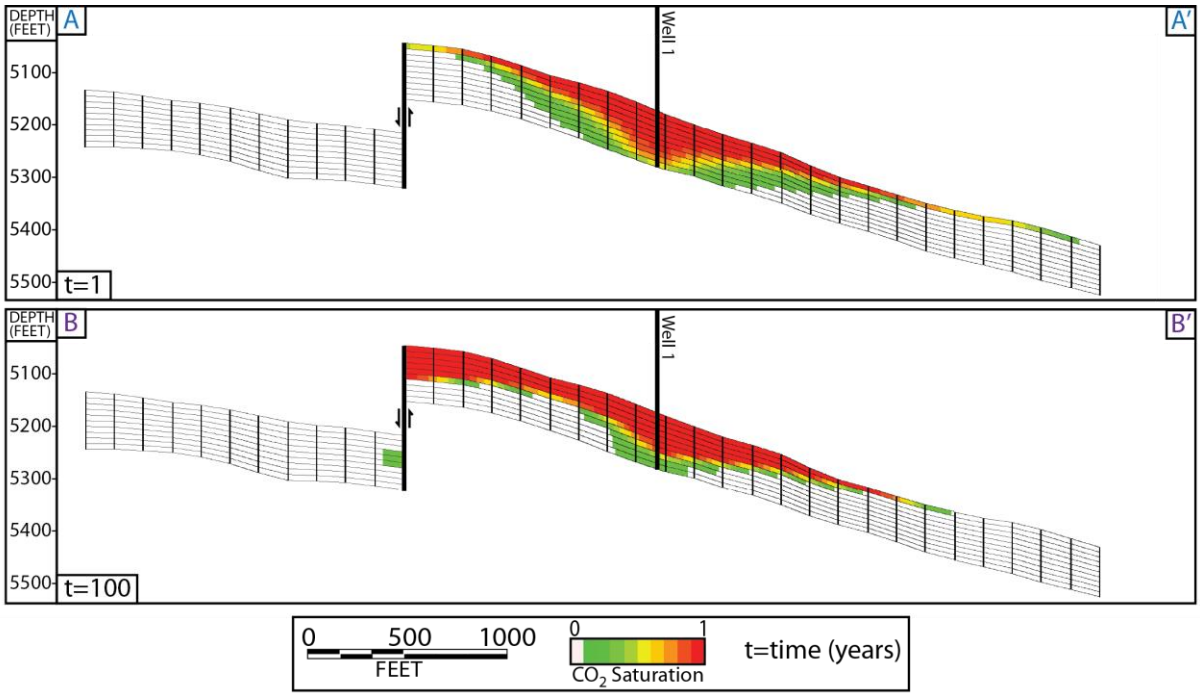

Figure 4.3.1: Cross section of CO_2 plume at t=1 (A-A') and t=100 (B-B') for injection well 1. The locations of cross section lines are shown in figure 3.3.1.

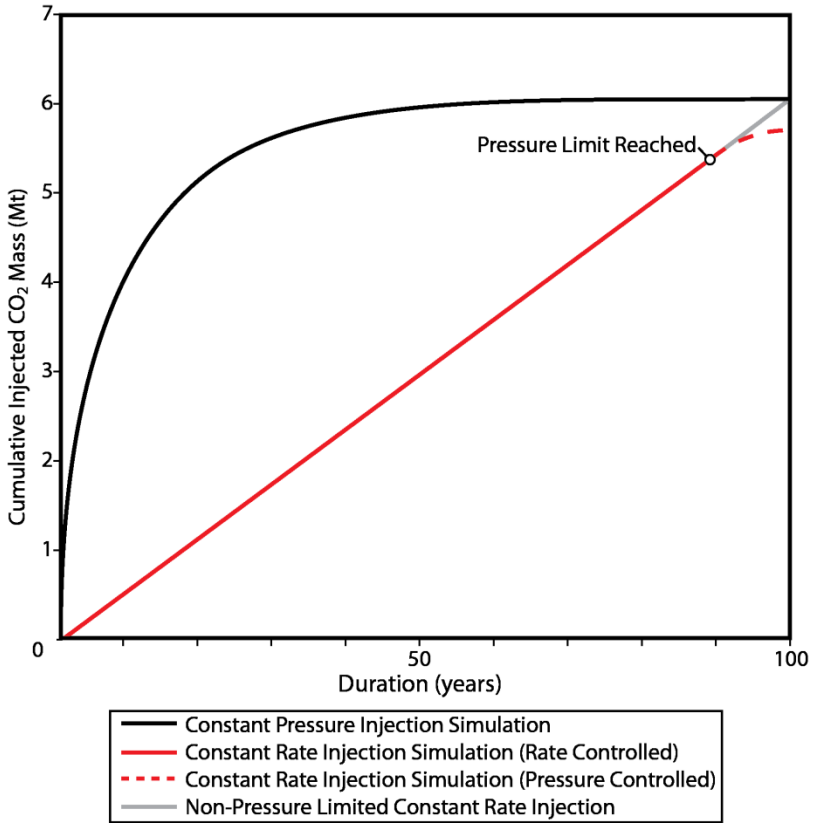

Figure 4.3.2: Cumulative CO_2 injection vs. duration for homogeneous single well injection with constant rate (red) and constant pressure (black) injection. The dashed red line represents constant pressure injection after the pressure limit is reached. The grey line shows the cumulative injection if no pressure limit is established.

Chapter 5: Discussion

CHAPTER 5.1 DISCUSSION OF REGIONAL STATIC MODEL

The primary use of the regional capacity maps (figures 2.2.9 and 2.2.12) should be to estimate capacity for selected areas of interest. Understanding that the resulting capacity values are tied to assumptions that can significantly impact actual capacity is important. For example, if the static volumetric capacity estimate is correct, for this capacity to be realized, every sand interval in the capacity interval must be perforated and injected to the maximum. For most of the study area, this is not feasible due to the large number of individual sand beds.

This estimate does not accurately consider geologic structure over small areas. That is, when summing values over large areas, the considerations of net-to-total area in the efficiency factor discount open structures that can contain less CO_2 (low bulk saturations) than structural closures (high bulk saturations). Because the regional study area encompasses many closures and many open structures, an average discount may be a valid assumption. However, when investigating a small area or a discrete point for CO_2 storage capacity, assuming an average areal discount is not valid. Because the actual structure and location of closures are not known prior to obtaining more detailed seismic data, capacity may be much higher or lower than the regional average potential at a specific location. If, for example, the point of investigation is in a structural closure, the capacity may be significantly higher than regionally predicted. If the point is over an open syncline or homocline, on the other hand, the storage potential may be significantly less than the regional average. For this reason, the regional capacity map should not be integrated over areas less than roughly twice the size of an average closure, which is approximately on the order of hundreds to thousands of acres (tens of square kilometers).

This rough integration limit is chosen because it will likely encompass an area large enough to contain both an open structure and a closure.

The most significant ways in which regional capacity estimates can be manipulated is through the definition of stratigraphic and reservoir thickness and the selection of an efficiency factor. The trends of the capacity maps generated in this study show that thickness is a primary influence; however, thickness is also highly susceptible to change with varying definitions. Thickness directly depends on the upper and lower limits of the estimation interval, which can be arbitrarily chosen. If a net capacity approach is used, thickness will also be susceptible to the sand picking methodology. Thickness definitions should be considered carefully when trying to understand the most accurate and precise storage capacity for a region. Equally important, but less constrained, is the selection of an efficiency factor. From the gross to the net capacity refinements, the potential error of the efficiency factor becomes evident. By constraining one of the five unknown variables in the determination of E (equation 9), a 25% difference is discovered, but the possible error in the remaining 4 variables is still uncertain. The range in efficiency factors from P_{10} to P_{90} spans from 0.51 to 5.4% (NETL, 2008) which means that, without special knowledge of any efficiency factor parameters in the area of interest, the potential range of capacity for a given area cannot be constrained beyond an order of magnitude. A general knowledge of the area of interest might not be sufficient to constrain E with any success. For example, the high sand volumes and long history of oil and gas exploration and production in the offshore Texas Miocene interval would suggest that an $E_{hn/hg}$ in the upper half of the probability range might be appropriate. However, from the data-supported $E_{hn/hg}$, the offshore Miocene is observed to fall in the lower range of probability. The reason for this is likely a result of

varying definitions of net sand. Our study considers primarily permeable sand intervals with defined SP cutoffs to be net sand. If any portion of the subsurface with a sand lithology were to be considered net sand, the net-to-gross ratio would be much higher. Because tight sand reservoirs (low φ and κ) would likely make poor offshore CCS targets, due to long fill times and small storable volumes, we should consider only permeable reservoirs in capacity estimates. Given the highly uncertain nature of E and the direct impact it has on capacity estimates, one must carefully consider the credibility of any single value of estimated capacity for a given region.

The primary benefit of using regional capacity estimates is the low cost in data and interpretation time necessary to yield results. From the NETL range of efficiency factors, as well as from subsequent refinement comparisons, we observe that this approach may be sufficient if knowledge of capacity is only necessary to be constrained within an order of magnitude. The results from this method should not be used to estimate capacity with confidence beyond this range of certainty.

CHAPTER 5.2 DISCUSSION OF SIMPLE DYNAMIC ANALYTICAL MODEL

The spread in the results of the simple dynamic analytical model is slightly less than that of the regional assessment. The variability in the dynamic model, however, is solely due to the changes in φ, κ, and S_w, whereas the variability in the regional assessment is primarily due to uncertainty of the efficiency factor. Error or probability of simple dynamic capacity is not easily quantified for a single simulation run. By comparing multiple results with variations of uncertain parameters, the error related to the input variables is tested to some degree, but the potential error from the inherent assumptions of the calculation is not quantified. We assume that the resulting values

represent the high end of capacity for each run, since Jain and Bryant (2011) suggest that the calculation is overly optimistic due to the over-simplification of flow behavior.

The simple dynamic analytical tool requires a significantly larger amount of data and interpretation time than the regional assessment. The addition of 3D seismic data, depth conversion, horizon interpretation, and closure analysis to the capacity assessment is costly and time consuming. The over-simplification of flow behavior and open boundary conditions, however, results in overly-optimistic capacity values. The additional work necessary to generate a reservoir mesh and perform 3D flow simulations with more accurate physical considerations is relatively minor. Only a slight gain is made in the understanding of capacity with this simple dynamic analytical model, yet a great amount of additional effort is required.

The value of this kind of simulation is less in the refinement of storage volume, and more in the addition of fill time to the capacity estimate. This dynamic aspect of the calculation is an important factor that is not considered in the regional assessment. The main benefit of dynamic analytical analyses appears to be an aggregate understanding of the geologic influences on fill times. Thus, one could decide to evaluate only the capacity that is available in a given time period (e.g. 50 years), which would result in some reduction of the dynamic analytical capacities. When considering fill time, some reservoirs may become completely unfeasible as CCS targets due to excessive injection duration necessary to reach the capacity potential. Take, for example, the model runs with high available pore space and low injected CO_2 mass (figure 4.2.2). These reservoirs are represented by the red points that are present above the linear trend. If considered in an NETL type assessment, these reservoirs may show capacity that is 2-3 times higher than could be achieved within 100 years of injection. These low permeability-high pore

volume reservoirs will not make suitable CCS targets and should ideally be dropped from consideration in regional assessments.

CHAPTER 5.3: DISCUSSION OF 3D DYNAMIC FLUID FLOW SIMULATION

The overall change in capacity created by varying the base case 3D fluid model is relatively small with the exception of boundary condition cases. This is an important result considering the goal of comparing various capacity assessments using increasingly more-refined methods. That is, while varying local geologic parameters can marginally adjust final capacities, pressure constraints are likely to be the single biggest factor influencing the actual capacity of a reservoir. Determining possible boundary conditions for a reservoir prior to well testing is difficult and is an expensive downstream part of site development. However, the 3D simulation results bound the capacity with enough precision to likely make an economic case (or not) for drilling such a test well. Even if boundaries are perfectly open, like the condition shown in case 3, any other injection activity in the interval, even at a great distance away from the model area, would be felt and reduce injection potential. The boundary conditions will most likely neither be fully open nor fully closed. Quantifying the length connectivity of the reservoir through pressure testing will be the most effective way to constrain estimates of capacity generated by 3D flow modeling. The extended length of time needed to conduct such a well test makes them expensive, and are only rarely undertaken. Well tests of the duration needed to define boundary conditions for CCS projects are much longer than those typically performed for hydrocarbon production, and thus represent an important cost consideration for proving up ultimate capacity in a region.

By considering the importance of boundary conditions, the accuracy of the model results can be inferred. Because perfectly open boundaries over large areas are unrealistic

geologically and because multiple injection sites in the reservoir interval would reduce capacity even in hypothetically open boundary cases, the results from case 3 (table 3.3.1) are likely too high. Also, the migration of CO_2 into the volumetrically expanded edge cells in case 3 indicates that CO_2 is no longer confidently contained within the DRMA and that resulting injected mass is not comparable to other cases. The closed boundary geometry used in the 3D models is certainly unrealistic; however, the relative size and connectivity length within the model boundaries may be on a scale that is close to reality. Compartments around the injection wells may be bigger or smaller than the reservoir model, which would increase or decrease capacity, respectively. The size of the compartment will be limited by heterogeneity and fault locations. Understanding of heterogeneity can be guided by a depositional and diagenetic model, but will always be difficult to quantify at a fine scale. With the use of seismic data, some heterogeneity can be observed, but the low resolution of the data within the reservoir does not typically allow for the kind of quantification necessary for a thorough understanding of the connectivity of the reservoir. The results from case 3 show that the addition of more realistic heterogeneity will reduce the effect of open boundary conditions. An ideal model would be large in area and populated with high resolution heterogeneity so that boundary conditions would need no definition and would be determined by the permeability field.

Though not assessed in this study, the sealing capacity of the faults is important to understanding the capacity of the reservoir. The effect of horizontal leakage, tested in case 4, does not accurately examine leakage, because vertical fault permeability is set to zero. The fault seal potential analysis for CO_2 storage in the offshore Texas Miocene interval (Nicholson, 2012) is useful for understanding the potential limitations of fault-trapping for CCS. The results of this study suggest that the maximum CO_2 column height

that can be sustained by a fault in this region may be significantly lower than the column height that could exist if the structure is filled to spill. This is potentially quite significant, because it suggests that pressure limitations may ultimately keep column heights in structural closure to heights that are demonstrably safe considering known methane column heights retained. However, it does suggest that the full closure height of most structures may not be available for storage in the time frames of interest economically. Though the reservoir model results show that CO_2 migrates to fault boundaries where it is eventually pooled, significant amounts of CO_2 are shown to be trapped by capillary forces downdip of the faults. With strategic well placement, a CCS project may still be feasible in a system with low fault sealing potential by maximizing capillary trapping. These model results suggest that the limitation of faults will not be their ability to retain CO_2 columns, but their ability to handle a large pressure increase without failure or reactivation. Even with strategic well placement, large pressure increases at the faults will likely be unavoidable.

Some of the 3D flow model case results are in opposition to expectations, particularly the effect of well number. Remembering that even the seismic-based heterogeneous model is grossly oversimplified is important when trying to understand these results. That is, as the model parameters become more realistic, the system may behave in a way that is closer to expectations. The perfect connectivity and closed boundaries in the homogeneous case create a system where pressure interference from additional wells is very strong, even over great distances. If the system were populated with natural scale permeability with accurate correlation lengths, the wells would not interfere as strongly. The addition of more wells in a realistic permeability setting will be much more likely to improve capacity by accessing pore space that may be unavailable to

the existing wells. The inferred consequence of this logic, however, is that the homogeneous and heterogeneous closed boundary models are likely overly optimistic. Additional heterogeneity and compartmentalization will only serve to reduce capacity, unless the compartment size is larger than the DRMA and very well connected. However, given that the DRMA is 26,496 acres (107 km^2) in size, this scenario seems unlikely.

The realistic nature of any of the individual 3D flow simulations is not the focus of this study. Rather, the purpose of 3D modeling is to begin to understand the effect on overall storage capacity when dynamic fluid flow and pressure conditions are considered. Generating multiple cases of this kind of model is done primarily to understand a potential range of capacity for the reservoir as well as to highlight the importance of the unknown parameters that would be necessary to study before an injection project could be planned.

The poor well ties to seismic data in the reservoir interval indicate the potential error in the sampling of seismic properties to the reservoir mesh. The impedance values used to populate the reservoir mesh may not be accurate indications of lithology. The most important contribution to the model from seismic population, however, is the addition of continuous baffles (considered to be qualitatively realistic geologically), seen in the form of connected impermeable shale zones. Whether or not the distribution is completely accurate for the reservoir, the mere presence of the baffles allows us to examine their effect on capacity. Again, the actual capacity of this specific reservoir is not the goal of this project; rather, our goal is to provide a more accurate estimate for any reservoir in the region when examined at a finer scale. For this reason, the log derived φ, κ, and S_w of the reservoir are not used. By leaving these inputs variable we believe that

the results become less unique to the conditions of the individual reservoir and may be more broadly applicable to the region.

CHAPTER 5.4: REFINEMENT COMPARISON

To better observe the effect of calculation refinement on estimated capacity, the results from gross and net regional assessments (appropriately normalized – see below), simple dynamic analytical modeling, and 3D dynamic flow modeling are compared in the plot in figure 5.4.1 This figure illustrates the relationship between the values of estimated capacity using a given method and the amount of effort necessary to perform each estimate refinement. The range of values produced by each calculation method, by varying input parameters, is plotted vertically by probability, where the darkest shade is the P_{50} value.

Because the regional assessments consider a much larger area and thickness than the dynamic reservoir models, they must be normalized before they can be compared directly and meaningfully to the flow simulation results. The simple dynamic analytical model is based on the same geologic inputs as the 3D flow model, so no normalization is necessary for comparison of those two estimates. Normalizing regional assessments is performed by applying the regional calculation to the reservoir inputs over the simulation domain. However, because reservoir thickness is primarily the net sand thickness, h_g, (in equation 1) cannot be specified and choosing any other thickness as a starting point would be arbitrary. Instead, the net capacity is calculated and gross capacity is inferred using the net-to-gross capacity relationship observed in chapter 3.1.

Net capacity is calculated by applying equation 11 to the dynamic reservoir inputs. A thickness value of 94.9 feet (28.9 meters) is obtained by averaging the isopach of the reservoir over the entire DRMA. Though the regional assessment uses initial

reservoir pressure to determine CO_2 density, the dynamic model results represent final pressure conditions. Thus, a CO_2 density of 0.795 g/cc is calculated at reservoir temperature and 80% of lithostatic pressure using equations 14 and 17, respectively, with an average midpoint depth over the DRMA of 5,083 feet (1,549 meters) as the depth input. An input area of 26,496 acres (107 km^2) is used for the DRMA. The calculation is performed for the 6,206 samples of porosity used in dynamic modeling. The efficiency factor used in each calculation is varied to better capture the range of possible capacity estimates. Using Goldsim software, the Monte Carlo simulation performed in the determination of E_{net} in Chapter 2.2 is repeated with 6,206 realizations. Each the resulting E_{net} realization is paired randomly with a porosity sample and net capacity is calculated. The resulting distribution of calculated CO_2 storage capacity has a P_{50} value of 30.4 Mt (figure 5.4.1).

Gross capacity for the model reservoir is determined by dividing the net capacity results by the average net to gross capacity ratio in the DRMA. A value of 0.81 is obtained by dividing the net capacity grid by the gross capacity grid and averaging the resulting grid values within the DRMA outline polygon. Each of the 6,206 realizations of net capacity is divided by this ratio to approximate gross capacity, which is found to have a P_{50} value of 37.5 Mt (figure 5.4.1). This method for determining gross static capacity in the reservoir model is selected because it most accurately reflects the gross to net overestimation observed over the DRMA in regional comparisons.

Simple dynamic analytical model results are plotted in figure 5.4.1 with a vertical bar reflecting the probability distribution of the model runs forthe 6,206 φ, κ, and S_w samples. Results from homogeneous, statistically heterogeneous, and seismic-based heterogeneous 3D flow models are plotted separately as they required varying amounts of

effort. The vertical bar plotted for each 3D flow model result represents the base case and seven cases performed for each scenario. The open boundary case is not included in the plot as the results are not comparable due to CO_2 migration out of the study area. Because the number of runs for each model type is so few, the vertical distribution shows the minimum, maximum, and mean rather than a probability distribution (figure 5.4.1).

The effort necessary to produce each refinement step can be described as a function of two parameters: time and cost. Time, in this case, describes the hours spent making log interpretations, digitizing logs, generating maps, picking sand, depth-converting seismic volumes, mapping seismic horizons, etc. Cost refers to the amount of money spent on data, salary, and overhead (building utilities, equipment, etc.). Table 5.4.1 gives an estimate of cost and time break down for each refinement step. Time is estimated for a project performed by a single person. Data costs are calculated using the unit price and quantity of data purchased for each study. Due to our agreement with SEI we are not able to reveal the actual price of the acquired seismic volume, so seismic data costs are assumed to be \$80 an acre (4,047 m^2). Due to the variability of the cost of overhead, it is not estimated in this study. Because each refinement step requires the data and interpretation time from the previous step, time and cost for each step is calculated cumulatively.

The comparison results in figure 5.4.1 show a decrease in estimated capacity with additional refinement, with the exception of the dynamic analytical model. The estimated capacity results from the net regional model are similar to the dynamic analytical model. Only the dynamic analytical model shows a much smaller probability range. The fluid flow assumptions in the dynamic analytical model make comparison to other capacity estimates difficult. The dynamic analytical model is known to be overly optimistic,

whereas the regional and 3D flow models attempt to more accurately model capacity. The results of the dynamic analytical solution are likely highly site specific. Estimated capacity is directly related to the input area in the dynamic analytical solution. Because the fluid flow assumptions are so optimistic, the calculation can only be applied to the closure areas. In the regional and 3D flow estimates, the entire DRMA is considered either for pressure buildup or volumetric calculations. Thus, for an area where the closures were smaller relative to the study area, the dynamic analytical solution results would have a significantly different relationship to the results from regional and 3D flow models, whereas the relationship between regional and 3D models would likely be much less affected. Thus, we suggest that the dynamic analytical solution is not ideal for capacity estimation. The added understanding by using 3D flow models is significant and the additional time and cost is relatively minor. The primary benefit of the simple dynamic model is a basic understanding of fill time.

An approximately 88% decrease in capacity is observed from the gross regional estimate to the seismic based heterogeneous models. The expected range of capacity also becomes much smaller with additional refinement, though in 3D models this is shown to be highly contingent on boundary assumptions. The reason for the large discrepancy between the gross regional model and the 3D flow models is the consideration of pressure. Pressure constraints and reservoir fracturing are not considered in the regional model, but are extremely limiting in 3D flow model simulations. The end result from the 3D modeling may not be indicative of the actual capacity of this site, however, without a better understanding of reservoir connectivity and boundary conditions, it is a reasonable estimate. Note that the maximum capacity values from 3D modeling are lower than the P10 values from the regional models. Given that the 3D models represent a possible

scenario, the range in efficiency factors used in regional modeling should yield results that encompass the capacity range from 3D modeling.

Table 5.4.1: Time and cost break down for each refinement step. Time is estimated for a single person and totals are summed cumulatively.

Gross Regional Static Model

	Cost				Time	
	Item	Unit Cost	Quantity	Total	Task	Time
Data	Raster logs	$9-13	3,300	$36,300	Database building	.5 years
Data	Digital Logs (LAS)	$250-280	50	$13,250	Log interpretation/ tops picking	.5 years
Data	Paleontological tops data	$11-22	448	$7,500	Log digitizing	.2 years
Data	Salary	$40,000/ year	1.4 years	$56,000	Map generation and calculation	.2 years
			total	**$113,050**	**total**	**1.4 years**

Net Regional Static Model

Cost				Time	
Item	Unit Cost	Quantity	Total	Task	Time
Salary	$40,000/ year	.35 years	$14,000	Sand picking	.25 years
				Map generation and calculation	.1 years
	+ Gross Regional		$113,050	+ Gross Regional	1.4 years
	total		**$127,050**	**total**	**1.75 years**

Simple Dynamic Analytical Model

	Cost				Time	
	Item	Unit Cost	Quantity	Total	Task	Time
Data	3D Seismic Data	$80/ acres	26,496 acres	$2,119,680	Database management	.2 years
Data	Digital Logs (LAS)	$250-280	14	$3,710	Seismic interp./ Horizon picking	.5 years
Data	Checkshots	$100	14	$14,000	Depth conversion	.25 years
Data	Salary	$40,000/ year	1.1 years	$44,000	Closure analysis	.05 years
					Model set up and calculation	.1 years
			+Net Regional	$127,050	+ Net Regional	1.75 years
			total	**$2,308,440**	**total**	**2.85 years**

Table 5.4.1 continued.

Homogeneous 3D Dynamic Model					
Cost				Time	
Item	Unit Cost	Quantity	Total	Task	Time
Salary	$40,000/ year	.35 years	$14,000	Model Generation	.25 years
				Simulation time	.05 years
+ Simple Dynamic Analytical			$2,308,440	+ Simple Dynamic Analytical	2.85 years
total			**$2,322,440**	**total**	**3.2 years**

Statistical Heterogeneous 3D Dynamic Model					
Cost				Time	
Item	Unit Cost	Quantity	Total	Task	Time
Salary	$40,000/ year	.1 years	$4,000	Model Generation	.05 years
				Simulation time	.05 years
+ Homogeneous 3D Dynamic			$2,322,440	+ Homogeneous 3D Dynamic	3.2 years
total			**$2,326,440**	**total**	**3.3 years**

Seismic Based Heterogeneous 3D Dynamic Model					
Cost				Time	
Item	Unit Cost	Quantity	Total	Task	Time
Salary	$40,000/ year	.15 years	$6,000	Model Generation	.1 years
				Simulation time	.05 years
+ Statistical Heterogeneous 3D			$2,326,440	+ Statistical Heterogeneous 3D	3.3 years
total			**$2,332,440**	**total**	**3.45 years**

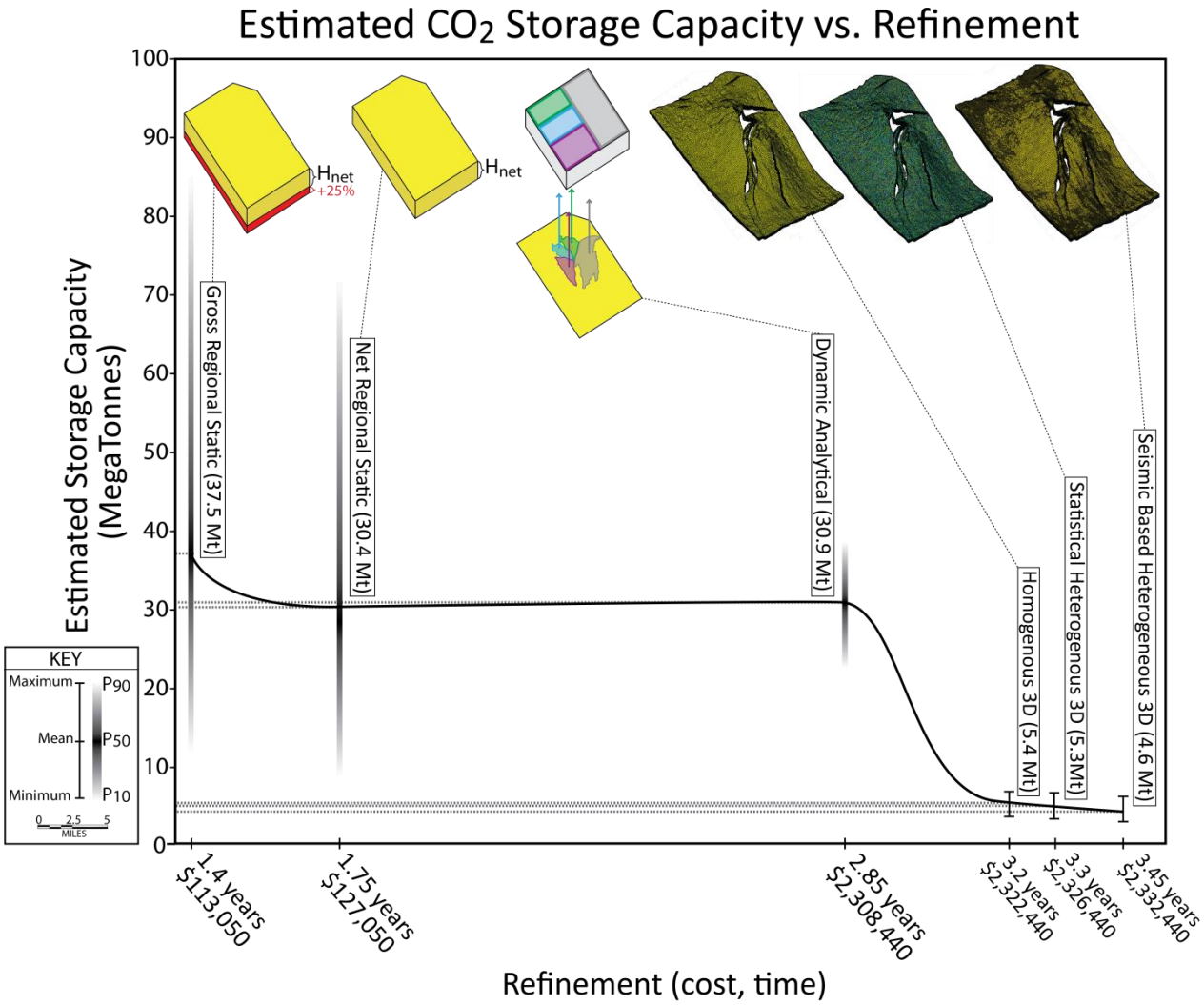

Figure 5.4.1: Estimated CO_2 storage vs. refinement. Time and cost for each step is given on the x-axis. Vertical shading represents probability distribution and vertical bars represent the range of results. Note that the horizontal scale in the key applies to all diagrams in the upper portion of the chart.

Chapter 6: Conclusion

The use of regional assessments to determine feasibility for long term CCS planning, domestically and worldwide, may lead to a extremely optimistic understanding of actual storage potential. Regional assessments should be reported within a large range, spanning at least an order of magnitude unless additional data to the inputs in equation 1 are available. The range of efficiency factors presented by NETL likely does not fully encompass the realistic range for an injection scenario where pressure limits must be considered. Though the results from this study are not broad enough to suggest an improved efficiency factor, for the single scenario considered in this work, the efficiency factor appears to be inadequate to accurately discount the available storage capacity. For the model area investigated in this study, the only way to estimate capacity accurately is to develop a sophisticated 3D model with reservoir specific pressure connectivity data. Without this, capacity is very difficult to estimate with a narrow uncertainty range.

CONTRIBUTIONS OF THIS STUDY

The contributions of this study are:

- An NETL based regional capacity assessment methodology for the Miocene stratigraphy of the Texas State waters with the use of gridded inputs as equation variables
- A gross and net regional static capacity assessment from 3,300 well logs and paleontological data of the offshore Texas Miocene interval
- Application of the simple dynamic algorithm proposed by Jain and Bryant (2011) to an offshore Texas Miocene interval reservoir
- Development of a 3D dynamic flow model for a reservoir site in the offshore Texas Miocene interval

- An understanding of estimated fill times for a potential offshore Texas Miocene interval reservoir and an appreciation for the geologic characteristics that influence fill times.
- A comparison of capacity estimates from multiple increasing levels of refinement in the calculation methods and data inputs.

REFERENCES

Allen, D. E., B. R. Strazisar, Y. Soong, and S. W. Hedges, 2005, Modelling carbon dioxide sequestration in saline aquifers: Significance of elevated pressures and salinities: Fuel Processing Technology, v. 86, p. 1569-1580.

Archie, G. E., 1942, The electrical resistivity log as an aid in determining some reservoir characteristics: Petroleum Transactions of AIME, v. 146, p. 54–62.

Audigane, P., I. Gaus, I. Czernichowski-Lauriol, K. Pruess, and T. Xu, 2010, Two-dimensional reactive transport modeling of CO_2 injection in a saline aquifer at the Sleipner site, North Sea: American Journal of Science, v. 310, p. 282-324.

Bachu, S., 2000, Sequestration of CO_2 in geologic media: criteria and approach for site selection in response to climate change: Energy Conversion and Management, v. 41, p. 953-970.

Bachu, S., 2003, Screening and ranking of sedimentary basins for sequestration of CO_2 in geologic media in response to climate change: Environmental Geology, v. 44, p. 277-289.

Bachu, S. and W. D. Gunter, 2003, Acid gas injection in the Alberta basin, Canada: a CO_2 storage experience: Geological Society, London, Special Publications, v. 233, p. 225-234.

Batzle, M., and Z. Wang, 1992, Seismic properties of pore fluids: Geophysics, v. 57, p. 1396-1408.

Benson, S. M., and D. R. Cole, 2008, CO_2 sequstration in deep sedimentary formations: Elements, v. 4, p. 325-331.

Bradshaw, B. E., and J. S. Watkins, 1994, Growth-fault evolution in offshore Texas: Gulf

Coast Association of Geological Societies Transactions, v. 44, p. 103-110.

Buckley, S. E., and M. Leverett, 1942 Mechanism of fluid displacement in sands: Transactions of AIME, v. 146, p. 1-7.

Burton, M., N. Kumar, and S. L. Bryant, 2008, Time-dependent injectivity during CO_2 storage in aquifers: SPE/DOE Symposium on Improved Oil Recovery, 20-23 April 2008, Tulsa, Oklahoma, USA.

Carr, D. L., 2010, Unpublished data, Bureau of Economic Geology, Austin TX.

Corey, A. T., 1954, The interrelation between gas and oil relative permeabilities: Production Monthly, v. 19, p. 38–41.

DOE (Department of Energy), 2010, Carbon sequestration atlas of the United States and Canada online: National Energy Technology Laboratory, Morgantown, WV, http://www.netl.doe.gov/technologies/carbon_seq/refshelf/atlas/index.html

Doughty, C., B. M. Freifeld, and R. C. Trautz, 2008, Site characterization for CO_2 geologic storage and vice versa: The Frio brine pilot, Txas, USA as a case study: Environmental Geology, v. 54, p. 1635-1656.

Duan, Z., R. Sun, C. Zhu, and I. Chou, 2006, An improved model for the calculation of CO_2 solubility in aqueous solutions containing Na^+, K^+, Ca^{2+}, Mg^{2+}, Cl^-, and SO_4^{2-} : Marine Chemistry, v. 98, p. 131-139.

Du Rouchet, J., 1981, Stress fields, a key to oil migration The American Association of Petroleum Geologists Bulletin, v. 65, p. 74-85.

Eiken, O., P. Ringrose, C. Hermanrud, B. Nazarian, T. A. Torp, and L. Høier, 2011, Lessons learned from 14 years of CCS operations: Sleipner, In Salah, and Snøhvit: Energy Procedia, v. 4, p. 5541-5548.

Fenghour, A., W. A. Wakeham, and V. Vesovic, 1998, The viscosity of carbon dioxide:

Journal of Physical Chemistry Reference Data, v. 27, p. 31-44.

Flett, M., R. Gurton, and I. Taggart, 2004, The function of gas-water relative permeability hysteresis in the sequestration of carbon dioxide in saline formations: Society of Petroleum Engineers Conference Paper, SPE Asia Pacific Oil and Gas Conference and Exhibition, 18-20 October 2004, Perth Australia.

Frailey, S. M., and R. J. Finley, 2008, Overview of the Illinois Basin's sequestration pilots, Society of Petroleum Engineers Conference Paper, SPE/DOE Symposium on Improved Oil Recovery, 20-23 April, Tulsa, Oklahoma, USA.

Friedman, S. J., 2007, Geological Carbon Dioxide Sequestration: Elements, v. 3, p. 179-184.

Gale, J., N. P. Christensen, A. Cutler, T. A. Torp, 2001, Demonstrating the potential for geologic storage of CO_2: the Sleipner and GESTCO projects: Environmental Geoscience, v. 8, p. 160-165.

Galloway, W. E., P. E. Ganey-Curry, X. Li, and R. T. Buffler, 2000, Cenozoic depositional history of the Gulf of Mexico basin: The American Association of Petroleum Geologists Bulletin, v. 84, p. 1743-1744.

Galloway, W. E., T. L. Whiteaker, and P. Ganey-Curry, 2011, History of Cenozoic North American drainage basin evolution, sediment yield, and accumulation in the Gulf of Mexico basin: Geosphere, v. 7, p. 938-973.

Gardner, G. H. F., L. W. Gardner, and A. R. Gregory A.R., 1974, Formation velocity and density -- the diagnostic basics for stratigraphic traps: Geophysics, v. 39, p. 770–780.

Giammar, D. E., R. G. Braunt Jr., and C. A. Peters, 2005, Forsterite dissolution and

magnesite precipitation at conditions relevant for deep saline aquifer storage and sequestration of carbon dioxide: Chemical Geology, v. 217, p. 257-276.

Holloway, S., 2001, Storage of fossil fuel derived carbon dioxide beneath the surface of the earth: Annual Review of Energy and the Environment, v. 26, p. 145-166.

Hovorka, S. D., S. M. Benson, C. Doughty, B. M. Freifeld, S. Sakurai, T. M. Daley, Y. K. Kharaka, M. H. Holtz, R. C. Trautz, H. S. Nance, L. R. Myer, and K. G. Knauss, 2006, Measuring performance of CO_2 storage in saline formations: the Frio experiment: Environmental Geosciences, v. 13, p. 105-121.

Jain, L., and S. L. Bryant, 2011, Time weighted storage capacity for geological sequestration: Energy Procedia, v. 4, p. 4873-4880.

Johnson, J. W., J. J. Nitao, and K. G. Knauss, 2004, Reactive transport modeling of CO_2 storage in saline aquifers to elucidate fundamental processes, trapping mechanisms, and sequestration partitioning: Geological Society of London Special Publication on Carbon Sequestration Technologies.

Juanes R., C. W. MacMinn, and M. L. Szulczewski, 2010, The footprint of the CO_2 plume during carbon dioxide storage in saline aquifers: Storage efficiency for capillary trapping at the basin scale: Transport in Porous Media, v. 82, p. 19-30.

Kaszuba, J. P., D. R. Janecky, and M. G. Snow, 2003, Carbon dioxide reaction processes in a model brine aquifer at 200^{o}C and 200 bars: Implications for geologic sequestration of carbon; Applied geochemistry, v. 18, p. 1065-1080

Keating, E. H., J. Fessenden, N. Kanjorski, D. J. Koning, and R. Pawar, 2010, The impact of CO_2 on shallow groundwater chemistry: observations at a natural analog site and implications for carbon sequestration: Environmental Earth Science, v. 60, p. 521-536.

Kumar, A., M. Noh, G. A. Pope, K. Sepehrnoori, S. Bryant, and L. W. Lake, 2004, Reservoir simulation of CO_2 storage in deep saline aquifers: Society of Petroleum Engineers Conference Paper, SPE/DOE Symposium on Improved Oil Recovery, 17-21 April 2004, Tulsa, Oklahoma.

Lackner, K. S., 2003, A guide to CO_2 sequestration: Science, v. 300, p. 1677-1678.

Lagneau, V., A. Pipart, and H. Catalette, 2005, Reactive transport modeling of CO_2 sequestration in deep saline aquifers: v. 60, p. 231-247.

Larionov, V.V., 1969, Bore hole radiometry: Nedra.

Lewicki, J. L., J. Birkholzer, and C. F. Tsang, 2007, Natural and industrial analogues for leakage of CO2 from storage reservoirs: identification of features, events, and processes and lessons learned: Environmental Geology, v. 52, p. 457-467.

Litynski, J. T., S. Plasynski, H. G. McIlvried, C. Mahoney, and R. R. Srivastava, 2008, The United States Department of Energy's regional carbon sequestration partnerships program validation phase: Environment International, v. 34, p. 127-138.

McDonnell, A., M. R. Hudec, and M. P. A. Jackson, 2009, Distinguishing salt welds from shale detachments on the inner Texas shelf, western Gulf of Mexico: Basin Research, v. 21, p. 47-59.

Morton, R. A., L. A., Jirik, and R. Q. Foote, 1985, Depositional history, facies analysis and production characteristics of hydrocarbon-bearing sediments, offshore Texas: The University of Texas at Austin, Bureau of Economic Geology Geological Circular, v. 85, p. 1-31.

Mualem, Y., 1976, A new model for predicting the hydraulic conductivity of unsaturated porous media: Water Resources Research, v. 12, p. 513-522.

NETL (National Energy Technology Laboratory), 2008, Methodology for development of geologic storage estimates for carbon dioxide online: National Energy Technology Laboratory, Morgantown, WV, http://www.netl.doe.gov/technologies/carbon_seq/refshelf/methodology2008.pdf

NIST (National Institute of Standards and Technology), 2011, Chemistry webbook thermophysical properties of fluid systems tool, http://webbook.nist.gov/chemistry/fluid/

Nicholson, A. J., 2012, Empirical analysis of fault seal capacity for CO_2 sequestration, Lower Miocene, Texas gulf coast, Master's Thesis, University of Texas at Austin, http://repositories.lib.utexas.edu/handle/2152/ETD-UT-2012-05-5606

Olabisi, A., 2011, Structural framework of the Clemente-Tomas and Corsair growth fault systems in the Texas continental shelf margin of the Gulf of Mexico: Master's Thesis, Texas Tech University, http://repositories.tdl.org/ttu-ir/handle/2346/ETD-TTU-2011-08-1792

Pawar, R. J., N. R. Warpinski, J. C. Lorenz, R. D. Benson, R. B. Grigg, B. A. Stubbs, P. H. Stauffer, J. L. Krumhansl, S. P. Cooper, and R. K. Svec, 2006, Environmental Geosciences, v. 13, p, 163-180.

Pennline, H. W., D. R. Luebke, K. L. Jones, C. R. Myers, B. I. Morsi, Y. J. Heintz, and J. B. Ilconich, 2008, Progress in carbon dioxide capture and separation research for gasification-based power generation point sources: Fuel Processing Technology, v. 89, p. 897-907

Pruess, K., J. Garcı´a, T. Kovscek, C. Oldenburg, J. Rutqvist, C. Steefel, T. Xu, 2002, Intercomparison of numerical simulation codes for geologic disposal of CO_2: Lawrence Berkeley National Laboratory Report LBNL-51813, Berkeley, CA.

Raymer, L. L., E. R. Hunt, and J. S. Gardner, 1980, An improved sonic transit time-to-porosity transform: SPWLA 21 Ann. Logging Symp., July 8-11, 1980, p. 1-12.

Ringrose, P., M. Atbi, D. Mason, M. Espinassous, o. Myhrer, M. Iding, A. Matheison, and I. Wright, 2009, Plume development around well KB-502 at the In Salah CO_2 storage site: First Break, v. 27, p. 85-89.

Salvador, A., 1987, Late Triassic-Jurassic paleogeography and origin of Gulf of Mexico basin: The American Association of Petroleum Geologists Bulletin, v. 71, p. 419-451.

Schlumberger, 1989, Chapter 1, in: Log Interpretation Principles/Applications, Schlumberger Wireline & Testing, Sugar Land, Texas, p. 5-8.

Schlumberger, 1998b, Chapter 5, Porosity Logs, in: Log Interpretation Principles/Applications, Schlumberger Wireline & Testing, Sugar Land, Texas, p.24

Schlumberger, 2000, Log interpretation charts: Schlumberger.

Seni, S.J. & The University of Texas at Austin (2006). Atlas of northern Gulf of Mexico gas and oil reservoirs. Bureau of Economic Geology.

Span, R., and W. Wagner, 1996, A new equation of state for carbon dioxide covering the fluid region from the triple-point temperature to 1100 K at pressures up to 800 MPa: Journal of Physical Chemistry Reference Data, v. 25, p. 1509-1596.

Spiteri, E. J., R. Juanes, M. J. Blunt, and F. M. Orr Jr., 2005, Relative permeability hysteresis: Trapping models and application to Geological CO_2 sequestration: Society of Petroleum Engineers Conference Paper, SPE Annual Technical Conference and Exhibition, 9-12 October 2005, Dallas, Texas.

Stuart, C. A., 1960, Geopressures, Shell Oil Company Production Department, New

Orleans.

Torp, T. A., and J. Gale, 2003, Demonstrating storage of CO_2 in geological reservoirs: The Sleipner and SACS projects: Proceedings of the 6th International Conference on Greenhouse Gas Control Technologies, p. 311-316

Tsang, C. F., S. M. Benson, B. Kobelski, and R. E. Smith, 2002, Scientific considerations related to regulation development for CO_2 sequestration in brine formations: Environmental Geology, v. 42, p. 275-281.

Ursenbach, C. P., 2007, CREWES Fluid Property Calculator, http://www.crewes.org/ResearchLinks/ExplorerPrograms/FlProp/FluidProp.htm (accessed February 3, 2013).

Vangkilde-Pedersen, T., K. L. Anthonsen, N. Smith, K. Kirk, F. Neele, B. van der Meer, Y. L. Gallo, D. Bossie-Codreanu, A. Wojcicki, Y. Le Nidre, C. Hendricks, F. Dalhoff, and N. P. Christensen, 2009, Assessing European capacity for geological storage of carbon dioxide- the EU GeoCapacity project: Energy Procedia, v. 1, p. 2663-2670.

Vogler, H. A., and B. A. Robinson, 1987, Exploration for deep geopressured gas-Corsair trend, offshore texas: American Association of Petroleum Geologists Bulletin, v. 71, p. 777-787.

Wellman, T. P., R. B. Grigg, R. K. Svec, and P. C. Lichtner, 2003, Evaluation of CO_2-brine-reservoir rock interaction with laboratory flow tests and reactive transport modeling: Society of Petroleum Engineers Conference Paper, International Symposium on Oilfield Chemistry, 5-7 February 2003, Houston, Texas.

White, C. M., B. R. Strazisar, E. J. Granite, J. S. Hoffman, and H. W. Pennline, 2003,

Separation and capture of CO_2 from large stationary sources and sequestration in geological formations-coalbeds and deep saline aquifers: Journal of the Air and Waste Management Association. V. 53, p. 645-715.

Wilson, E. J., T. L. Johnson, and D. W. Keith, 2003, Regulating the ultimate sink: Managing the risks of Geologic CO_2 storage: Environmental Science Technology, v. 37, p. 3476-3483.

Winker, C. D., and M. B. Edwards, 1983, Unstable progradational clastic shelf margins: SEPM Special Publication 33, p. 139-157.

Winker, C. D., and R. T. Buffler, 1988, Paleogeographic evolution of early deep-water Gulf of Mexico and margins, Jurassic to Middle Cretaceous (Comanchean): The American Association of Petroleum Geologists Bulletin, v. 72, p. 318-346.

Witrock, R. B., L. D. Nixon, P. J. Post, and K. M. Ross, 2003, Biostratigraphic chart of the Gulf of Mexico Offshore Region, Jurassic to Quaternary, U. S. Department of the Interior, Bureau of ocean Energy Management, New Orleans, Louisiana.

Wolf, G. H., A. V. G. Chizmeshya, J. Diefenbacher, and M. J. McKelvry, 2004, In situ observation of CO_2 sequestration reactions using a novel microreaction system: Environmental Science and Technology, v. 38, p. 932-936.

Yang, Q., 2008, Dynamic modeling of CO_2 injection in a closed saline aquifer in the Browse Basin, western Australia: Society of Petroleum Engineers Conference Paper, SPE Asia Pacific Oil and Gas Conference and Exhibition, 20-22 October 2008, Perth, Australia.

Zeidouni M., M. Pooladi-Darvish, and D. Keith, 2009, Sensitivity analysis of salt

precipitation and CO_2 brine displacement in saline aquifers: SPE International Conference on CO_2 Capture, Storage, and Utilization, 2-4 November 2009, San Diego, California, USA.

Zeng, H., 2012, Unpublished data, Bureau of Economic Geology, Austin, TX.